

Casing expansion in mono-diameter wells

a thermal analysis

Sander van Gemert



Casing expansion in mono-diameter wells

a thermal analysis

by

Sander van Gemert

to obtain the degree of Master of Science
at the Delft University of Technology,
to be defended publicly on Thursday October 12, 2017 at 10:00 AM.

Student number: 4095758
Project duration: March 6, 2017 – October 12, 2017
Thesis committee: dr. ir. M.J.B.M. Pourquie, TUDelft, ME, supervisor
prof. dr. ir. E.A. van Keulen, TUDelft, ME
prof. dr. ir. J. Westerweel, TUDelft, ME
dr. ir. A.M. Aragon, TUDelft, ME
dr. ir. P.R. Wellens, TUDelft, MT
dr. ir. W. Assaad, Shell
dr. ir. H.R. Passaribu, Shell

This thesis is confidential and cannot be made public

Abstract

When drilling for oil or gas, wells are typically constructed using a conventional or telescopic well design. After a section of the well has been drilled, a steel casing (or liner) is inserted into the hole preventing the collapse of the hole. The next well section has a smaller diameter as its casing must pass through the previously installed casing. This process leads to a stepwise reduction of the well diameter which, especially in deep or complicated wells, restricts the maximum production rate of oil and gas.

Mono-diameter technology utilizes casings which are plastically deformed after they have been placed in the well. This plastic deformation is done by pulling a conically shaped tool, known as the cone, through the newly installed casing. The plastic deformation increases the diameter of the new casing to (nearly) the same as that of the previous casing, therefore the well diameter no longer decreases with every new section.

The expansion requires a force in the order of 1000-2500[kN]. The work done by this force leads to high local heat generation due to friction and plastic deformation. This heat, poses a risk for the expansion process as the lubricant (RPSLF) decomposes above 250[°C] [10]. Decomposition of the lubricant leads to an increase of the friction, inducing more heat release and further decomposition of the lubricant. The expansion force may then exceed the pulling capacity of the drill rig or strength of the drill string, leaving the cone stuck in the well.

Previous research provides the distribution of pressure on the contact surface of the cone, the strain distribution inside the liner and the temperature dependent friction coefficient of the lubricant, by combining these the frictional heat is calculated [7, 35]. Heat generation from plastic deformation is a complex phenomenon especially at low strain (-rates). The Taylor-Quinney coefficient defines the ratio between the work done on a material and the heat generated [30]. A strain-dependent model for the Taylor-Quinney coefficient, developed by Zehnder, is used to determine the heat release from plastic deformation [38].

A numerical heat transfer model is built in Matlab, based on the finite volume method. The model uses a mesh based on skewed quadrilateral cells. Numerical stability of the model is verified for the cell size, time step and time integration method. Movement of the cone and the plastic deformation of the casing are modeled by taking a reference frame fixed relative to the motion of the cone and adding a "convective" term inside the liner. Heat transfer phenomena at all boundaries are investigated using thermal resistance models.

A series of experiments is executed to verify the numerical model. The experiments consist of full-scale expansion test using a cone equipped with 30 thermocouples placed just below the contact surface. Additionally also the temperature of the liner, expansion speed and expansion force are measured and recorded.

Comparison of the experimental and numerical results leads to the observation that the pressure profile determined in previous work is likely valid at the first onset of expansion. Over time, the forming of a lubricant film however leads to the re-distribution of roughly 20% of the force from the rear of the cone to the front. When the pressure profile is corrected for this effect; the temperatures inside the cone, temperature of the liner, expansion force and overall heat balance show a good match between the numerical and experimental results with an error of around 5%.

From the heat balance based on the experimental results, it follows that between 54% - 60% of the work done on the system is converted into heat. As all work done in the form of friction is converted into heat the remaining energy must be lost in the the work done to plastically deform the casing, this provides indirect evidence for the validity of the Zehnder model.

The validated numerical model is used to simulate a reference case field expansion, the maximum contact temperature here is 164.4[°C]. This value is well below the lubricant decomposition temperature of 250[°C], which leads to the conclusion that the process is safe and the expansion speed could even be increased from a thermal point of view.

Preface

Since march of 2017 I have been working on my Msc. thesis in close cooperation with Shell in Rijswijk. I would like to express my gratitude to Shell for entrusting me with this project and providing all the resources required for both the theoretical as experimental parts. Especially my daily supervisor, Wissam Assaad, has been of great value throughout the entire process.

Naturally I would also like to thank the TUDelft and in particular my supervisors Mathieu Pourquoiie and Fred van Keulen for all their time and advice.

Finally, I hope you enjoy reading my Msc. thesis I have certainly learned a lot and enjoyed creating it.

*Sander van Gemert
Rijswijk, September 2017*

Nomenclature

Symbol	Description	Unit
A	Area	m^2
Bi	Biot number	-
C	Numerical constants	-
C_p	Specific heat	$\frac{J}{kgK}$
Cr	Courant number	-
D_h	Hydraulic diameter	m
e	Engineering strain	-
E	Modulus of elasticity	Pa
E	East wall or surface	-
f	(Fanning) friction factor	-
F	Force	N
Fo	Fourier number	-
h	Convective heat transfer coefficient	$\frac{W}{m^2K}$
I_n	Interpolation point	-
J_n	Bessel function of the nth order	-
k	Thermal conductivity	$\frac{W}{mK}$
K	Consistency index power law fluid	Pas
K	Ratio between elastic and plastic modulus	-
L	Length scale in arbitrary direction	m
n	Swift law hardening exponent	-
n	Power law fluid exponent	-
n	Time level in numerical methods	-
N	North wall or surface	-
Nu	Nusselt number	-
P	Pressure	Pa
Pr	Prandtl number	-
q	Heat flux density	$\frac{W}{m^2}$
Q	Heat flux	W
r	Radial cylindrical coordinate	m
R	Thermal resistance	$\frac{K}{W}$
Re	Reynolds number	-
s	Engineering stress	MPa
s	Heat source	$\frac{W}{m^3}$
S	South wall or surface	-
St	Stanton number	-
t	Time	s
T	Temperature	$^{\circ}C$
U	Internal energy	J
v	Speed	$\frac{m}{s}$
V	Volume	m^3
W	(Mechanical) work	W
W	West wall or surface	-
X	Heat/ work ratio	-
z	Axial cylindrical coordinate	m

Symbol	Description	Unit
α	Thermal diffusivity	$\frac{\text{m}^2}{\text{s}}$
β	Taylor-Quinney coefficient	-
ϵ	Radiative emissivity	-
ε	Strain	-
$\dot{\varepsilon}$	Strain rate	$\frac{1}{\text{s}}$
λ_n	Bessel zero of the nth order	-
η	Apparent viscosity power law fluid	Pas
ρ	Density	$\frac{\text{kg}}{\text{m}^3}$
ρ	Expansion mode coefficient	-
σ	Stress	Pa
σ	Stefan-Boltzmann constant ($5.670367 * 10^{-8}$)	$\frac{\text{W}}{\text{m}^2\text{K}}$
θ	Circumferential cylindrical coordinate	rad
μ	Friction factor	-
μ	Viscosity	Pas
ω	Numerical parameter	-

Subscript	Description
0	Reference or ambient condition
1	Top left corner of a grid cell
2	Top right corner of a grid cell
3	Bottom right corner of a grid cell
4	Bottom left corner of a grid cell
avg	Average
c	Center of a grid cell
ce	Cement
co	Cone
cond	Conduction
conv	Convection
de	Deformation
df	Drilling fluid
do	Down hole
ds	Drillstring
e	East
ex	Expansion
fr	Friction
hy	Hydration
i	Horizontal index in the grid (West to East)
j	Vertical index in the grid (North to South)
li	Liner
lub	Lubricant
n	North
p	Plastic deformation
r	Radial direction
s	South
uts	Ultimate stress point
w	West
wa	Wall
we	Center of the east wall of a grid cell
wn	Center of the north wall of a grid cell
ws	Center of the south wall of a grid cell
ww	Center of the west wall of a grid cell
yield	Yield point
z	Axial direction
θ	Circumferential direction

Abbreviation	Description
AB-2	Second order Adams-Bashforth scheme
BC	Boundary condition
Casing	Steel tube used to secure the sides of a well
CN	Cranck-Nicolson scheme
Cone	The conical shaped tool which is used to expand the liner
Down hole	At the bottom of a well
Drill string	Steel pipe which supports the drilling and expansion tools
FD	Finite difference method
FE	Forward Euler scheme
FEM / FEA	Finite element method / Analysis
FV	Finite volume method
HTC	Heat transfer coefficient
Liner	A series of casings used to secure the sides of a well
RPSLF	Rust preventive solid lubricant F

Contents

Abstract	iii
Nomenclature	vii
1 Introduction	1
1.1 Conventional well design	1
1.2 Mono-diameter well design	1
1.3 Thermal Implications	2
1.4 Objective	3
1.5 Research approach	3
2 Scope & Literature	5
2.1 Scope	5
2.2 Scientific Literature	6
2.3 Previous work with Shell	7
3 Heat sources	9
3.1 Friction	9
3.2 Plastic deformation	12
3.3 Hydrating cement.	15
3.4 Elevated temperature	15
4 Modeling method	17
4.1 Solution Method	17
4.2 Mesh	19
4.2.1 Fitting the mesh to the geometry.	21
4.3 Time integration method	22
4.4 Numerical stability	23
4.5 Cone movement	24
4.5.1 Moving cone, absolute reference frame	24
4.5.2 Moving liner, relative reference frame	25
4.6 Thermal gradients on a non-orthogonal grid	25
4.6.1 West & East gradient	27
4.6.2 North & South gradient	28
4.6.3 Verification of thermal gradient method	30
5 Boundary Conditions	31
5.1 Contact boundary condition	32
5.1.1 Thermal resistance of the lubricant	32
5.1.2 Heat generation due to friction	32
5.2 Liner Boundary conditions	33
5.2.1 East & West	33
5.2.2 South, in front of the cone	34
5.2.3 South, to the rear of the cone.	35
5.2.4 North	35
5.3 Cone boundary conditions	36
5.3.1 South	36
5.3.2 West	39
5.3.3 East	39

6 Experiments	41
6.1 Test 1: Split cone	41
6.1.1 Goals.	41
6.1.2 Setup.	42
6.1.3 Results	42
6.1.4 Lessons learned	44
6.2 Test 2: Thermal test	45
6.2.1 Goals.	45
6.2.2 Background principle	45
6.2.3 Setup.	45
6.2.4 Results single liner	48
6.2.5 Results overlap.	49
6.2.6 Results heavy overlap	51
7 Results	53
7.1 Calibration & Validation.	53
7.1.1 Pressure profile & Cone temperatures	53
7.1.2 Plastic deformation & the Zehnder model	57
7.1.3 Heat Partitioning.	57
7.1.4 Heat balance.	58
7.1.5 Extrapolation of the results to the contact surface	58
7.2 Results for the base case	59
7.3 Sensitivity Analysis	60
8 Conclusions & Recommendations	63
8.1 Conclusions.	63
8.1.1 Heat due to friction	63
8.1.2 Heat due to plastic deformation	63
8.1.3 Validity of the heat transfer model	64
8.1.4 Peak contact temperature	64
8.2 Recommendations	65
A Components	67
A.1 Cone	67
A.1.1 Dimensions	67
A.1.2 Material	68
A.1.3 Thermal properties	68
A.2 Liner - Single	69
A.2.1 Dimensions	69
A.2.2 Material	69
A.2.3 Thermal properties	69
A.2.4 Mechanical properties	69
A.3 Liner - Overlap	70
A.3.1 Dimensions	71
A.3.2 Material	71
A.3.3 Thermal properties	71
A.3.4 Mechanical properties	71
A.4 Lubricant	72
A.4.1 Thermal properties	72
A.5 Drilling fluid	72
A.5.1 Thermal properties	73
A.6 Drill string	73
A.6.1 Thermal properties	73

B	Measurement of thermal properties	75
B.1	Liquids	75
B.1.1	Calibration.	76
B.1.2	Measuring procedure	76
B.1.3	Analysis	76
B.2	Solids	76
B.2.1	Calibration.	77
B.2.2	Measuring procedure	77
B.2.3	Analysis	77
C	Conduction of heat	79
C.1	Theoretical background.	79
C.2	Analytical approach.	79
D	Model flowchart	83
E	Thermal resistance models	85
F	Split cone design	87
G	Thermal cone design	91
H	Full results thermal cone	95
H.1	Single liner expansion.	95
H.2	Overlap expansion	98
H.3	Heavy overlap expansion	101
I	Base case	105
J	Test case	107
	Bibliography	109

Introduction

1.1. Conventional well design

When drilling for oil or gas, wells are typically constructed using a conventional, telescopic, well design. After a section of the well has been drilled, a steel casing (or liner) is lowered into the open hole preventing collapse of the hole. In most cases it is necessary to drill the well in multiple sections as the local geological formation is not strong enough to support the full length of the well. The drill bit must then pass through the top liner, and thus be of a smaller diameter than this liner. Consequently, the following liner is also of a smaller diameter and so for every section of the well the diameter of the well decreases as illustrated by Figure 1.1. Especially for very deep wells or in locations with complex geological formations this consistent reduction of the diameter may lead to a final liner which is so small that production of oil or gas is uneconomical or even impossible.

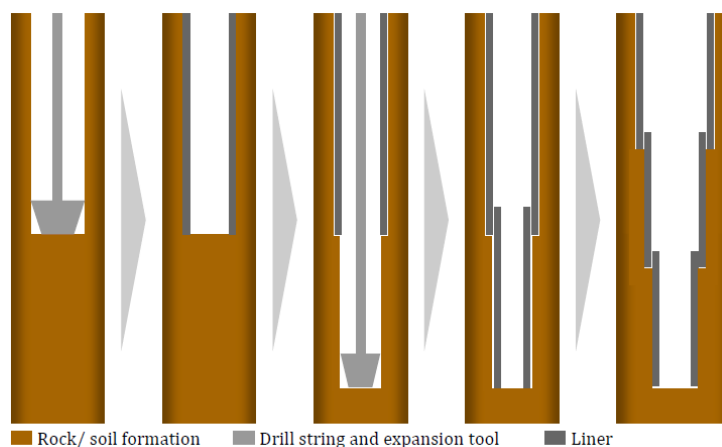


Figure 1.1: Construction of a Conventional (telescopic) well; First, a section of the well is drilled, hereafter a steel liner is inserted to prevent collapse of the well. A new section of the well can then be drilled, in which a smaller liner is inserted as it must pass through the previous liner. The final result is a well with consistent reduction of diameter.

1.2. Mono-diameter well design

The construction of a mono diameter well starts off in a very similar way to a conventional well, first a new section of the well is drilled and a (specially designed) liner is inserted with a diameter smaller than that of the liner above. The next step is to engage an anchoring system inside the previous liner known as the TAaP (Top Anchor and Pull) system. This anchor prevents movement of the liner as a conically shaped tool is pulled through. This conically shaped tool, known as the cone, has a larger maximum outer diameter than the inner diameter of the newly inserted liner. Pulling the cone through this liner plastically deforms the liner increasing its diameter in the process. The cone is designed such that the inner diameter of the expanded liner nearly perfectly matches the diameter of the previous liner, thus obtaining a mono-diameter well as

illustrated in Figure 1.2. In order to support the new section of liner there is a small section where the new and the old liner overlap each other, the new liner is hung on the old liner at this overlap section. Consequently in this section two liners must be expanded simultaneously. Due to the double wall, the expansion force required here is significantly higher and it should be analyzed separately [8, 11].

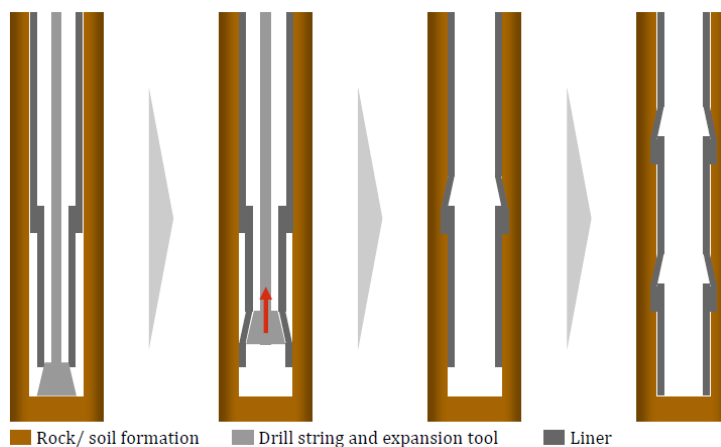


Figure 1.2: Construction of a mono-diameter (MOD) well; After the first section of the well has been constructed (identical to the conventional well design) an anchoring system is engaged in the newly inserted liner to prevent any movement. Next, a conically shaped tool is pulled upward, plastically deforming the liner in the process. This deformation process can be repeated numerous times to create a well with a constant (mono-) diameter.

Due to the minimal or no reduction in liner diameter the mono-diameter well design allows for a higher flow rate of oil and gas during production and the possibility to reach (deep) reserves unreachable with conventional technology. Mono-diameter technology has already been successfully implemented in the field several times, especially in deep-water, deep reservoir operations such as the Gulf of Mexico [23, 28].

1.3. Thermal Implications

The process of expanding the liner is prone to significant heat generation. This generated heat in combination with the already elevated temperatures down hole, pose a threat to the expansion process and in particular the lubricant. The lubricant with which the inside of the liner is coated, decomposes at temperatures above 250[°C] [7]. When the lubricant decomposes, it loses its friction reduction properties, this in turn leads to an increase of the friction force and consequently an increase of the heat generated due to friction. When the friction force increases too much it can exceed the mechanical strength of the drill string or the pulling capacity of the drill rig. This will cause the cone to get stuck with no option to continue expansion or retrieve the cone. The only option left is then to abandon the hole and bypass the failed section, an exercise which can consume a considerably amount of time. With the cost of deep-water drilling operations at around \$1 million a day this needs to be prevented at all cost.

In total four different sources contribute to the temperature increase during expansion. They are summarized below and depicted in Figure 1.3.

1. Friction between the cone and the liner

It is well known that friction between two sliding contacts produces heat. The heat originates from the local plastic deformation of the peaks of the roughness on the sliding bodies. The amount of heat released depends on the friction coefficient, the pressure and relative speed between the two bodies [3, 14].

2. Plastic deformation of the liner

When a material is deformed past the elastic limit (yield stress) the energy used to deform the material past this limit is no longer relieved elastically when the applied force is removed. Most of this energy is converted into heat. For steels typically between 80-95% of the energy used for the plastic deformation is released in the form of heat [27, 30, 38].

3. Elevated temperature at down hole conditions

Although significant local variations are possible it can generally be stated that the temperature at large depths is significantly higher than that on the surface [9]. At the locations where mono-diameter technology is considered the down hole temperature typically varies between 80[°C] and 130[°C].

4. Heat release in hydrating cement layer

In order to fix the liner to the rock formation, a layer of cement is added between the formation and the liner. During the expansion process this cement layer is still in a liquid state but the hydration process is already ongoing. Although this effect is expected to be small compared to the other heat sources, cement is known to release heat during the hydration process [19].

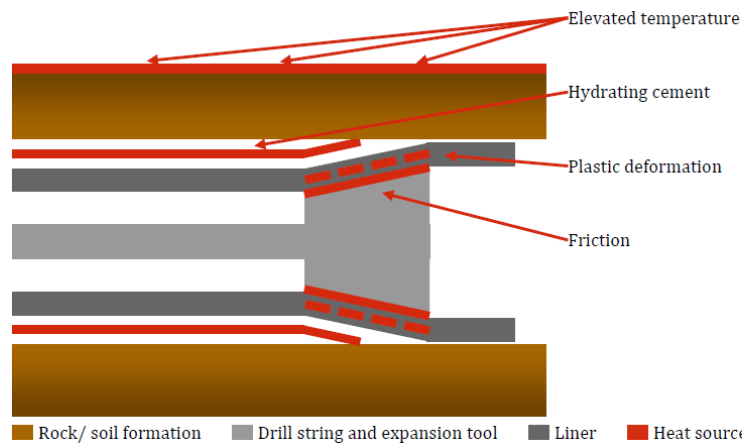


Figure 1.3: During expansion heat is generated from three different sources, friction, plastic deformation and hydration of cement. The figure illustrates the location of each of these heat sources. Furthermore, the figure highlights the elevated temperature at down hole conditions which can be seen as a boundary condition imposed on the system.

1.4. Objective

Currently, the temperature increase during the expansion process has been estimated based merely on a few experiments combined with a large safety margin. Consequently, for some projects expandable technology may be considered too risky or the speed of expansion may be unnecessarily slow. The aim of this research is to develop a thorough understanding of the thermal behavior of the expansion process and provide a numerical model which can adequately predict the temperature distribution along the contact of the cone and the liner. This model should be able to simulate any combination of expansion parameters, cone- and liner type. Furthermore, it is the aim to validate the model through full scale experiments.

1.5. Research approach

The aim is to approach the problem with a modular modeling method. The entire problem is divided into smaller sub-problems which are each first solved analytically, if necessary for a simplified case or geometry. Next a numerical version is derived which can deal with all geometries considered and non-uniformities such as temperature dependent material characteristics. Finally these solutions are combined into one multi-physics numerical model which can solve the time transient temperature distribution during the expansion process.

The model will be developed for a base (reference) case configuration which is representative for a field expansion. Later the model can then be adjusted to cope with other geometries and materials for specific well configurations. Based on the conditions of this base case, but adjusted to the equipment and materials available at the Shell Rijswijk laboratories, a test case is derived which is used to experimentally validate the model.

2

Scope & Literature

2.1. Scope

The objective of this research is to determine the peak contact temperature of the lubricant during the expansion process. This will require transient thermal analysis of the expansion process. The location of the heat sources from friction, plastic deformation and hydration is more or less known. The scope of this research is therefore limited to a region around the cone large enough to capture all these heat sources but not extended to the thermal analysis of an entire well. The scope is qualitatively shown in Figure 2.1. The scope is a relative frame which follows the movement of the cone during the expansion process, so that there is an in- and outflow of the liner at the boundaries of the frame. Geometric details and material properties of the components within the scope, are given in Appendix A. In many cases, the material properties have been measured specifically for this research, the measuring procedures can be found in Appendix B.

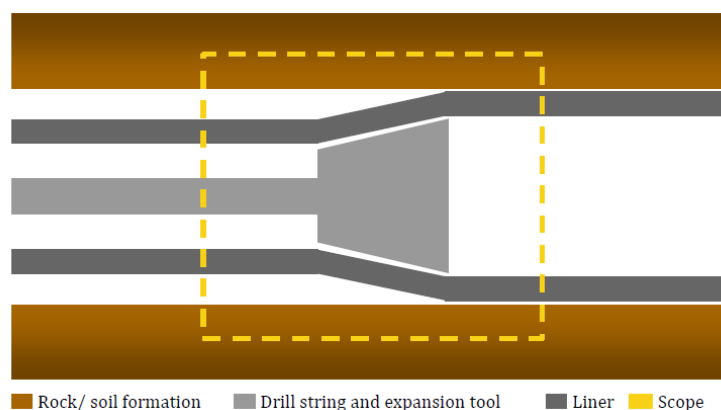


Figure 2.1: For the thermal analysis, a scope is selected relative to the movement of the cone during the expansion process. As the reference frame is moving in an absolute sense there is an in- and out flow of the liner at the boundaries. The scope includes the heat transfer from the liner to the formation.

A base case situation has been selected, this case represents one of the most common field configurations for the construction of mono-diameter wells. The base case describes the expansion of a single, VM50 type, liner and the overlap expansion of a VM50 liner with a P110 overlap liner, at a speed of $0.1[\frac{m}{s}]$. The full details of the base case are given in Appendix I. This base case is used to develop a numerical model and all numbers in this report will be in correspondence with this base case unless stated otherwise. The model is able to cope with other situations with different materials, geometries, expansion & well parameters, allowing the analysis of specific well configurations.

Next to the base case, also a test case is used, as described in Appendix J. This case is identical to the base case in terms of the components, but the expansion parameters coincide with the specifications of the equipment available at the Shell laboratory in Rijswijk. The test case is used to experimentally verify the model.

2.2. Scientific Literature

In a scientific context this research combines the fields of tribology and solid mechanics with heat transfer. All fields are extensively covered in literature, the combination of all three in one specific case is however unique. This research can be seen as a spider completing the center of a existing web of knowledge.

Tribology

The link with the field of tribology is evident, in any problem with friction or sliding contact surfaces heat is generated at their shared boundary. In most cases one of the sliding bodies is stationary with respect to the contact area while the other moves. In it's most simple form this could be seen as a heat source, not another body, of a defined heat flux per unit area, moving over a semi-infinite solid. The first systematic study of such problems was conducted by Jaeger in 1942 [14]. In his paper Jaeger analyzes the effect of the shape and intensity of a moving heat source on the temperature distribution inside a semi-infinite solid. He provides analytical equations for the temperature distribution inside the semi-infinite solid as a function of the heat source, speed of movement and the thermal properties of the solid. Hou and Komanduri, build on Jaegers research and derive generalized equations for both moving and steady state heat sources [12]. They also define a relation between the intensity distribution of the heat source and the relative location of the peak temperature. Yevtushenko *et al* have analyzed the transient effects of a variable sliding speed on the temperature [36].

The research becomes more practical when not just a moving heat source is analyzed but it is applied to sliding problems with friction, Ashby *et al* analyze a pin-on-disk setup [3]. The equations they provide allow for the pin and disk to have different material properties and determine both the so called bulk- and flash temperature. This bulk temperature, is defined as the bulk surface temperature of the sliding contact. The flash temperature is the peak temperature obtained on the scale of the roughness of the material, where friction causes local plastic deformation. For the friction coefficient they use a coulomb friction model. In the book of Stribeck, published in 1903, already qualitative relations for the friction coefficient as a function of for instance the sliding speed or the contact pressure are described [29]. Unfortunately the only way to fit these relations to practical applications is through experiments with a specific lubricant.

Solid mechanics

The heat release from the plastic deformation of metals was first described by Taylor and Quinney in 1934 [30]. They analyzed the latent heat from cold working rods in torsion and defined the Taylor-Quinney coefficient, which describes the relationship between the amount of work done on a metal and the amount of energy retained in the form of heat. As of today for many applications, especially at high strain (-rates), it is more than satisfactory to assume an, experimentally determined, constant value for the Taylor Quinney coefficient. Such constants are provided abundantly in literature by researchers such as Rusinek [24, 27]. In 1991 Zehnder introduced a model which correlated the Taylor-Quinney coefficient to the strain [38]. From his model and corresponding experiments, he concludes that at low strains significantly less heat is dissipated in the form of heat during plastic deformation as compared to high strains. He reasons that the difference is stored in the material in the form of dislocation multiplication. Further (experimental) research, by for instance Mason *et al* and Zaera *et al* has provided evidence for Zehnders model and also indicates a correlation with the strain rate [21, 37].

Heat transfer

Conduction of heat is a well described phenomenon, for basic geometries plenty full of analytical solutions are available which even cover transient effects. The book Basic Heat & Mass Transfer by Mills covers most of these methods [1]. When dealing with more complicated geometries and other non-uniformities numerical methods can provide a solution. Research such as that by Lyra *et al* shows how the finite volume method can be applied to solve a cylindrical heat transfer problem [20].

2.3. Previous work with Shell

Mono-diameter technology has already been used in the field and hence a lot of research has already been done in the past. Previous research has focused mainly on the mechanical aspects of the plastic deformation and the reduction of the expansion force, through the optimization of the cone geometry or selection of an alternative lubricant. This research is the first to investigate the thermal aspects of the expansion process. The process is known to generate heat and in some previous experiments temperatures have been measured, however no in depth investigation has yet been conducted. This work builds on two previous Msc. thesis written by students from the university of Twente, both are briefly described below.

Experimental and theoretical modeling of ironing during tubular expansion - Wilmink

In his thesis Wilmink has analyzed the impact of high external pressures, in a well, on the thinning of the liner wall during the expansion process [35]. Very high external pressures can lead to an effect described as ironing, where the expanded liner is elongated during the expansion process. Severe elongation could lead to significant reduction of liners wall thickness and hence collapse strength. To investigate this phenomenon Wilmink developed a mathematical model, which calculates the strains in the liner under laboratory and down hole conditions. The model is thereafter validated by FEM analysis and small scale experiments.

Relevant for this research, is Wilmink's mathematical model for the calculation of the strains in the liner and his method for the correction of liner material properties at elevated temperatures. Additionally the pressure profile on the cone was also determined in close correlation with this work.

A study to the lubrication of expansion processes for high temperature wells - Brinkhuis

Brinkhuis has investigated the working principle of the lubricant (RPSLF) under different conditions with the temperature as one of the main focus points [7]. A two stage melting process of RPSLF was identified that starts around 83°C with the softening of calcium stearate and continues up to 124°C when the polyethylene wax melts. Brinkhuis concluded that the temperature is a very important factor in the lubrication of the expansion process. He found that when the contact temperature is in between the two melting points the RPSLF is able to form a film which is strong enough to separate the cone and the liner and hence provide hydrodynamic lubrication. He finishes with a theoretical model based on the Reynolds equation to calculate the pressure and thickness of the lubricant film at different ambient temperatures.

The key take away from Brinkhuis' research is the strong correlation between the temperature and friction coefficient when using RPSLF as a lubricant, this serves as a direct input for the thermal model. Furthermore the theory behind the lubrication film can be used to explain some of the experimental results.

3

Heat sources

A too high lubricant temperature and thereby decomposition of the lubricant is one of the failure mechanisms of the expansion process. During expansion, the elevated down hole temperature is further increased by heat from three different sources as shown in Figure 3.1. Most of the work done on a system, especially with friction involved, is converted into heat. This work,

$$W = Fv, \quad (3.1)$$

is correlated to a force F , which is applied on a system to maintain a constant speed, v . First, the heat generated due to friction is described in Section 3.1. Section 3.2 describes heat generation due to plastic deformation. The heat release from hydrating cement is discussed in Section 3.3 and an indication for the down hole temperature is given in Section 3.4.

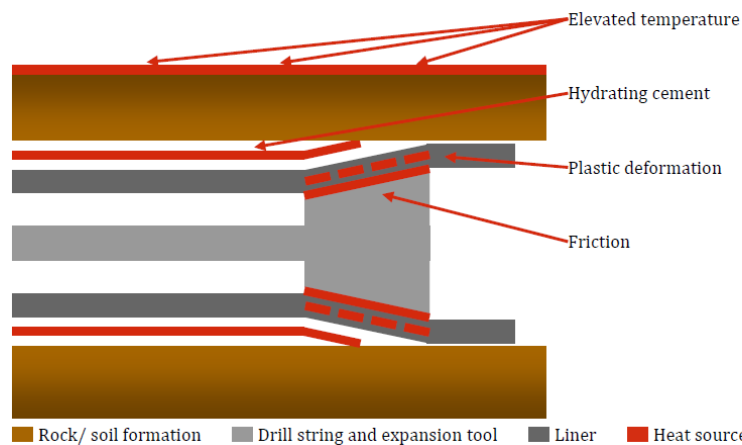


Figure 3.1: During expansion heat is generated from three different sources, friction, plastic deformation and hydration of cement. The figure illustrates the location of each of these heat sources. Furthermore, the figure highlights the elevated temperature at down hole conditions which can be seen as a boundary condition imposed on the system.

3.1. Friction

A significant amount of heat is generated due to friction between the cone and the liner. Heat generation due to friction between sliding contact surfaces has been studied extensively in the past. Ashby *et al.* [3] provide a simple equation for the heat generated by friction per unit area:

$$q_{fr} = \mu P v, \quad (3.2)$$

here μ is the friction coefficient, P the contact pressure and v the relative speed between the sliding bodies. Typically, it is assumed that the RPSLF gives a constant friction factor of $\mu = 0.065[-]$ [10]. This friction factor can vary significantly with the temperature. Brinkhuis has conducted test using the ball on three flats method

to determine the friction coefficient of RPSLF at different temperatures [6, 7]. The resulting profile for the friction coefficient as a function of the temperature is shown in Figure 3.2.

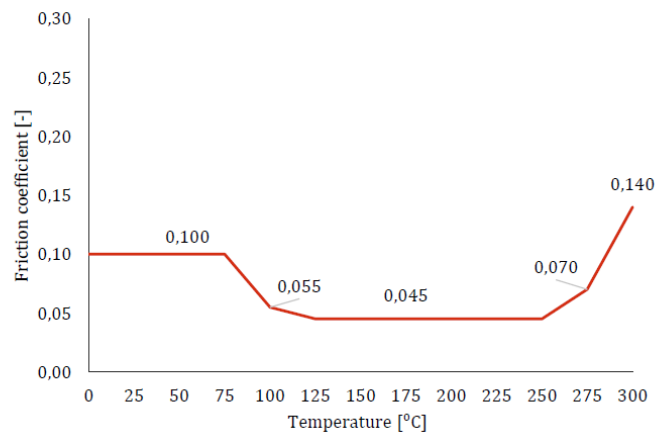


Figure 3.2: Friction coefficient of the lubricant (RPSLF) as a function of the temperature determined, experimentally by Brinkhuis using the ball on three flats method [7]. The friction coefficient decreases when components of the lubricant begin to melt and rapidly increases again when the decomposition temperature is reached.

It is well known that the contact pressure can also influence the friction coefficient of a sliding system. The Stribeck curve describes this relation qualitatively with three different lubrication regimes [29]. At high pressures, the friction coefficient is high in the so called boundary lubrication regime, as the pressure decreases the friction coefficient decreases into the mixed lubrication regime. Finally, at low pressures a minimum of the friction coefficient is found after which friction remains low although a slight increase is possible in the hydrodynamic lubrication regime. It is very well possible that different lubrication regimes coexist over the contact area. To gain some preliminary insight in this phenomenon the friction coefficient has been measured at different loads as shown in Figure 3.3. The mean load of this test corresponds to a contact pressure between 450 and 770 [MPa]. The increase of the friction coefficient at very low pressures is due to the lack of popper contact.

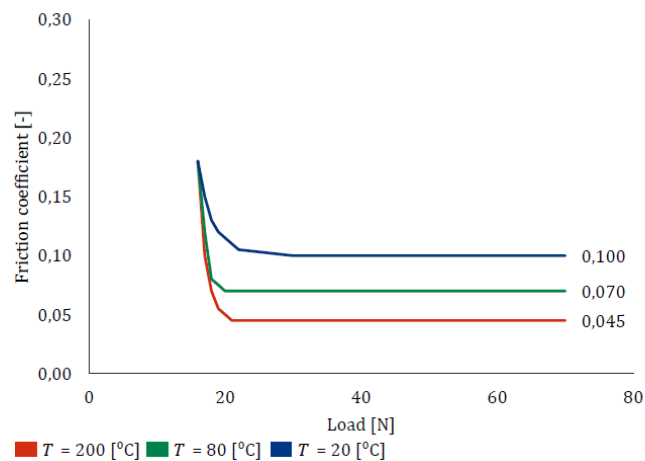


Figure 3.3: Friction coefficient of the lubricant (RPSLF) as a function of the contact pressure represented by the force on the test ball. The Stribeck curve qualitatively describes a variation of the friction coefficient with the pressure. The experimental results shown in the figure show that, at higher pressures this relationship is much weaker than the relationship with the temperature.

The pressure on the cone, along the contact with the liner, is expected to have a non-uniform distribution due to the combination of expansion and bending in the liner. A peak pressure is expected at the location where the liner comes into contact with the cone, here a bending moment is exerted on the liner, this peak is known as the front peak. After the front peak the diameter of the liner is increased linearly, this large section with a relatively low pressure is known as the linear section. The pressure profile is concluded with the rear peak which is again caused by a bending in the liner as it is straightened at the round-off of the cone.

A lot of work has been done in the past in an attempt to gain an understanding of this pressure profile [2, 16, 35]. The profile which is currently used was determined by 4RealSim, in research commissioned by Shell, in this study the pressure profile over the length of the cone has been numerically determined using an Abaqus FEA model, the result is shown in Figure 3.4. Care should be taken when using this pressure profile as the result is mesh dependent and when the expansion force is calculated based on this pressure profile the results overestimate this force by around 10%, indicating that the pressures are likely a bit too high. As no better alternative is currently available the pressure profile is seen as a working hypothesis and attempts will be made to (partially) validate it later by means of experiments.

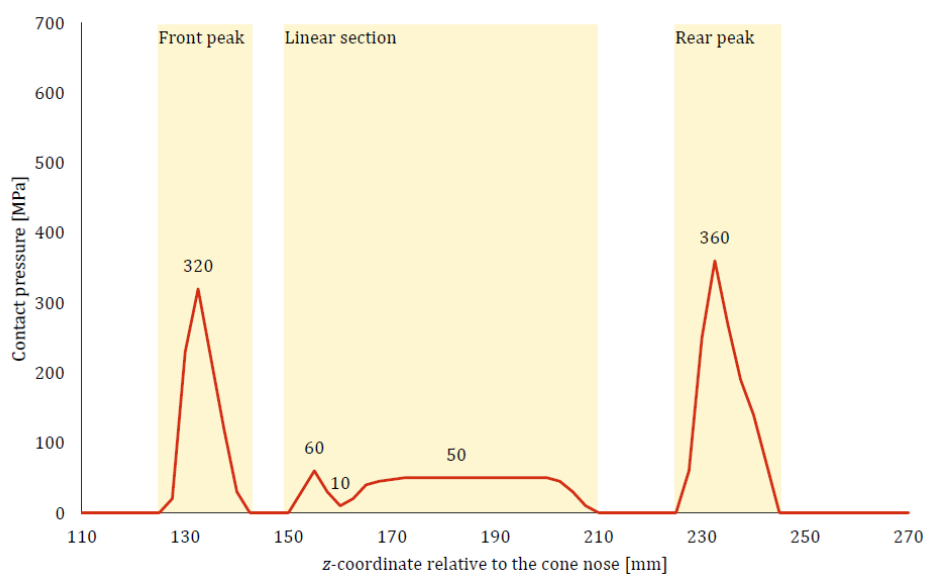


Figure 3.4: Pressure profile over the length of a 10.2" cone during single liner expansion as determined by 4RealSim using an unvalidated Abaqus FEA model. The front peak is caused by bending of the liner as it comes into contact with the cone. At the linear section the diameter of the liner is increased. Finally, the rear peak is caused by straightening of the pipe at the round-off of the cone.

During expansion of an overlap section, the pressure profile changes significantly as compared to the single liner expansion. Not only is it higher in absolute terms, but due to the location where the overlap liner comes into contact with the single liner the location of the rear pressure peak is also altered. The pressure profile during overlap expansion as calculated by 4RealSim is shown in Figure 3.5.

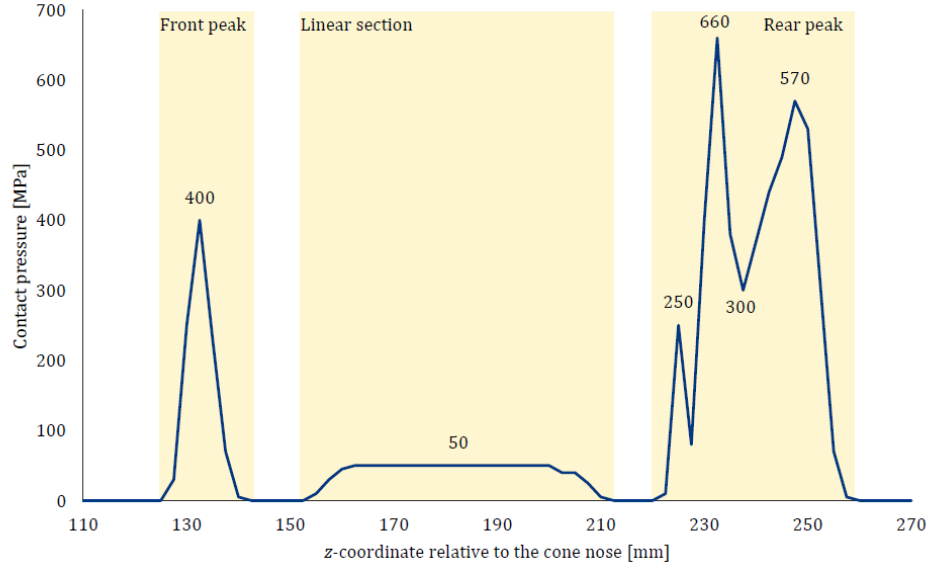


Figure 3.5: Pressure profile over the length of a 10.2" cone during overlap expansion as determined by 4RealSim using an unvalidated Abaqus FEA model. Especially the rear peak is significantly higher during overlap expansion as compared to single expansion. The pressure only builds up here as the point of first contact with the overlap liner is located only just before the round-off.

When this pressure profile is inserted into Equation 3.2 which is then integrated over the surface area of the cone the total heat release related to friction, Q_{fr} at the surface of the cone, can be calculated using;

$$Q_{fr} = \oint \mu(T)P(z)v_{ex}dA, \quad (3.3)$$

here $\mu(T)$ represents the temperature dependent friction coefficient as defined in Figure 3.2, $P(z)$ is the pressure profile and v_{ex} the expansion speed. For the base case the total initial frictional heat is $Q_{fr} = 46.7$ [kW]. Finally, the expansion force due to friction, F_{fr} can be calculated as;

$$F_{fr} = \frac{Q_{fr}}{v_{ex}}. \quad (3.4)$$

The expansion force related to the friction is $F_{fr} = 467$ [kN].

3.2. Plastic deformation

When analyzing heat transfer in combination with plastic deformation, the material's Taylor-Quinney coefficient,

$$\beta = \frac{Q_{de}}{W_{de}}, \quad (3.5)$$

must be known [30]. As shown by Equation 3.5 the Taylor-Quinney coefficient gives the relationship between the amount of work done to plastically deform a material, W_{de} and the amount of heat generated, Q_{de} . The fraction of the work not converted into heat is stored in the material as strain energy due to dislocations, dislocation interactions and residual strains caused by incompatible slip in grains of a different orientation [38]. At relatively high strain, values for the Taylor-Quinney coefficient can be found abundantly in the literature. For steels typically a value of $\beta = 0.9$ [-] is used [27]. At very low strain or very low strain (-rates) assuming a constant value for the Taylor-Quinney coefficient results in a significant error. This is caused by the fact that, at very low strain (-rates) more energy is stored inside the material in the form of dislocations or metallurgical transformations as compared to high strain (rates). Zehnder has proposed a model to estimate the Taylor-Quinney coefficient based on power law stress-strain behavior [38]. This model is given by;

$$n_z = \frac{1}{n}, \quad (3.6)$$

$$K(\varepsilon_p) = n_z \frac{\varepsilon_p^{n_z-1}}{\varepsilon_0^{n_z}}, \quad (3.7)$$

$$\beta(\varepsilon) = \frac{Q_{de}}{W_{de}} = \frac{K(\varepsilon_p) - C}{K(\varepsilon_p)}. \quad (3.8)$$

In these equations n is the power law hardening exponent of the material, ε_p the plastic strain, ε_0 the strain at the yield point and C a numerical constant. Zhender proposes that in order to fit his model to a certain material one should do several experiments and chose the constant C (in the order of 10) such that the curve generated by his model fits the experiments. A method for such experiments is described by Perez-Castellanos & Rusinek [24]. These experiments require very accurate and high-speed thermal imaging cameras which were unfortunately not available at Shell. The choice was therefore made to select the constant C so that the known high strain Taylor-Quinney coefficient of $\beta = 0.9$ [-] is found. A value of $C = 15$ [-] was found suitable for this purpose. the resulting relationship between the strain and the Taylor-Quinney coefficient of VM50 and P110 is shown in Figure 3.6. As the dependency of the Taylor-Quinney coefficient on the strain rate is typically a lot weaker the choice is made to ignore this relationship and assume it as constant.

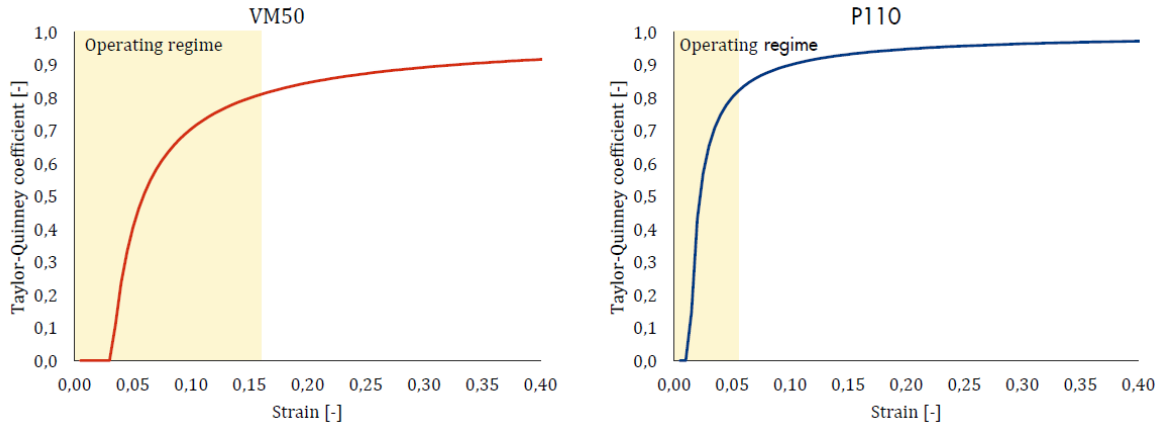


Figure 3.6: Strain dependent Taylor-Quinney coefficient of VM50 (single liner) and P110 (overlap liner) based on the Zhender model using $C = 15$ [-]. It is seen that before the yield strain is reached the Taylor-Quinney coefficient is 0 [-], after which it increases according to Equation 3.8.

Next the amount of energy needed to plastically deform the liner per unit volume is calculated, represented by U in [$\frac{J}{m^3}$]. This is done by integrating the stress strain curve over the strain interval of the deformation as

$$U = \int \sigma d\varepsilon, \quad (3.9)$$

here σ is the stress and ε the strain. The stress/strain behavior of the liner materials is defined using a Swift law stress/strain curve. This is described in more detail in Appendix A.2 for VM50 and A.3 for P110. Most of the strain inside the liner will be in the hoop direction, θ , however as volume is conserved strain also exists in other directions depending on the mode of expansion. These strains,

$$\varepsilon_\theta = \ln\left(\frac{r}{r_0}\right), \quad (3.10)$$

$$\varepsilon_r = \rho \varepsilon_\theta, \quad (3.11)$$

$$\varepsilon_z = -\varepsilon_\theta - \varepsilon_r, \quad (3.12)$$

have been determined by Wilmlink for each expansion mode [35]. Here ε_r represents the radial strain, ε_z the axial strain and ρ parameter depending on the expansion mode. The parameter ρ in Equation 3.11 has been determined experimentally by Wilmlink. The value of ρ for each expansion mode is shown in Table 3.1.

Table 3.1: Relationship between the hoop and radial strain for different expansion modes assuming "free" expansion

Expansion mode	ρ
Compression	-0.47
Tension	-0.74
Fixed-Fixed	-1.00

The equivalent strain, ε_e , follows through a von-Mises strain approximation such that:

$$\varepsilon_e = \sqrt{\frac{2}{3} (\varepsilon_\theta^2 + \varepsilon_r^2 + \varepsilon_z^2)}. \quad (3.13)$$

As both the material stress and the Taylor-Quinney coefficient are related to the strain, the heating due to plastic deformation is strongly correlated to the local increase in the strain. Figure 3.7 shows the distribution of the strain during an overlap expansion. The strain in the inner (single) liner is unaffected by the presence of the overlap liner.

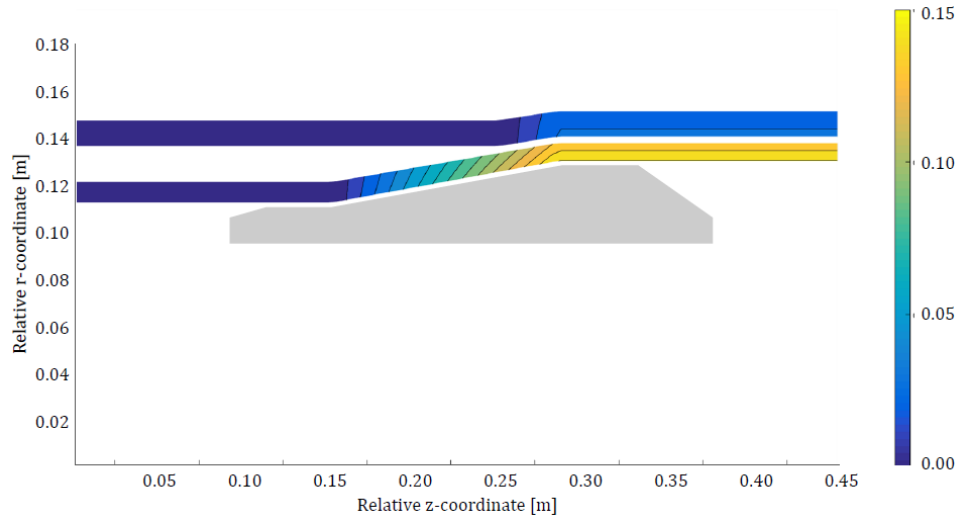


Figure 3.7: Strain distribution in the single liner and overlap liner during expansion . As the diameter of the liner is increased the strain increases correspondingly. At the inside of the liner the expansion ratio is slightly larger than at the outside, hence a slightly higher strain is seen at the inside.

When the strain, work and Taylor-Quinney coefficient are determined, the heat source from plastic deformation is calculated by

$$Q_{de} = V \frac{v_{ex}}{L} \beta(\varepsilon) \int \sigma d\varepsilon. \quad (3.14)$$

where the length scale L represents the length of the liner over which the plastic deformation takes place and V the volume of the liner which is being deformed. The heat release due to plastic deformation in the reference case is $Q_{de} = 20.2[\text{kW}]$. Parallel to the expansion force related to friction also the expansion force related to plastic deformation, F_{de} , can then be calculated

$$F_{de} = \frac{1}{v_{ex}} \iiint_V \frac{s_{de}(r,z)}{\beta(\varepsilon)} dV, \quad (3.15)$$

an extra correction needs to be introduced for the Taylor-Quinney coefficient as shown by Equation 3.15, where s_{de} represents the local volumetric heat generation due to plastic deformation in $[\frac{\text{W}}{\text{m}^3}]$. The expansion force related to plastic deformation is 489[kN] The total expansion force is then calculated by a summation of the expansion force due to friction and plastic deformation;

$$F_{ex} = F_{de} + F_{fr}. \quad (3.16)$$

The combined forces lead to total initial expansion force of the base case is 956[kN].

3.3. Hydrating cement

It is well known that the hydration (or curing) of cement is an exothermic reaction. Around the liner a layer of cement is set which is curing during the expansion process and thus acts as a heat source on the outer surface of the liner.

Typically the drilled well hole has a radius of around 50[mm] larger than the liner to be inserted, this area is filled with cement. The volume of hydrating cement, V_{ce} , around the cone can thus be calculated as:

$$V_{ce} = L_{co}\pi(r_{we}^2 - r_{li}^2), \quad (3.17)$$

where L_{co} is the length of the cone, r_{we} die radius of the well and r_{li} the outer radius of the liner. The maximum density of cement is around 2000 [$\frac{\text{kg}}{\text{m}^3}$] and the maximum heat release of hydration per unit mass is around $s_{hy} = 20$ [$\frac{\text{W}}{\text{kg}}$] [19]. Then the expected maximum heat release of the cement relative to the cone is calculated by

$$Q_{ce} = V_{ce}\rho_{ce}s_{hy}. \quad (3.18)$$

For the base case, this heat source is no more than 0.24[kW]. Considering the 20.2[kW] from plastic deformation and 46.7[kW] from friction, the heat release from cement only contributes 0.36% of the total heat input in the system, it is therefore neglected.

3.4. Elevated temperature

Although not strictly a heat source, it must be noted that at down hole conditions the typical temperature is around 80[°C]. This elevated temperature must be considered in the model as it influences the friction coefficient and material properties. The table below gives a summary of some recent wells in which mono-diameter technology was used with their respective down hole temperatures.

Table 3.2: Recent wells in which mono-diameter technology was used, with the year in which the expansion was executed and the down hole temperature at the depth of the expansion

Well	year	Down hole temperature [°C]
King MC-764	2016	82
Ui2	2015	85
P8	2015	84
Pi1	2014	90

4

Modeling method

To obtain maximal flexibility in modeling and gain a true understanding of the problem, the choice is made not to use commercially available modeling software, such as ANSYS fluent or Abaqus, but build the model from scratch in Matlab. Modeling the entire problem in 3D would require a very large computational domain and add many terms to the heat transfer equations. As conduction of heat is uniform in all directions and the shape of the cone has no significant variations in the circumferential direction, an axis symmetric model is used. An analytical derivation of the conduction of heat is given in Appendix C and a high-level flowchart of the model is available in Appendix D.

As multiple solution methods are available, in Section 4.1 a simple calculation is done to verify the functionality of these methods on a cylindrical heat transfer model. The selected method is then explained in further detail. Section 4.2 describes the type of mesh used and how it is fit to the geometries. A time integration method is selected in Section 4.3. In Section 4.4 the numerical stability is verified. Movement of the cone requires some specific modeling, this is described in Section 4.5. Finally, a method to calculate the thermal gradients on a non-orthogonal grid is proposed in Section 4.6.

4.1. Solution Method

Two of the main types of solution methods used for solving heat transfer problems are the finite difference method, which solves the differential equations directly, and the finite volume method which uses an integral form of the differential equation. To prove the validity of these methods for this type of problem, a simple calculation is done. For this calculation, a steel cylinder is chosen to be of a uniform temperature of $T = 0[^\circ\text{C}]$ at $t = 0[\text{s}]$. Then the outer boundary of the system is set to $T = 100[^\circ\text{C}]$ and the heating of the cylinder with respect to the radial coordinate and the time is analyzed. Furthermore, all the properties of the cylinder are assumed to be independent of the temperature.

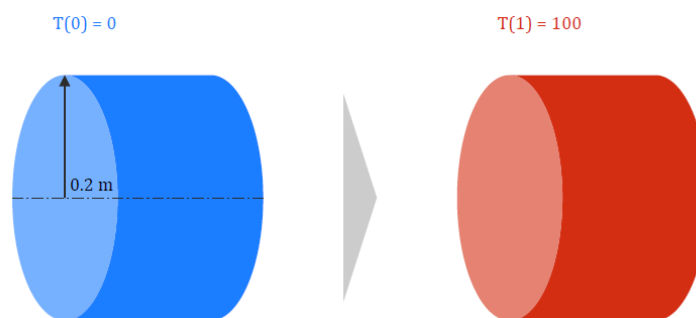


Figure 4.1: Setup of the test calculation to verify the validity of the FV and FD solution methods. The setup is based on a cylinder with a radius of 0.2[m], initially at $T = 0[^\circ\text{C}]$ everywhere. Then the outer surface temperature is set to $T = 100[^\circ\text{C}]$ and the radial temperature distribution is analyzed.

In Appendix C, an analytical expression for the time transient temperature distribution of this problem has

been derived. This solution is compared to the results of the Finite Volume and Finite Difference methods as shown in Figure 4.2.

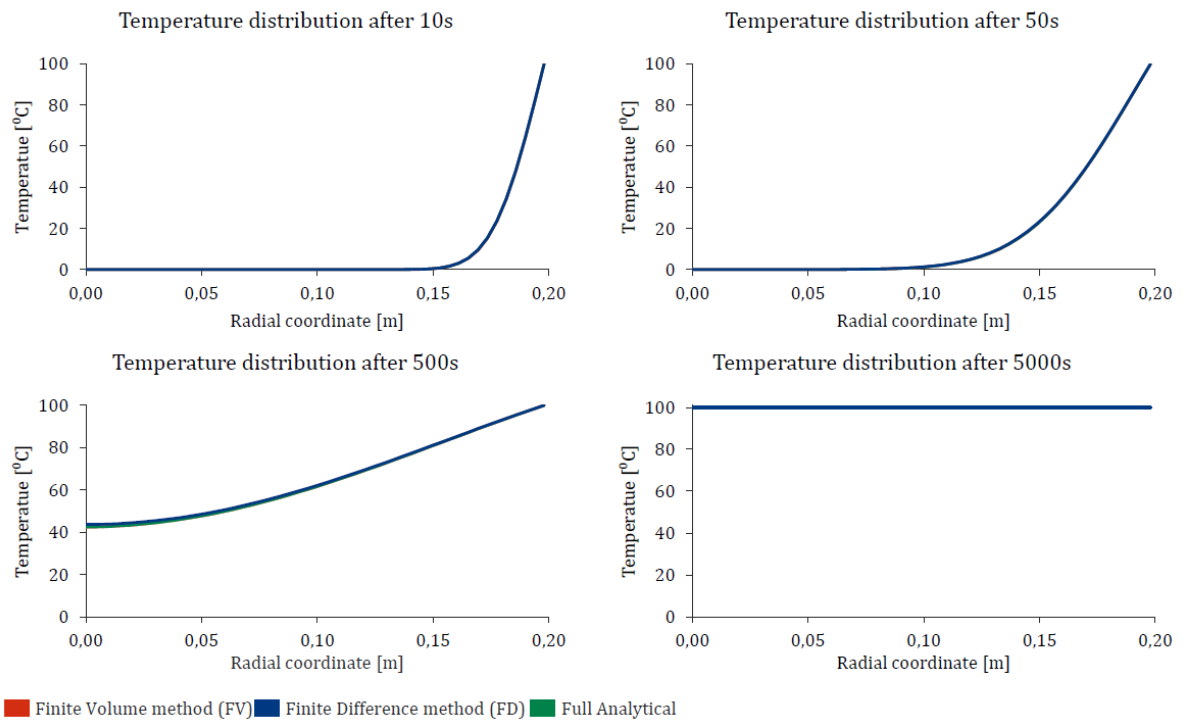


Figure 4.2: The temperature distribution along the r -coordinate of the test calculations is shown at four different moments in time. Both the FV and FD method match the analytical solution everywhere and at any time.

The results are identical, hence the finite volume method is selected as the (relatively) simple formulation of the surface heat fluxes allows for the use of unstructured grids which are necessary to adequately represent the geometry. In principle the finite volume method considers a cell, or small volume, in which all properties are assumed to be constant. Adjacent cells may have different properties and this difference can provide a driving force for a flux or flow of heat on the boundary between two cells. In this specific case a heat transfer problem is considered with the temperature as the main driving parameter. If, in Figure 4.3, the temperature is higher in the left cell, than in the right cell heat will flow across their shared boundary from the left cell to the right cell at a rate determined by the temperature and other properties, such as the dimensions of the cells and their thermal conductivities.

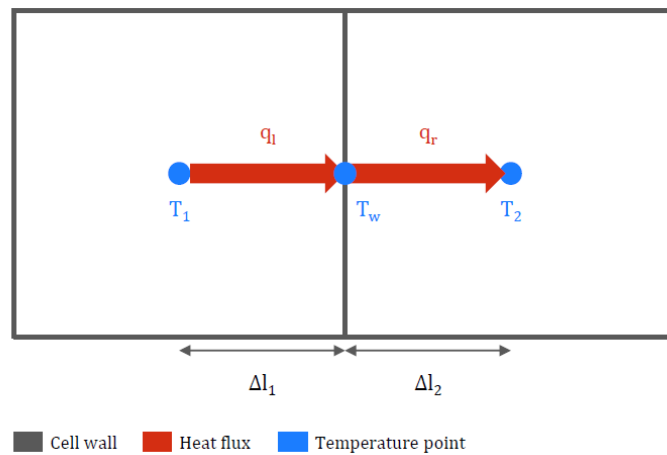


Figure 4.3: Schematic of a heat flux using the finite volume method. When the temperature of the left cell T_1 is higher than the right cell T_2 , heat will flow from the left to the right. The amount of heat leaving the cell on the left, must always be equal to the amount of heat entering the cell on the right (heat conservation).

Once the heat fluxes between all the cells have been calculated and boundary conditions have been taken into account, the total flow of heat from a single cell follows from a summation of these heat fluxes. This summation, accompanied by the thermal capacity of the cell allows a calculation of the change of temperature, T , over a considered time increment, Δt . The heat balance is given by

$$T(t + \Delta t) = T(t) + \Delta t \frac{\sum_i q_i A_i + sV}{\rho V C_p}, \quad (4.1)$$

here \sum_i denotes the summation of all heat fluxes, q_i , multiplied by their corresponding area, A_i . Furthermore, s , is a volumetric heat source multiplied by the cell volume, V . The heat capacity of the cell is given by the density, ρ , the cell volume and specific heat, C_p .

4.2. Mesh

To use the finite volume method, the entire domain must be divided into small volumes (cells). The size of these cells must be chosen sufficiently small so that the required resolution in the final solution is obtained. However, smaller cells means more cells must be used and the time integration must use smaller time steps leading to much slower computation (see Section 4.4 for more details). Finally, the solution should be independent of the type and size of mesh chosen.

Cell type

The mesh is constructed using skewed quadrilateral cells as illustrated in Figure 4.4. The vertical edges on the left and right simplify the calculation of the East and West, (denoted by E and W) heat fluxes. The more complex skewed lines on the North and South of the cells are required to fit the geometry.

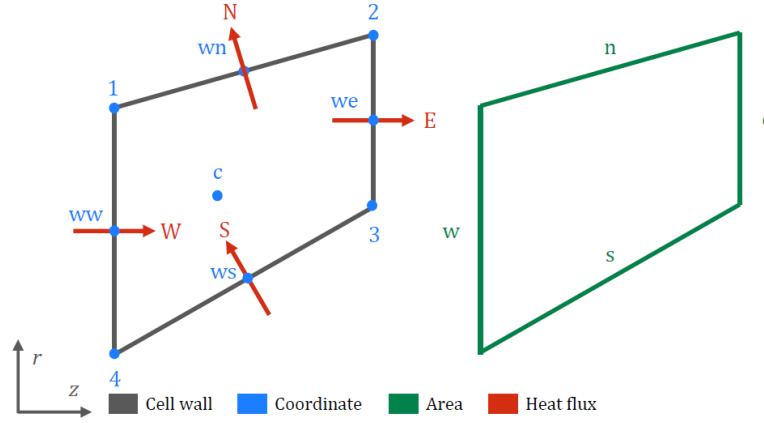


Figure 4.4: Basic shape and properties of the cells. The skewed grid cells are geometrically defined by 4 corner points ($1, 2, 3, 4$) shown in blue, 4 centers of the cell walls (wn, we, ws, ww) also shown in blue, 4 area's of the cell walls (n, e, s, w) shown in green and the cell center of mass c , again shown in blue. The position and positive direction of the heat fluxes is shown in red and denoted by (N, E, S, W).

For every cell a number of points, areas and a volume need to be defined. Their physical location with respect to the cell and naming are shown in Figure 4.4. The grid generator first defines the coordinates of the corners of the cells (points 1 to 4), after which the centers of the walls follow easily. The coordinates of the center of mass of a trapezoid with two parallel sides are given by

$$\bar{z} = \frac{b}{2} + \frac{(2a+b)(c^2-d^2)}{6(b^2-a^2)}, \quad (4.2)$$

$$\bar{r} = \frac{b+2a}{3(a+b)}h, \quad (4.3)$$

where the variables a, b, c, d, h are consistent with Figure 4.5. As the cells are represented by a trapezoid in the 2D r, z space, these equations are used to determine the center of mass of the cells.

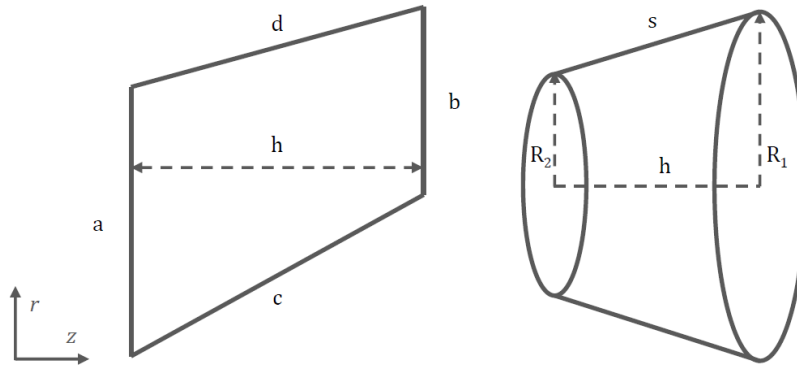


Figure 4.5: Reference shape of a trapezoid (left) used for the calculation of the cell center of mass. On the right the reference shape of a cone used to calculate the north and south cell area's.

As a cylindrical coordinate system is used, the east and west areas of a cell are trivial to calculate as they are represented by a ring shape. Hence, the east area is equal to;

$$A_e = \pi(r_1^2 - r_2^2), \quad (4.4)$$

here r_1 and r_2 correspond to the radial cell coordinates of the corners as defined in Figure 4.4. The north and south surfaces are represented by the sides of a conical segment and must therefore be calculated by

$$A_n = \pi(R_1 + R_2)\sqrt{(R_1 - R_2)^2 + h^2}, \quad (4.5)$$

where R_1, R_2 and h correspond to the definition set by Figure 4.5. The cell surface A_n is the outer surface of the conical segment s .

4.2.1. Fitting the mesh to the geometry

Naturally it is of major importance that the mesh has a good fit with the geometry. Using the simplified geometry, derived in Appendix A.1.1, the domain is divided into a total of 10 or 14 sections, 5 for the cone, 5 for the liner and if applicable 4 for the overlap as shown in Figure 4.6.

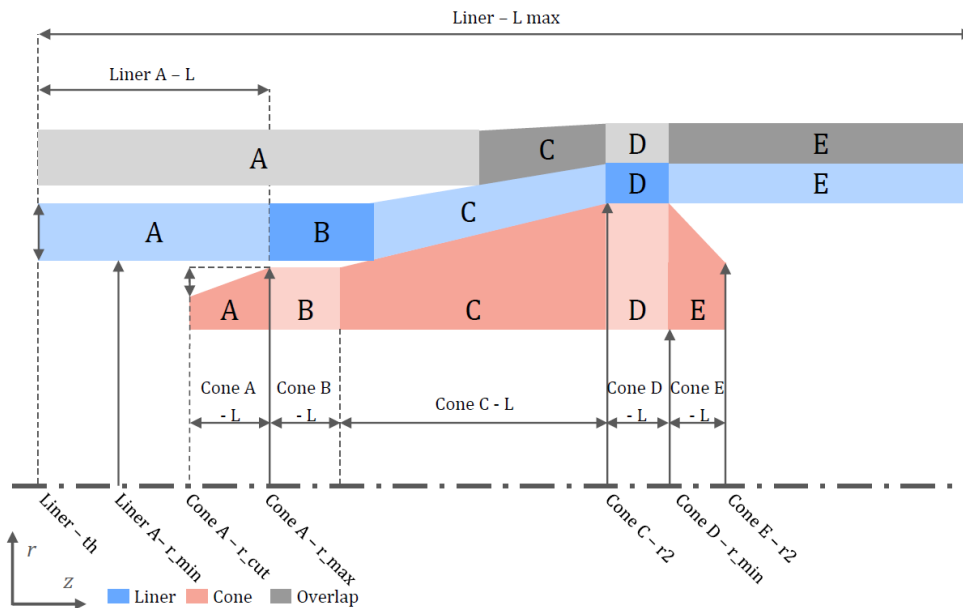


Figure 4.6: The figure shows the 14 sections with corresponding dimensions that are used to define the geometry of the components. In Sections C and D there is contact between the cone and the liner and the grid cells must therefore be aligned in the z -direction. In sections C, D and E there is contact between the liner and the overlap liner, hence alignment in the z -direction is also crucial.

In order to ensure good contact between the cone and the liner, the mesh of these components must be in perfect alignment in the sections C and D. Here the width of the cells (z -direction) must be identical for the cone and the liner, a difference between sections C and D is allowed to ensure a good fit with the geometry. In section A, B and E the width is chosen solely so that there is a good fit with the geometry as no contact with other components exists. In all cases the maximum allowable size of grid cells in the z -direction is set to 3.0[mm]. The radial coordinates require a different treatment. Here no match is required between the cone and the liner but adjustments need to be made with the changing radii along the z -direction. Additionally the choice is made to use bias factors in both the cone and the liner so that extra detail can be added in the mesh near to the contact surface. A bias factor defines the growth rate of cells in along a certain axis. In the liner a single sided bias factor of 1.3[-] is used, along the r -axis, with the maximum cell height on the outside of the liner of 3.5[mm]. In the cone a single bias factor of 1.2[-] is used, also along the r -axis, so that the largest cells are located at the bottom, the maximum height is set to 7.5[mm]. The resulting mesh is shown in Figure 4.7.

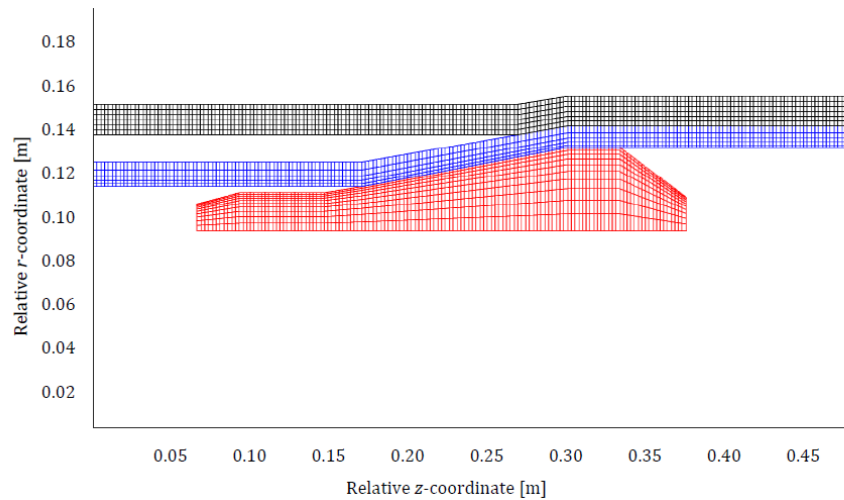


Figure 4.7: Mesh used for the base case simulations constructed with 1165 cells. Bias factors are used in the cone and the liner to refine the grid near the contact surface between the cone and the liner.

The model is run with different values for the maximum cell sizes and bias factors to prove that although the resolution may vary, the result of the model in general terms is unaffected by the mesh size. Figure 4.8 shows the peak contact temperature with different sizes of the mesh.

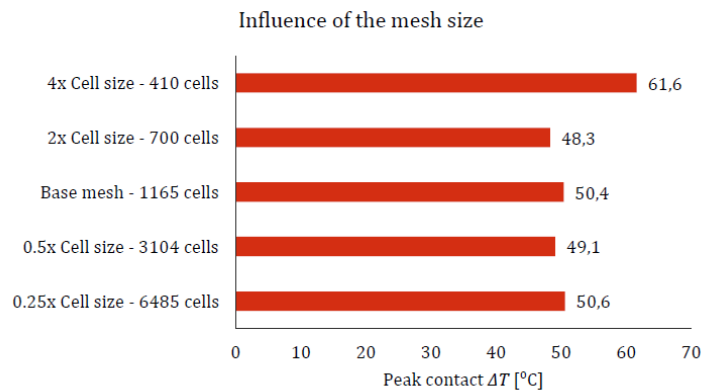


Figure 4.8: The base case has been simulated with different mesh sizes to verify that the mesh size does not have a significant impact on the peak contact temperature. Above around 1000 cells the variation in the peak contact temperature is negligible.

Some variation is visible between the different mesh sizes, mainly due to the mapping of the pressure profile on the cells at the contact between the cone and the liner. Nevertheless above around 1000 cells the variation is less than 2%. This variation is within the acceptable range and therefore the mesh with 1165 cells is used.

4.3. Time integration method

Numerous numerical methods are available to compute the temperature at the next time step, the simplest of them being the first order Forward Euler (FE) scheme;

$$\omega_{n+1} = \omega_n + \Delta t f(t_n, \omega_n), \quad (4.6)$$

where ω is the variable to be integrated in time, n the time step and $f(t_n, \omega_n)$ the derivative at the current time step [33]. When this the discretization in Equation 4.6 is applied to the Finite Volume method it transforms to;

$$T_{j,i}^{n+1} = T_{j,i}^n + \Delta t \frac{\sum q_{j,i}^n A_{j,i} + s_{j,i}^n V_{j,i}}{V_{j,i} \rho_{j,i} C p_{j,i}}. \quad (4.7)$$

The forward Euler scheme uses only the derivative and temperature at the current time step to approximate the temperature at the next time step. This scheme is very easy and fast to compute but lacks in accuracy and stability properties. Higher accuracy can be achieved with, for instance, the Adams Bashfort-2 method, which although still explicit gives second order accuracy. The increased accuracy comes at the cost of a tighter time step requirement for stability. This method is defined by;

$$\omega_{n+1} = \omega_n + \frac{3}{2}\Delta t f(t_n, \omega_n) - \frac{1}{2}\Delta t f(t_{n-1}, \omega_{n-1}). \quad (4.8)$$

When this the discretization in Equation 4.8 is applied to the Finite Volume method it transforms to;

$$T_{j,i}^{n+1} = T_{j,i}^n + \frac{3}{2}\Delta t \frac{\sum q_{j,i}^n A_{j,i} + s_{j,i}^n V_{j,i}}{V_{j,i} \rho_{j,i} C p_{j,i}} - \frac{1}{2}\Delta t \frac{\sum q_{j,i}^{n-1} A_{j,i} + s_{j,i}^{n-1} V_{j,i}}{V_{j,i} \rho_{j,i} C p_{j,i}}. \quad (4.9)$$

More complex numerical methods, like the second order implicit Cranck-Nicolson scheme, which is given by;

$$\omega_{n+1} = \omega_n + \frac{\Delta t}{2} (f(t_n, \omega_n) + f(t_{n+1}, \omega_{n+1})), \quad (4.10)$$

use temperatures and derivatives at other, even future, time steps [33]. These schemes can be inherently stable and provide much better accuracy but at a significant cost of computation-time. Generally speaking the use of such methods only pays off if a very high accuracy is required or a much larger time step can be used in comparison with explicit methods. When this the discretization in Equation 4.10 is applied to the Finite Volume method it transforms to

$$T_{j,i}^{n+1} = T_{j,i}^n + \frac{1}{2}\Delta t \left(\frac{\sum q_{j,i}^n A_{j,i} + s_{j,i}^n V_{j,i}}{V_{j,i} \rho_{j,i} C p_{j,i}} + \frac{\sum q_{j,i}^{n+1} A_{j,i} + s_{j,i}^{n+1} V_{j,i}}{V_{j,i} \rho_{j,i} C p_{j,i}} \right). \quad (4.11)$$

Once the time step is chosen sufficiently small so that a certain time integration method is stable, all of them give the same result as shown in Figure 4.9. All time integration methods are built into the model to allow future flexibility, for this research the Forward Euler method is used as it is the fastest to compute.

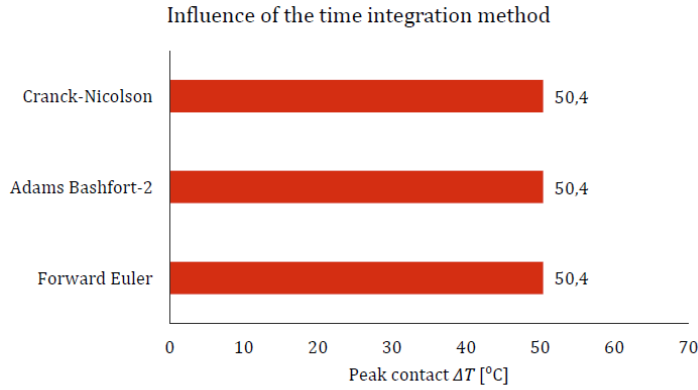


Figure 4.9: The base case model has been run with three different time integration methods. This figure shows that the peak contact temperature is unaffected by the time integration method. The Forward Euler method is used as it is the fastest to compute.

4.4. Numerical stability

Numerical methods, especially explicit schemes, are subject to instability and unphysical results if the chosen time step does not meet the criteria set by the grid and other properties of the model. Two main criteria can be identified to which the size of the time step must uphold.

Von Neuman criterion

The “Von Neuman” criterion which is given by

$$\frac{\Delta t \alpha}{\Delta r_{min}^2}, \frac{\Delta t \alpha}{\Delta z_{min}^2} \leq 0.5, \quad (4.12)$$

in which Δt is the time step, Δr_{min} and Δz_{min} are the minimum dimensions of a cell and α , the thermal diffusivity is given by

$$\alpha = \frac{k}{\rho C_p}. \quad (4.13)$$

Essentially, this criterion specifies that the distance the diffusing heat travels in one time step may not exceed the minimum length of any cell in any direction [33].

Courant number

The next criterion is the ‘‘Courant number’’ as described by

$$Cr = \frac{v_r \Delta t}{\Delta r_{min}}, \frac{v_z \Delta t}{\Delta z_{min}} \leq Cr_{max}, \quad (4.14)$$

in which Cr is the Courant number, which must be smaller than 1, v_r and v_z are the radial and axial components of the velocity. The Courant number specifies that, the speed of any fluid or moving part along a certain axis within a time step, may not be greater than the minimal length of a grid cell along that specific axis[15]. In the case considered this means that the speed of the cone per time step may not exceed the length of the smallest cell in the z -direction.

Minimum time step

The minimum time step given by the two criteria becomes the driving criterion for the entire domain. It is customary to use a time step of around 0.8 times the minimum time step found by the criteria to create a small safety margin. In the base case the von Neuman number is the driving criterion, a time step of 0.017[s] is used to remain in the stable region. Similar to the validation of the grid size and the time integration method it can also be shown that as soon as the time step is small enough the final result is independent of the time step chosen. Figure 4.10 shows the peak contact temperature for different time steps.

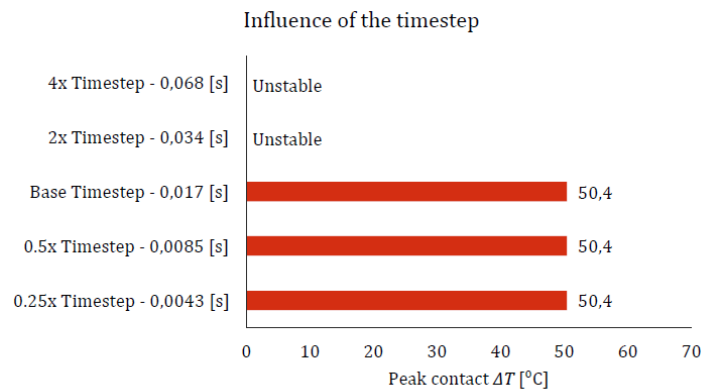


Figure 4.10: The base case has been simulated with different time steps. The calculated minimum time step for the base case is 0.017[s], hence the figure shows that larger time steps yield unstable results and any smaller time step does not influence the result.

4.5. Cone movement

The cone is moving while the liner is expanded, this movement means that the heat sources are at a fixed position relative to the cone but moving relative to the liner. Two methods are considered to model this phenomenon.

4.5.1. Moving cone, absolute reference frame

One could consider modeling this phenomenon by modeling a section of the liner and moving the cone along it whilst continuously adjusting the dimensions and grid of the liner as it expands, as shown in Figure 4.11. Although such an approach may seem obvious at first it poses some significant complications.

1. A large section of the liner must be modeled

It is expected to take around two minutes for the contact temperature to arrive at a steady state. All the

distance displaced by the cone in this time must be included in the grid of the liner. This in turn means a large number of grid cells are required to model the liner leading to slower calculations.

2. Continuous grid adjustment

Due to the plastic deformation of the liner (a part of) the grid of the liner must be adjusted every iteration, this is a time consuming process.

3. Grid alignment between the cone and the liner

When moving the cone at a certain speed with a given time step, the distance covered in one time step is not necessarily an exact multiple of the cell width. As a consequence some cells may be only partially in contact, this will introduce errors on the contact surface.

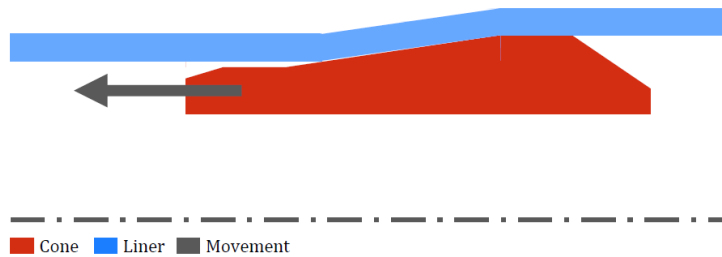


Figure 4.11: Movement of the cone in an absolute reference frame. A long section of the liner is modeled and the position of the cone is changed every iteration as a function of the expansion speed. Consequently the grid of the liner is adjusted to account for the plastic deformation.

4.5.2. Moving liner, relative reference frame

In this method, shown by Figure 4.12, the cone is taken as the reference point and the liner is modeled around it. Subsequently a "convective" heat transfer term is modeled inside the liner with the the expansion speed in the inverse direction. This method allows for a much smaller section of the liner to be modeled (about 7.5[cm] in front and 20[cm] behind the cone), as further described in Section 5.2.1. Additionally, no grid adjustments have to be made every iteration which saves a lot of computational effort. The only price to pay is the extra "convective" heat flux which is added to the cells in the liner. This option is selected for the model as it is the fastest to compute.

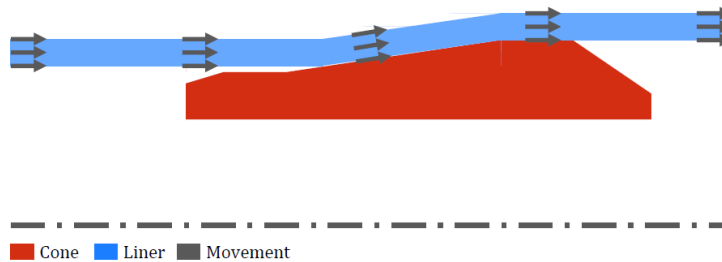


Figure 4.12: Movement of the cone using fluid properties inside the liner (relative reference frame). Only the section of the liner around the contact with the cone is modeled, a velocity component is added to the liner to simulate the relative movement of the two components.

4.6. Thermal gradients on a non-orthogonal grid

On an orthogonal grid, such as shown in Figure 4.4 the calculation of the gradient normal to and at the center of cell wall can be calculated using a simple finite difference. The north thermal gradient is for instance represented by

$$\left(\frac{\delta T}{\delta r}\right)_n = \frac{T_{j,i} - T_{j-1,i}}{|r_{j,i} - r_{j-1,i}|}, \quad (4.15)$$

where j represents the vertical cell index (r -direction) and i the horizontal cell index (z -direction). Depending on which gradient is desired the appropriate indices must be selected and inserted into Equation 4.15 which gives an example for the north gradient of cell j, i . Note that the positive directions of the gradients are defined according to Figure 4.13.

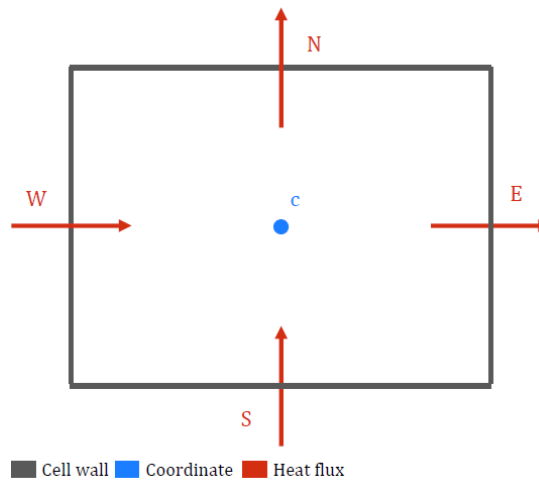


Figure 4.13: Postive direction of heat fluxes on a cell. A heatflux is defined positive when it is flowing into the cell at the South and West boundaries, or flowing out of the cell at the North and East boundaries.

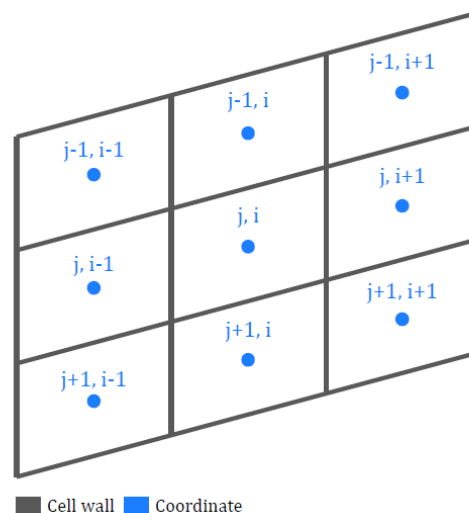


Figure 4.14: Naming convention of the neighboring cells on a non-orthogonal grid. The top left cell of the grid is seen as the origin and has coordinate (1,1), the index j increases downward and the index i increases further to the right.

A direct consequence of the skewed grid, such as shown in Figure 4.14, is that it is no longer trivial how the thermal gradient at and normal to the cell wall must be calculated. Many methods exist to determine the gradient at the cell wall for any arbitrary grid. A lot of them rely on calculating the gradients in the center of the cells (using for instance a central difference scheme) and then using regression analysis using by for example the least squares method to extrapolate the gradient to the cell wall [13]. These techniques are useful as they work on any 2D or 3D grid, but require a lot of computational power. The grid described in Section 4.2, is not unstructured merely non-orthogonal as the west and east cell boundaries are always parallel to the r -axis. This can be used to simplify the calculation of the thermal gradient at the wall. A procedure is developed to calculate the wall thermal gradient, in correspondence with Figures 4.15 to 4.17.

1. Find two points at which the temperature can be found by linear interpolation and which form a line normal to the wall, through its center ($I1$ and $I2$)
2. Interpolate to find the temperature at these points, following the orange lines in the Figures 4.15 to 4.17
3. Calculate the thermal gradient along a line intersecting the interpolation points and the center of the cell wall

4.6.1. West & East gradient

For the east and west flux this procedure is fairly straight forward as the gradient parallel to the z -axis is desired. The interpolation points $I1$ & $I2$ are located at the r -coordinate of the known center of the cell wall hence,

$$r_{I1} = r_{I2} = r_{we_{j,i}}. \quad (4.16)$$

Linear first order interpolation is then used to find the temperature at these points. For the situation shown in figure 4.15 the temperature at $I1$ is given by

$$T_{I1} = \frac{T_{j-1,i} |r_{I1} - r_{c_{j,i}}| + T_{j,i} |r_{I1} - r_{c_{j-1,i}}|}{|r_{c_{j,i}} - r_{c_{j-1,i}}|}, \quad (4.17)$$

and the temperature at $I2$ by

$$T_{I2} = \frac{T_{j,i+1} |r_{I2} - r_{c_{j+1,i+1}}| + T_{j+1,i+1} |r_{I2} - r_{c_{j,i+1}}|}{|r_{c_{j,i+1}} - r_{c_{j+1,i+1}}|}. \quad (4.18)$$

The Equations 4.17 and 4.18 correspond to the situation sketched in Figure 4.15.

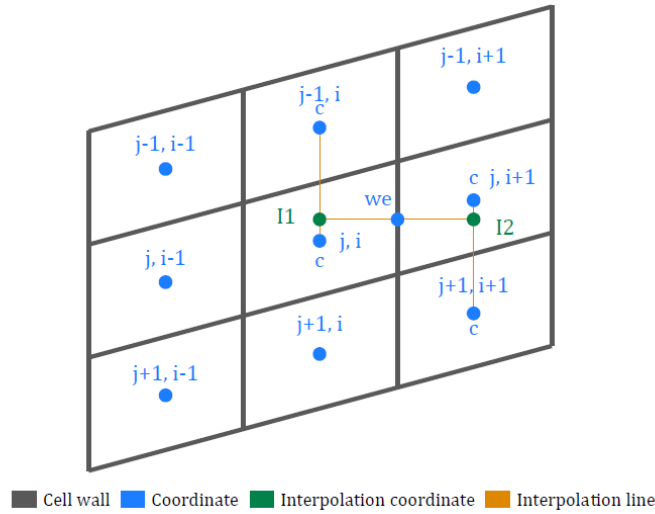


Figure 4.15: Lines and points used for the interpolation of the temperature at points $I1$ & $I2$ and the calculation of the thermal gradient on and normal to the east wall of the cell j, i

The z -coordinates of the points $I1$ & $I2$ are known, as they are in line with the cell centers above and below,

$$z_{I1} = z_{c_{j,i}}, \quad (4.19)$$

$$z_{I2} = z_{c_{j,i+1}}. \quad (4.20)$$

The thermal gradient is then calculated by taking a finite difference between the interpolation points

$$\left(\frac{\delta T}{\delta z} \right)_w = \frac{T_{I1} - T_{I2}}{|z_{I1} - z_{I2}|}. \quad (4.21)$$

At the top or bottom row of the grid, the situation can occur where a cell desired for interpolation is not available. The gradient between the cell (j, i) and the second interior cell $(j + 1, i)$ is then extrapolated to the point $I1$, as shown by figure 4.16. Therefore first the gradient with the second cell is calculated, which is then multiplied by the distance in the r -direction between the interpolation point and the cell center such that,

$$T_{I1} = \left(\frac{\delta T}{\delta r} \right)_{j+1,i} |r_{I1} - r_{c_{j,i}}|. \quad (4.22)$$

The temperature at $I2$ can still be interpolated and thus no extrapolation is required here and equation 4.18 is used. Interpolation is always preferred over extrapolation due to the higher accuracy.

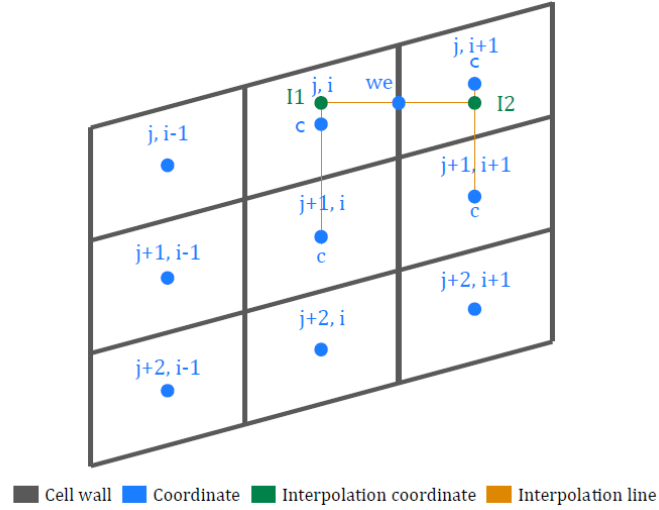


Figure 4.16: Lines and points used for the extrapolation of the temperature at point $I1$, interpolation at $I2$ and the calculation of the thermal gradient on the east wall of the cell (j, i) which is located at the top of the grid.

4.6.2. North & South gradient

The principle of interpolation is used in the same way for the north and south gradients as for the east wall. Now the gradient sought after is not parallel to any axis, nor are the coordinates of the point $I1$ & $I2$ in alignment with the centers of the neighboring cells. Therefore first an equation must be derived for the normal vector of the cell boundary. The slope of the normal with respect to the north cell wall is defined by

$$\left(\frac{dr}{dz} \right)_{norm.} = \frac{-1}{\frac{r_{1j,i} - r_{2j,i}}{z_{1j,i} - z_{2j,i}}}, \quad (4.23)$$

where 1 and 2 denote corners of the cells as specified by Figure 4.4. The normal vector found is the orange line between the points $I1$ and $I2$ in Figure 4.17.

Then slopes for the interpolation lines connecting the centers of the cells above and below the wall are derived as

$$\left(\frac{dr}{dz} \right)_{I1} = \frac{r_{c_{j,i}} - r_{c_{j,i-1}}}{z_{c_{j,i}} - z_{c_{j,i-1}}}, \quad (4.24)$$

$$\left(\frac{dr}{dz} \right)_{I2} = \frac{r_{c_{j+1,i+1}} - r_{c_{j+1,i}}}{z_{c_{j+1,i+1}} - z_{c_{j+1,i}}}. \quad (4.25)$$

The coordinates of $I1$ & $I2$ can be found by intersection of the connection lines and the normal vector on the cell wall which yields:

$$z_{I1} = \frac{r_{wn_{j,i}} - z_{wn_{j,i}} \left(\frac{dr}{dz} \right)_{norm.} - r_{c_{j,i}} + z_{c_{j,i}} \left(\frac{dr}{dz} \right)_{I1}}{\left(\frac{dr}{dz} \right)_{I1} - \left(\frac{dr}{dz} \right)_{norm.}}, \quad (4.26)$$

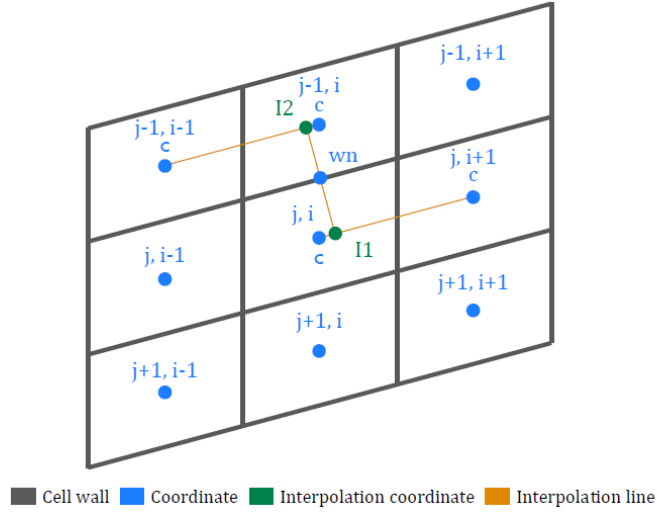


Figure 4.17: Lines and points used for the interpolation of the temperature at points $I1$ & $I2$ and the calculation of the thermal gradient on the north wall of the cell j, i . The skewed orange line through the north wall of the cell j, i , is exactly normal to this wall as determined by Equation 4.23.

$$r_{I1} = r_{c,j,i} + \left(\frac{dr}{dz} \right)_{I1} (z_{I1} - z_{c,j,i}), \quad (4.27)$$

$$z_{I2} = \frac{r_{wn,j,i} - z_{wn,j,i} \left(\frac{dr}{dz} \right)_{norm.} - r_{c,j-1,i-1} + z_{c,j-1,i-1} \left(\frac{dr}{dz} \right)_{I2}}{\left(\frac{dr}{dz} \right)_{I2} - \left(\frac{dr}{dz} \right)_{norm.}}, \quad (4.28)$$

$$r_{I2} = r_{c,j-1,i-1} + \left(\frac{dr}{dz} \right)_{I2} (z_{I2} - z_{c,j-1,i-1}). \quad (4.29)$$

For the interpolation step, the distances between the interpolation points and the cell centers are calculated using Pythagoras. For the point $I1$ these distances are given by

$$\Delta l_{left} = \sqrt{(z_{c,j,i-1} - z_{I1})^2 - (r_{c,j,i-1} - r_{I1})^2}, \quad (4.30)$$

$$\Delta l_{right} = \sqrt{(z_{c,j,i} - z_{I1})^2 - (r_{c,j,i} - r_{I1})^2}, \quad (4.31)$$

where the variable l denotes the distance. The temperature at $I1$ can then be calculated using linear interpolation

$$T_{I1} = \frac{T_{j,i} \Delta l_{left} + T_{j-1,i} \Delta l_{right}}{\Delta l_{left} + \Delta l_{right}}. \quad (4.32)$$

Finally, the interpolated temperatures and coordinates of the interpolation points are used to calculate the thermal gradient normal to and at the center of the wall so that

$$\left(\frac{\delta T}{\delta l} \right)_n = \frac{T_{I1} - T_{I2}}{\sqrt{(z_{I1} - z_{I2})^2 - (r_{I1} - r_{I2})^2}}. \quad (4.33)$$

By using other values for the indices j, i the fluxes of all other cells can be determined.

4.6.3. Verification of thermal gradient method

To verify the devised method to calculate the thermal gradients, a simple test case is used. In the case shown by Figure 4.18, a hollow cylinder is modeled with different fixed temperatures on the inner and outer surfaces and isolated boundary conditions on the sides. From analytical methods it is known that in this case the isotherms must remain aligned with the z -axis at any time. The grid is then fit to the geometry in a very strange way so as to bring the most possible disturbance to the result. Finally the result is analyzed and it can be concluded that the thermal gradient method is valid as indeed all the isotherms are parallel to the z -axis.

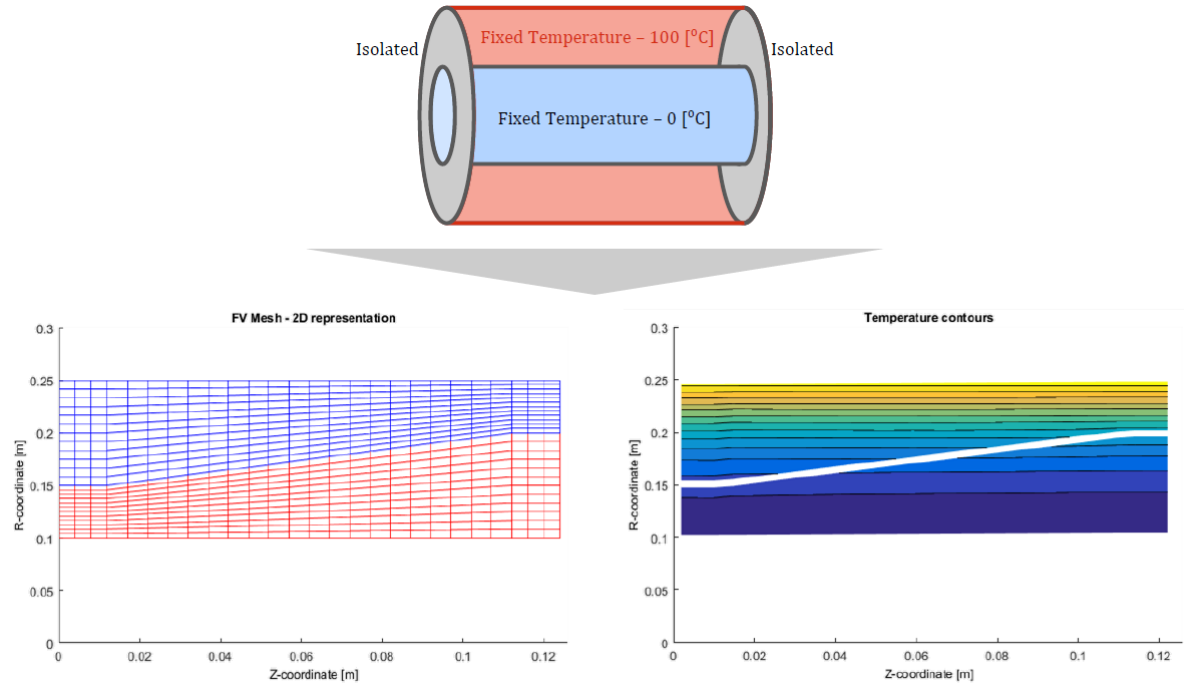


Figure 4.18: A test calculation, consisting of a hollow cylinder, is used to verify the interpolation method. The geometry and boundary conditions are shown in the top figure. In the bottom left, the mesh is shown which is deliberately fit to the geometry in a strange way. The bottom right figure, shows the contour lines of the temperature distribution.

5

Boundary Conditions

At the surfaces of the cone, liner, overlap and the interaction interfaces between them, conditions have to be specified to solve the heat transfer problem. Figure 5.1 gives a simplified overview of all the components in the system and indicates the heat fluxes. This chapter will describe the assumptions and modeling choices made for each boundary condition. Analysis of the boundaries is done by means of thermal resistance models which are described in Appendix E. The values for the material properties used in the thermal resistance models are taken from Appendix A at room temperature.

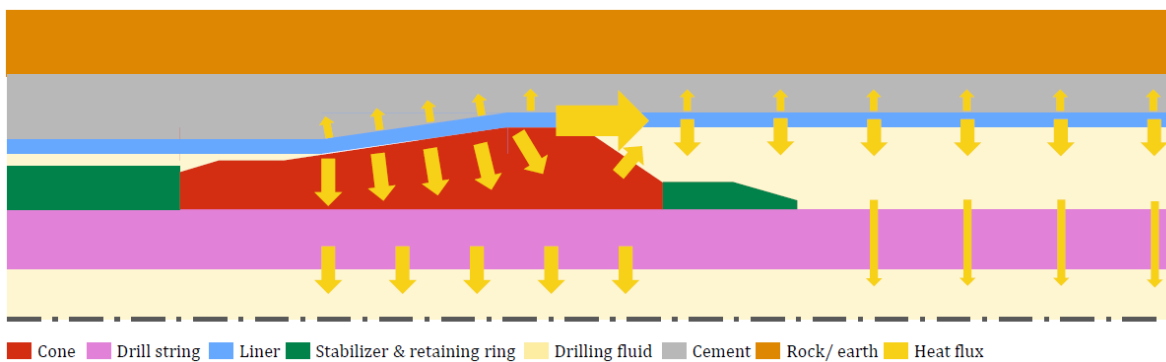


Figure 5.1: General overview of the cone and surrounding components during down hole expansion. The yellow arrows indicate qualitatively how the heat flows away from the sources into the surroundings.

The naming convention used for the boundary conditions is very similar to that of the grid cells, Figure 5.2 shows the name of each boundary condition.

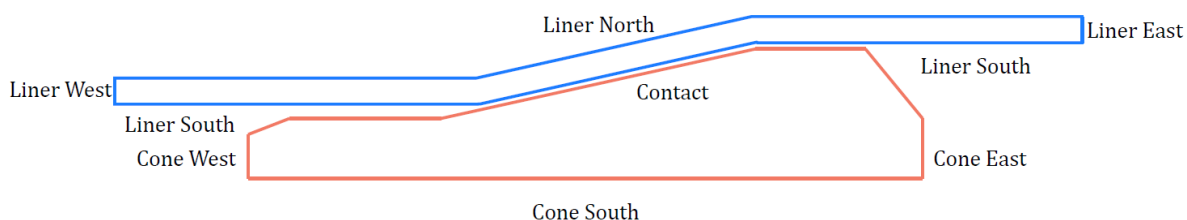


Figure 5.2: Naming convention of the boundary conditions using compass names with the exception of the contact surface.

First, the contact boundary condition will be described in Section 5.1.1. Section 5.2 then describes the liner boundary conditions. Finally, the boundary conditions of the cone are described in Section 5.3.

5.1. Contact boundary condition

At the contact surface between the cone and the liner heat is generated due to friction and subsequently this heat is divided between the cone and liner (heat partitioning). Additionally the layer of lubricant works as an insulator between the cone and the liner. Both these phenomena need to be modeled parallel to each other, the thermal resistance of the lubricant is analyzed in Section 5.1.1 and the frictional heat in Section 5.1.2.

5.1.1. Thermal resistance of the lubricant

There is a thin layer of lubricant, with an average thickness of approximately 90[μm], between the cone and liner, this layer poses an extra thermal resistance to the heat flow [7]. A thermal resistance model is used to see if this thin layer of lubricant has a significant influence on the temperature at locations close to the contact surface (around 1[mm]). The contact area on the north of the cone and south of the liner, are assumed to be the same as the thickness of the lubricant layer is only very small. The thermal resistances of the cone, liner and lubricant are then given by;

$$R_{co} = \frac{L_{co}}{k_{co}} \approx 6.85 * 10^{-5}, \quad (5.1)$$

$$R_{li} = \frac{L_{li}}{k_{li}} \approx 2,10 * 10^{-5}, \quad (5.2)$$

$$R_{lub} = \frac{L_{lub}}{k_{lub}} \approx 1.91 * 10^{-4}, \quad (5.3)$$

where R gives the thermal resistance per unit area, L is the thickness of the layer (1[mm] for the cone and liner, 90[μm] for the lubricant) and k is the thermal conductivity. As these resistances are in series and around the same order of magnitude the conclusion is that the thermal resistance of the lubricant must be considered. Note that when analyzing the temperature further away from the contact surface the thermal resistance of the lubricant becomes smaller in comparison to the other resistances. The impact of the lubricant resistance on the overall temperature profile is therefore expected to be minimal.

5.1.2. Heat generation due to friction

The straightforward approach to model the lubricant, would be to use 1 layer of cells with the thickness of the lubricant layer as the cell height. This method would imply using many more cells in the cone and liner, due to the limited growth of cells to ensure numerical stability. Therefore, the choice is made to model the lubricant layer merely as a thermal resistance between the cone and the liner. Inherently, this means that the assumption is made that no heat flows through the lubricant in the z -direction and that the thermal capacity of the lubricant is negligible. These assumptions are valid due to the very limited height of the lubricant layer, which implies that there is practically no area for heat transfer to take place in the z -direction and that the volume and hence (thermal) mass of the lubricant is limited. The heat fluxes from the cone to the liner and through the lubricant are then given by;

$$q_{co} = \frac{T_{co} - T_{co,n}}{\Delta l_{co}} k_{co}, \quad (5.4)$$

$$q_{co} = \frac{T_{co,n} - T_{lub}}{0.5\Delta l_{lub}} k_{lub}, \quad (5.5)$$

$$q_{li} = \frac{T_{li,s} - T_{li}}{\Delta l_{li}} k_{li}, \quad (5.6)$$

$$q_{li} = \frac{T_{lub} - T_{li,s}}{0.5\Delta l_{lub}} k_{lub}, \quad (5.7)$$

where Δl_{co} represents the distance from the center to the north surface of the top cell of the cone, Δl_{lub} the thickness of the lubricant layer and Δl_{li} the distance from the south wall to the cell center of the bottom most cell of the liner. The location of the temperatures, T_{co} , $T_{co,n}$, T_{lub} , $T_{li,s}$ and T_{li} is illustrated in Figure 5.3.

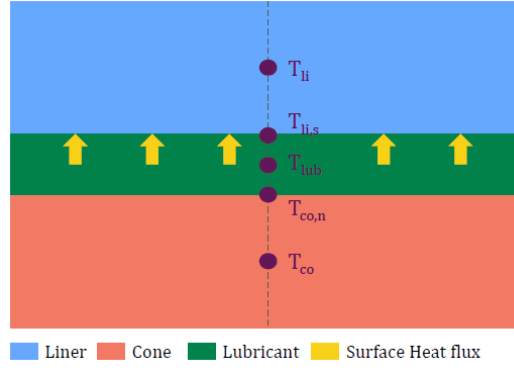


Figure 5.3: Schematic of the components and temperature points used to model the contact boundary condition. Only the cone, T_{co} , and liner, T_{li} , temperature are known but due to the 1D modeling of the heat transfer in the lubricant the system can still be solved.

The heat generated due to friction is derived in Section 3.1. This heat is created at the contact surface and not inside the bulk material of either the cone or the liner. Normally, the heat flux from the north of the cone would be equal to the heat flux at the south of the liner. In this case however, the heat flux from friction is introduced and defined positive in the north direction. The heat equilibrium at the surface is described by

$$q_{li} = q_{co} + q_{fr}, \quad (5.8)$$

where q_{fr} is the heat generated by friction per unit area. Equations 5.4 to 5.7 are then inserted in Equation 5.8 and after some rearranging an explicit equation for the lubricant temperature is found;

$$T_{lub} = \frac{\frac{k_{co} T_{co}}{\left(1 - \frac{k_{co} 0.5 \Delta l_{lub}}{k_{lub}}\right) \Delta l_{co}} + \frac{k_{li} T_{li}}{\left(1 + \frac{k_{li} 0.5 \Delta l_{lub}}{k_{lub}}\right) \Delta l_{li}} + q_{fr}}{\frac{k_{co}}{\left(1 - \frac{k_{co} 0.5 \Delta l_{lub}}{k_{lub}}\right) \Delta l_{co}} + \frac{k_{li}}{\left(1 + \frac{k_{li} 0.5 \Delta l_{lub}}{k_{lub}}\right) \Delta l_{li}}}. \quad (5.9)$$

This temperature is used to derive the wall temperatures of the cone and liner. After the lubricant temperature is calculated the heat fluxes can be calculated according to the normal procedure.

5.2. Liner Boundary conditions

With the contact boundary described in the previous section, the remaining four boundary conditions of the liner are explained below. During overlap expansion, the boundary conditions of the overlap liner are identical to that of the single liner except for their interface boundary, where perfect contact and thus normal conduction of heat is assumed.

5.2.1. East & West

The east and west boundaries of the liner are theoretical boundaries which don't exist in reality. They originate from the fact that the choice is made to model only a section of the liner, moving relative to the cone. To ensure the modeling method described in Section 4.5 is valid, these boundary conditions must be chosen so that they have minimal influence on the final solution. The movement of the liner is modeled through a "convective" heat transfer term inside the liner, hence the boundary conditions on the east and the west side of the liner are split into a conductive and a convective part.

Convective term

In order to model the convective term at the boundaries an imaginary grid cell is used just outside the computational domain. The temperature of this cell is assumed to be equal to the down hole or well temperature. Furthermore it has the same dimensions as the adjacent grid cell within the computational domain. With this imaginary cell, the convective heat flux at the boundaries is calculated parallel to the internal convective heat flux;

$$q_{conv} = \frac{v}{\Delta l} \rho V C_p T_{do}, \quad (5.10)$$

where, T_{do} is the ambient or down hole temperature, Δl the length of the cell in the direction of the velocity, and A is the area normal to the direction of the velocity, v . The use of such an imaginary cell is valid as long as the conductive terms at the boundaries are negligible compared to the convective terms. To verify this assumption, the model is run with different lengths of the liner to show that it does not influence the final result, this is shown by Figure 5.4.

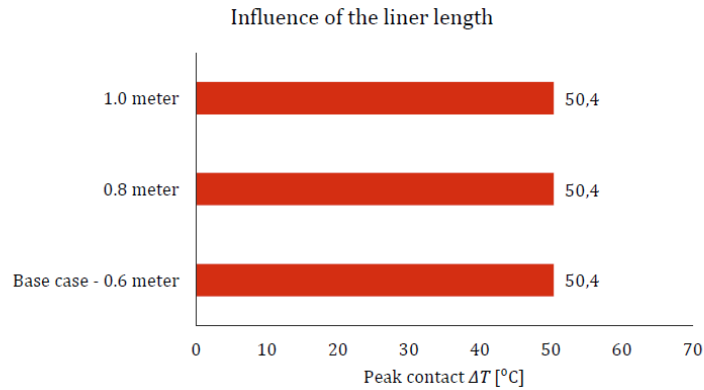


Figure 5.4: Comparison between several runs of the base case model with different lengths lengths of the liner modeled. It can be seen that the peak contact temperature is unaffected by the length of the liner segment modeled.

Conduction

As shown in Figure 5.4, the length of the liner in the model has been chosen such that conductive terms play a negligible role at the east and west boundary of the liner. Therefore the simplest boundary condition can be opposed, isolated.

5.2.2. South, in front of the cone

A region filled with drilling fluid exists below the liner and in front of the cone, as can be seen in Figure 5.1. This region is fairly small as the liner is still in the unexpanded state. Furthermore the fluid moves with the movement of the cone. This means that the fluid here will heat up, which will effect the rate of heat transfer on this boundary. Since the thermal gradients and heat transfer coefficients in this region are expected to be low and their is no room for the heat to dissipate this boundary is treated as an isolated boundary. This assumption is validated by comparing peak temperature increase of the isolated boundary condition with a fixed ambient temperature boundary condition as shown in Figure 5.5.

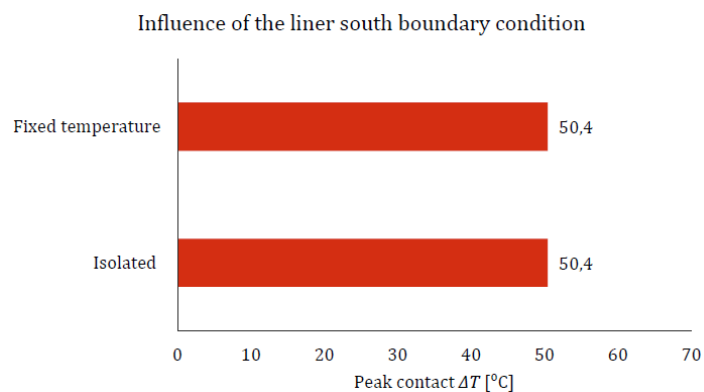


Figure 5.5: Comparison of the lubricant peak temperature for different boundary conditions at the south of the liner. It can be seen that the boundary condition has no effect on the peak contact temperature.

From Figure 5.5, it is evident that the choice for an isolated boundary condition does not influence the peak contact temperature.

5.2.3. South, to the rear of the cone

The region of drilling fluid behind the cone is fairly comparable to that in front of the cone. The major difference is the volume of the region and the fact that more heat can dissipate at the rear of the cone. As a preliminary analysis, the thermal resistance of the heat flowing with the liner is compared to the convective resistance of the drilling fluid;

$$R_{df} = \frac{1}{A_{li} h_{df}} \approx 0.0129, \quad (5.11)$$

$$R_{li} = \frac{1}{A_{li} v \rho C_p} \approx 0.00034. \quad (5.12)$$

In which the area A_{li} is linked to the expansion speed so its length is the same per unit time as that of the heat traveling inside the liner has covered;

$$A_{li} = 2\pi r_{li} v. \quad (5.13)$$

As these resistances are in parallel and $R_{df} \gg R_{li}$ the resistance of the drilling fluid can be neglected, hence assuming an isolated boundary condition on the south wall of the liner to the rear of the cone.

5.2.4. North

The north wall of the liner is in contact with a layer of curing cement. Heat generation from this cement was proven negligible in Section 3.3. Furthermore, heat generated by friction and plastic deformation is conducted through the liner in the direction of the north boundary as shown by Figure 5.6.

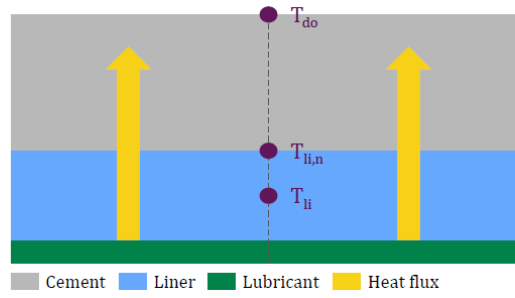


Figure 5.6: Layout of components and temperatures taken into account when modeling the liner north boundary condition. Due to the low thermal conductivity of the cement an isolated boundary condition is used.

To determine what type of boundary condition is suitable a thermal resistance model is used. First the thermal resistance of the liner is analyzed;

$$R_{li} = \frac{L_{li}}{k_{li}} \approx 2.31 * 10^{-4}, \quad (5.14)$$

taking the full thickness of the liner (11[mm]) as L_{li} , this corresponds with distance from the frictional heat source to the wall. Next the thermal resistance of the cement layer is computed using;

$$R_{ce} = \frac{L_{ce}}{k_{ce}} \approx 2.5 * 10^{-2}, \quad (5.15)$$

where L_{ce} is the expected average thickness of for the cement layer, 50[mm]. Furthermore, the thermal conductivity of cement is estimated as $k = 2[\frac{W}{mk}]$, which is a relatively high value for cement [22]. Despite the high value for the thermal conductivity of the cement, the thermal resistance of the cement layer is still a factor of 100 larger than the thermal resistance of the liner. Furthermore, the formation behind the layer of cement will also have a thermal conductivity in the same order of the value of cement. Therefore the north boundary of the liner is treated as an isolated boundary condition. To validate this assumption, the heat flux that would of have been conducted through the north boundary is estimated;

$$Q_{li,n} = k_{ce} \frac{T_{li,n} - T_{do}}{\Delta l_{ce}} A_{li,n}, \quad (5.16)$$

where $A_{li,n}$ is the full outside area of the liner and $T_{li,n}$ is the average temperature at the north of the liner. This theoretical heat flux is 119 [W] or 0.2% of the total heat input, this can be neglected.

5.3. Cone boundary conditions

Since the cone is stationary with respect to the chosen reference frame, the boundary conditions are slightly less complicated than those of the liner. Nevertheless, the convective heat transfer coefficients associated with the drilling fluid pose some complications. Evidently the North boundary condition of the cone is the contact boundary condition, which is described in Section 5.1.

5.3.1. South

At the south of the cone two thermal resistances exist in series, first a conductive resistance through the drill string and second a convective resistance to the drilling fluid as shown in Figure 5.7.

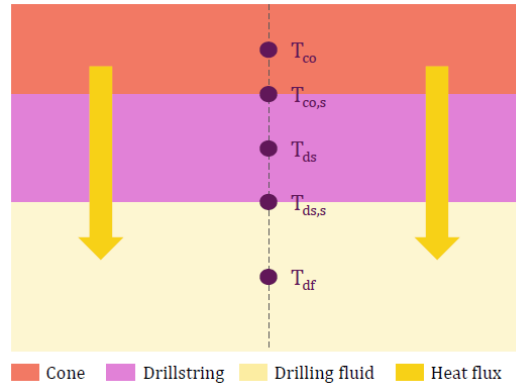


Figure 5.7: Schematic of the components and temperatures at the south of the cone. At the south of the cone both the drill string and the drilling fluid pose as thermal resistances, both need to be taken into account for adequate modeling.

The thermal resistances of both the drill string (approximate thickness of 54[mm], L_{ds}) and the drilling fluid are computed and compared to the thermal resistance of the cone (average thickness of 30[mm], L_{co}) in order to investigate if any of the resistances can be neglected in the model. These resistances are given by;

$$R_{co} = \frac{L_{co}}{k_{co}} \approx 2.05 * 10^{-3}, \quad (5.17)$$

$$R_{ds} = \frac{L_{ds}}{k_{li}} \approx 1.28 * 10^{-3}, \quad (5.18)$$

$$R_{df} = \frac{1}{h_{df}} \approx 1.05 * 10^{-3}, \quad (5.19)$$

here h_{df} is the convective heat transfer coefficient with the drilling fluid. Unfortunately all thermal resistances are in the same order of magnitude, so that all of them need to be taken into account. The choice is made to model the drill string as a thermal resistance on the boundary as the computational domain would otherwise have to be expanded significantly. This assumption implies that heat only flows through the drill string in the radial direction essentially converting this into a 1D section. The heat fluxes through the south of the cone, the drill string and subsequently into the drilling fluid are then described by;

$$q_{co} = \frac{T_{co} - T_{co,ws}}{\Delta r_{co}} k_{co}, \quad (5.20)$$

$$q_{ds} = \frac{T_{co,ws} - T_{ds,ws}}{\Delta r_{ds}} k_{ds}, \quad (5.21)$$

$$q_{df} = h_{df} (T_{ds,ws} - T_{df}), \quad (5.22)$$

$$q_{co} = q_{ds} = q_{df}. \quad (5.23)$$

As the heat flux through the drill string is assumed as 1D, the heat fluxes must all be equal and the equations can be combined to form one equation for the heat flux on the south of the cone

$$q = \frac{T_{co} - T_{df}}{\frac{\Delta r_{co}}{k_{co}} + \frac{\Delta r_{ds}}{k_{ds}} + \frac{1}{h_{df}}}. \quad (5.24)$$

The only term remaining to be determined is the convective heat transfer coefficient of the drilling fluid h_{df} . Determining this heat transfer coefficient is complicated due to the non-Newtonian properties of the fluid. In order to get a good estimate of this heat transfer coefficient, two calculation methods are used. First a Newtonian approach, using an apparent viscosity, thereafter an approximate non-Newtonian approach.

Newtonian

Utilizing the method described in by Mills in chapter 4 of his book the Newtonian heat transfer coefficient is calculated [1]. First the speed of the drilling fluid inside the drill string must be calculated. Here the fact is used that the volume displaced by the cone during expansion must be filled with drilling fluid. The velocity of the drilling fluid is given by;

$$v_{df} = v_{ex} \frac{A_{ds,in}}{A_{li,in}}. \quad (5.25)$$

where $A_{ds,in}$ is the inner area of the drill string, $A_{li,in}$ the inner area of the expanded liner, v_{ex} the expansion speed and v_{df} the speed of the drilling fluid to the rear of the cone. Once the speed of the fluid is known the Reynolds number,

$$Re = \frac{\rho v D_h}{\mu}, \quad (5.26)$$

can be computed based on the density of the drilling fluid ($\rho_{df} = 1557[\frac{\text{kg}}{\text{m}^3}]$) and the apparent viscosity of the drilling fluid ($\mu_{df} = 0.024[\text{Pas}]$). For the base case a Reynolds number of $Re = 6274[-]$ is found, which means the flow inside the drill string is in the transition region from laminar to turbulent flow. In order to calculate the Nusselt number, first the Prandtl number and friction factor need to be calculated;

$$Pr = \frac{\mu C_p}{k}, \quad (5.27)$$

$$f = (0.79 * \ln(Re) - 1.62)^{-2} \quad (5.28)$$

The Nusselt number is approximated using Gnielinski's correlation:

$$Nu = \frac{\left(\frac{f}{8}\right)(Re - 1000)Pr}{1 + 12.7\left(\frac{f}{8}\right)^{1/2}(Pr^{2/3} - 1)}, \quad (5.29)$$

as the Reynolds and Prandtl numbers are within its range of validity;

$$3000 \leq Re \leq 5 * 10^6, \quad (5.30)$$

$$0.5 \leq Pr \leq 2000. \quad (5.31)$$

For the base case the Nusselt number is 193[-], which can be converted into a heat transfer coefficient using;

$$Nu = \frac{h D_h}{k}. \quad (5.32)$$

The Newtonian fluid approach yields a convective heat transfer coefficient of $h_{df} = 833[\frac{\text{W}}{\text{m}^2\text{K}}]$.

Non-Newtonian

Calculating the convective heat transfer coefficient for non-Newtonian fluids, comes with a significantly higher degree of uncertainty as compared to Newtonian flows. First of all the calculation of the Reynolds numbers is difficult as the viscosity is dependent on the local shear rate. Three different approaches for the calculation of the Reynolds number are provided by Pinho [25]. The first is the generalized Reynolds number, which is calculated so that the Fanning friction factors for non-Newtonian and Newtonian fluids in laminar pipe flow fit onto the same curve of $f_f = \frac{16}{Re'}$. The generalized Reynolds number is given by:

$$Re' = \frac{\rho \bar{v} D}{\eta'}, \quad (5.33)$$

where \bar{v} is the bulk velocity of the fluid, D the hydraulic diameter and η' an apparent viscosity defined by:

$$\eta' = K' \left(\frac{8\bar{v}}{D} \right)^{n-1}, \quad (5.34)$$

where n is the power-law fluid exponent and K' the corrected consistency of the fluid;

$$K' = K \left(\frac{3n+1}{4n} \right)^n, \quad (5.35)$$

which depends again on the power-law exponent, n , and the consistency, K . This approach yields a Reynolds number of $Re' = 6544[-]$. Another proposed approach is the Re^+ approach, which is based on the definition of a characteristic shear rate of $\frac{\bar{v}}{D}$. This approach is given by;

$$Re^+ = \frac{\rho \bar{v} D}{\eta^+}, \quad (5.36)$$

$$\eta^+ = K \left(\frac{8\bar{v}}{D} \right)^{n-1}. \quad (5.37)$$

Using the Re^+ approach a Reynolds number of $Re^+ = 1752[-]$ is found. The final approach given is the apparent Reynolds number, based on the apparent viscosity of the fluid. This approach is specifically used for pipe flows and is given by;

$$Re^a = \frac{\rho \bar{v} D}{\eta^a}, \quad (5.38)$$

$$\eta^a = K \left(\frac{3n+1}{4n} \frac{8\bar{v}}{D} \right)^{n-1}. \quad (5.39)$$

The apparent Reynolds number is $Re^a = 10362[-]$, which is in fair agreement with the generalized Reynolds approach. The difference with the Re^+ approach can most likely be explained due to the fact that this approach is intended for external flows, whereas the flow inside the drill string is a internal (pipe) flow (where the Re' and Re^a are more suitable). Assuming that Re' and Re^a are the best options the conclusion is made that the flow is turbulent and due to the length of the drill string also fully developed. Pinho also provides an equation for the Nusselt number for hydro-dynamically fully developed turbulent flows of power law fluids through the Stanton number:

$$St^a = 0.0152 Re_a^{-0.155} Pr_a^{-\frac{2}{3}}, \quad (5.40)$$

$$St^a = \frac{Nu}{Re^a Pr^a}. \quad (5.41)$$

These equations are valid in the ranges of:

$$3000 \leq Re^a \leq 90000, \quad (5.42)$$

$$0.2 \leq n \leq 0.9. \quad (5.43)$$

Using these equations a Nusselt number of $Nu = 221[-]$ is found, yielding a convective heat transfer coefficient for the drilling fluid of $h_{df} = 954 \left[\frac{W}{m^2K} \right]$.

Convective heat transfer coefficient

As both methods yield a result in the same order of magnitude and sensitivity analysis (Section 7.3) shows that this parameter does not have a big influence on the contact temperature, h_{df} is set to the Non-Newtonian value of $954[\frac{W}{m^2K}]$.

5.3.2. West

The west side of the cone is difficult to properly fit into one boundary condition. First of all there is the near cone stabilizer, which ensures the cone is concentric with respect to the liner before it makes contact. Furthermore, a small region of drilling fluid exists, which is stationary with respect to the cone. As the major part of the heat inside the cone and the liner flows in the east direction and the heat sources are located further to the east of this boundary, this section of the cone does not heat up as much as the rest of the cone. The boundary condition chosen here will most likely have very limited effect on the overall solution, this can be proven by comparing the isolated and fixed ambient temperature boundary conditions as shown in Figure 5.8

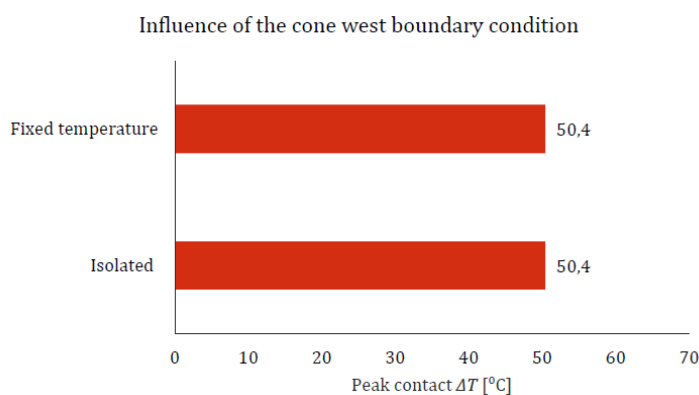


Figure 5.8: Comparison of the lubricant peak temperature for different boundary conditions at the west of the cone

So, although in reality some heat may be transferred into the drilling fluid, this heat flux is expected to be minimal. An isolated boundary condition is used as it is the conservative option.

5.3.3. East

To the east of the cone a region of drilling fluid exist which is moving with the cone. This means that although it does have a bulk velocity of roughly the expansion speed it is stationary with respect to the cone. The hydraulic diameter of this region is calculated by;

$$D_h = \frac{4A}{P}, \quad (5.44)$$

in which P denotes the wetted perimeter and A the cross-sectional area of the flow. The bulk velocity of the drilling fluid in this region is assumed to be equal to the expansion speed. Then following the procedure described in Section 5.3.1 the Newtonian and non-Newtonian Reynolds numbers are calculated and found between $20 \leq Re \leq 474$, indicating the fluid is in a laminar flow regime. The heat transfer coefficient is then driven by the natural circulation of the drilling fluid in this region. To investigate the impact of this boundary condition a simulation is run using an isolated boundary condition and a fixed ambient temperature boundary condition, the results are shown in Figure 5.9.

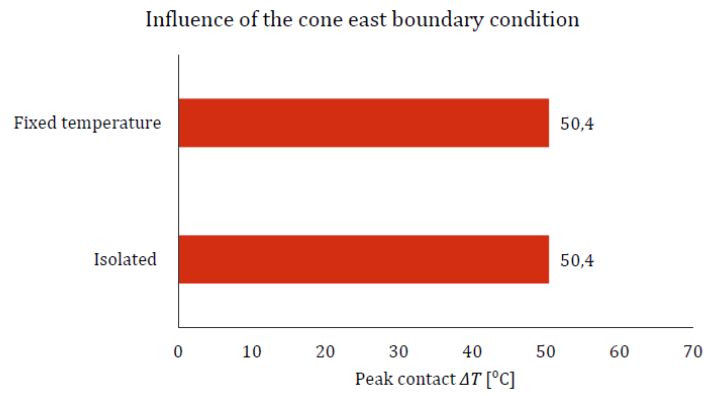


Figure 5.9: Comparison of the lubricant peak temperature for different boundary conditions at the east of the cone

It is found that the boundary condition has no impact on the peak temperature. To prevent adding unnecessary complications to the model and remain on the safe side, an isolated boundary condition is used at the east of the cone.

6

Experiments

In order to verify the model, two full scale expansion test are conducted in the laboratory at Shell Rijswijk. This laboratory is home to the custom built RETF (Rotary Expandable Test Facility), shown in Figure 6.1. The RETF is basically a horizontal tension machine with a maximum pulling capacity of 250 metric tonnes, which can expand samples up to 9 meters in length.



Figure 6.1: RETF (Rotary Expandable Test Facility) in the Shell laboratory in Rijswijk with 9 5/8" liner installed for the split cone test.

The first test consists of a set of thermocouples that were added in the setup of an already planned test. This first test focuses on the verification of the expansion force and the load distribution on the cone. the second test has been specifically designed to verify the thermal model of the expansion process.

6.1. Test 1: Split cone

The split cone test was originally designed to give more insight in the pressure profile on the cone by measuring the forces on 3 sections of the cone through strain gages. A few thermocouples have been added inside this cone and on the outside of the liner, this required only minor modifications which could still be implemented in the design.

6.1.1. Goals

The goal of the split cone test is to obtain basic insight in the thermal behavior of the system. Two specific aspects are of interest:

1. Verify the assumption of axis symmetry
2. Verify the total heat production

6.1.2. Setup

As this test was designed for other purposes, only limited changes could be made to monitor temperatures. A total of 14 thermocouples are added to this test. All thermocouples are of type K with a diameter of 1.5[mm] and are sampled at 1[Hz]. Detailed technical drawings of the cone and the liner for the split cone test are available in Appendix F, these drawings also clearly show how the cone is split.

Cone

8 Thermocouples are placed inside the cone at 3 different locations in the z -direction, 2[mm] below the contact surface, as shown in Figure 6.2. At the front location (1), where the front pressure peak is expected, 4 thermocouples have been placed with an angle of 90° between them. At the two rear locations (2,3), close to the expected rear pressure peak, there was insufficient room to fit all 4 thermocouples so that only 2 could be placed at each location with a 180° angle between them.

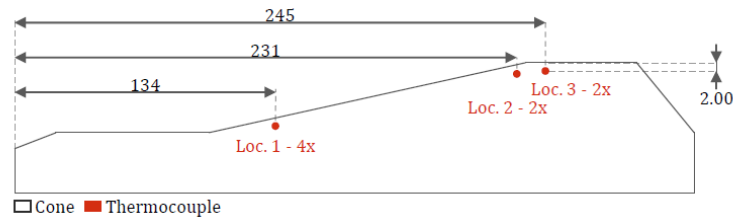


Figure 6.2: Placement of thermocouples in the split cone at 3 different locations. The first location is below the expected front pressure peak, the second, below the rear pressure peak. Finally, location 3 should be effected significantly more by the overlap expansion as compared to the single expansion. All dimensions are in [mm].

Liner

On the outside of the liner a total of 6 thermocouples have been placed, 3 of them at the single liner section and 3 of them at the overlap section. The thermocouples are placed 800[mm] from the start of each liner segment and 300[mm] apart from each other.



Figure 6.3: Placement of thermocouples on the outside of the single liner section for the split cone test. The thermocouples are welded to the liner at locations 1, 2 and 3 as marked on the liner. Before welding the surface is first cleaned to ensure good contact.

6.1.3. Results

A difference of around $2 - 5[^\circ\text{C}]$ is visible between the thermocouples at locations 2 and 3, as defined in Figure 6.2, this shows that such a thermal gradient can exist inside the material. The thermocouples at the same z -location but at different circumferential orientations show the same temperatures. Combining these two observations leads to the conclusion that the heat input must be axis symmetric otherwise a difference between the thermocouple outputs at different circumferential locations should be visible.

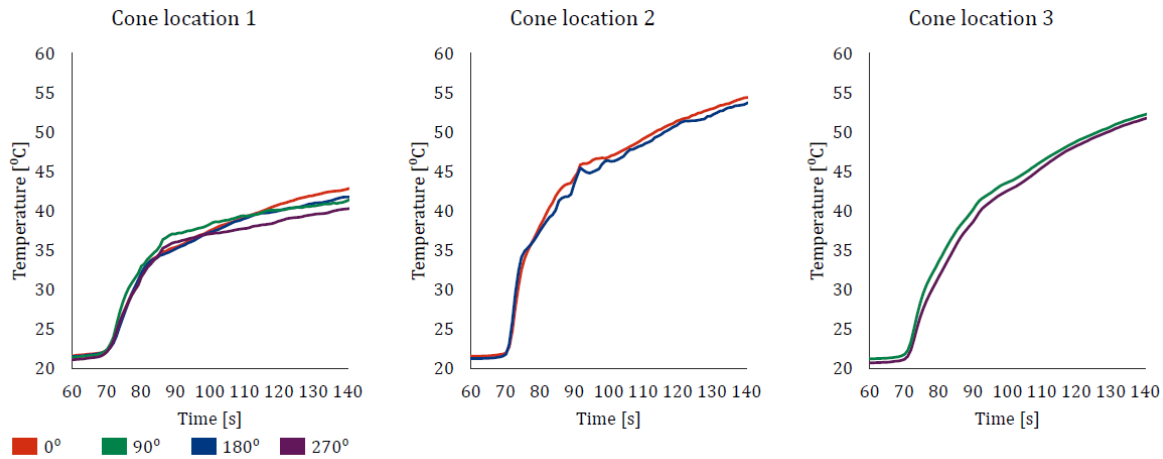


Figure 6.4: Cone temperatures over time during the single liner expansion of the split cone test, grouped per location. It is clear that thermocouples at the same z -location give the same result, hence axis symmetry is valid.

Next the liner thermocouples are analyzed of which the output is shown in Figure 6.5. It was expected that all liner thermocouples would show the same heating curve, the third thermocouple however gave a different result, this difference is yet unexplained. To be sure 5 thermocouples will be placed on the liner during the thermal test to rule out this uncertainty. In any case the model gave a significant over prediction of the liner temperature by about 5–10[°C]. After analysis of several possible causes, this has led to the implementation of the strain dependent modeling of the Taylor-Quinney coefficient by means of the Zehnder model as described in Section 3.2. The Zehnder model gives a significantly lower average value for the Taylor-Quinney coefficient as compared to typical literature values, the lower heat input then leads to a lower temperature of the liner after expansion.

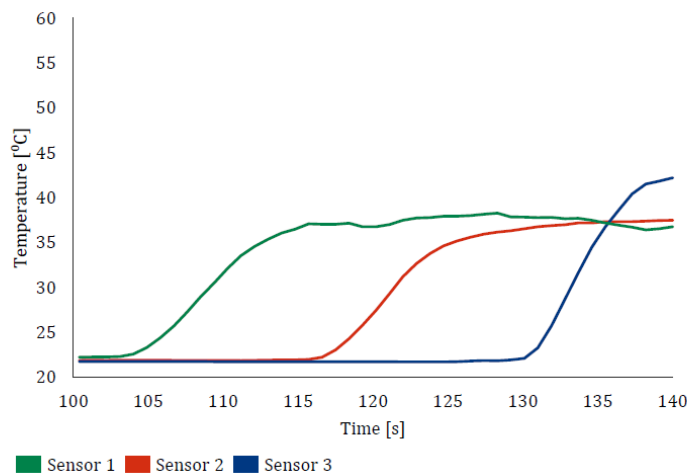


Figure 6.5: Temperature of the liner at three different locations during single liner expansion of the split cone test. As soon as the cone passes the thermocouple the temperature increases and then remains steady.

Visual inspection of the cone after the expansion test, as shown in Figure 6.6, showed that the front cut which was made to split the sections had filled itself with RPSLF during the test. This most likely prevented a lubricant film from building up over the full length of the contact area. In turn the lack of the presence of the film could lead to a higher average friction coefficient and thus explain the roughly 12% higher expansion force during the split cone test as compared to a regular cone. The expansion force of the split cone test is shown in Figure 6.7, with a regular cone the steady state expansion force is expected in the order of 950[kN].



Figure 6.6: Left, the split cone after the test. It can be seen how the lubricant film is broken at the cuts of the split segments. On the right, the top segment has been removed to show that the gap has filled up with lubricant during the expansion.

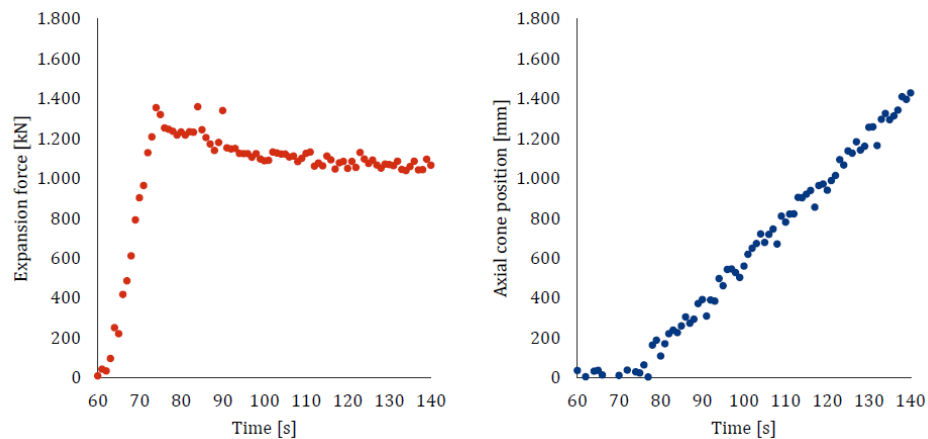


Figure 6.7: Left, the expansion force over the time during the split cone test. As expected, the expansion force decreases slightly over time as the lubricant heats up. On the right, the position of the cone follows a linear curve indicating a constant expansion speed.

6.1.4. Lessons learned

Some practical lessons were learned during the split cone test which led to improvements of the setup for the thermal test.

- **Liner Insulation**

During the split cone test, the outside of the liner was not insulated. Although heat losses due to convection and radiation are expected to be minimal and the (short-term) stability of the temperature of the sensors on the liner supports this, for future tests it would be wise to rule out any uncertainties by insulating the liner.

- **Sampling rate of sensors**

The plan was to sample all thermocouples at 10[hz] however malfunctioning of the data acquisition hardware prevented this. For future test this problem should be solved.

- **Running speed**

The split cone test was run at an expansion speed of 20[mm/s] due to requirements of the original plan for the test. Running at higher speeds gives a bigger difference between heating due to plastic deformation and friction, therefore future test could be run at higher speeds, the maximum expansion speed of the RETF is 30[mm/s].

- **Time to reach steady state**

The results from the thermocouples inside the cone indicate that, a full steady state was not yet achieved after 70[s] of single liner expansion. It is likely that the reduced mass of the split cone, where roughly 1/3 of the mass was removed to make room for the strain gages, also influenced the steady state behavior. To rule out any doubt in the future a longer section of liner should be expanded and a cone with the nominal mass should be used.

6.2. Test 2: Thermal test

The thermal test has been specifically designed to verify the thermal model of the expansion process and builds on the results and lessons learned from the split cone test. Detailed technical drawings of the design of the cone and liner for this test are available in Appendix G. All raw results from the thermal cone test are shown in Appendix H.

6.2.1. Goals

The thermal test is equipped with a lot more thermocouples than the split cone and should therefore be able to not only give insight in the total heat input but also the distribution of the heat input which is in turn an indication for the pressure profile. The thermal test has three main goals:

1. Decouple the heating due to plastic deformation and heating due to friction
2. Verify the pressure profile
3. Verify the thermal model

6.2.2. Background principle

The main philosophy behind the thermal test is that the temperature profile along the length of the cone is closely linked to the pressure profile. When measuring the temperature very close to the surface not only the temperature increase due to local frictional heating is measured but also heating from plastic deformation and heat which has been built up in the surrounding area. In a way the temperature at the contact surface could be seen as a superposition of the effect of heat from friction and plastic deformation as sketched in Figure 6.8. The strong local correlation of the temperature with the pressure profile can be used to reverse engineer the pressure profile from the temperature readings.

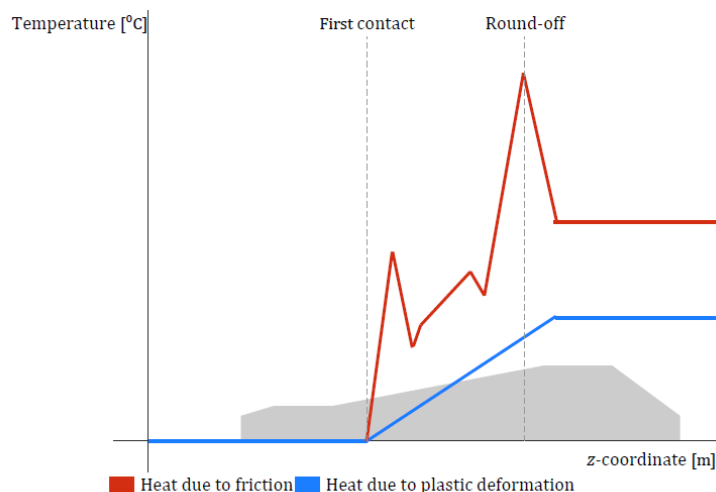


Figure 6.8: Principle of the thermal test; The temperature at the contact surface is a superposition of heat generated by plastic deformation (blue) and heat generated by friction (red).

6.2.3. Setup

For a detailed analysis of the pressure profile, it is necessary to have enough thermocouples inside the cone to capture all pressure peaks. Previous research by Willmink and 4RealSim indicates that the expected width of the shallowest pressure peak is about 15[mm] [35]. To ensure this peak will be measured with some extend

of detail the distance between the thermocouples is chosen to be 6.0[mm]. To ensure the full pressure profile is measured the measurement section is chosen slightly longer than the expected pressure profile. The thermocouples are numbered from front to rear, from 1 to 30.

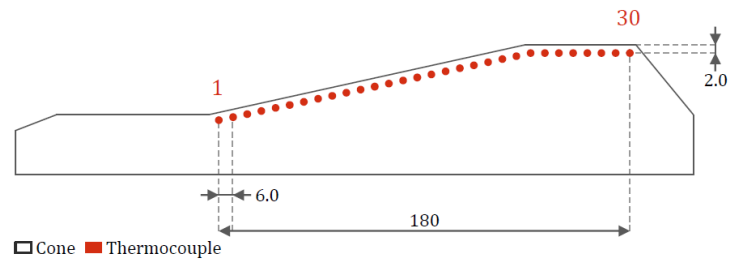


Figure 6.9: Placement of thermocouples inside the cone for the thermal test. The thermocouples are placed over a length of 180[mm] with 6[mm] spacing between them and 2[mm] below the contact surface.

In order to fit such a larger number of thermocouples inside a single cone a spiral pattern is used, an angle of 36° is set between each thermocouple so that the maximal spacing is created between the thermocouples hence minimal distortion of the measurement. The holes for the placement of the thermocouples are manufactured by electrical discharge machining from the inside of the cone. This is done to ensure the contact surface with the liner remains unaffected, ruling out any new tribological effects. In Figure 6.10 the inside of the cone is shown with the holes for the thermocouples highlighted in red.

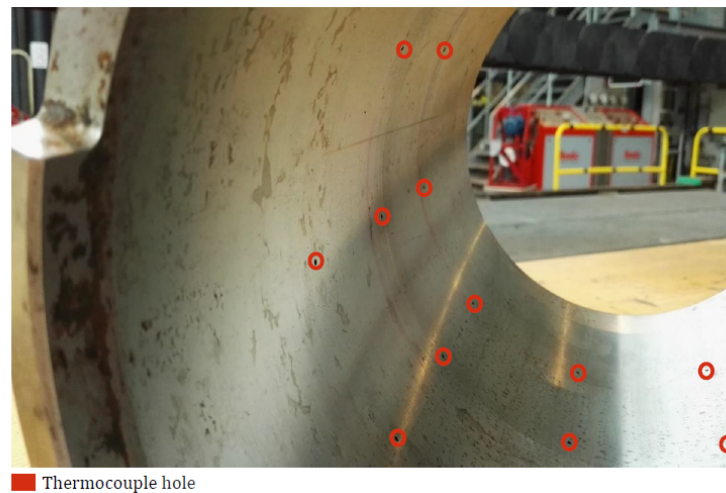


Figure 6.10: Cone with holes in spiral pattern for placement of thermocouples for the thermal cone test. The spiral pattern is used so that the sensors are placed as far apart as possible hence minimizing the effect of the holes on the measurement.

The cone with thermocouples installed and all wiring connected is shown in Figure 6.11. After installation of the thermocouples the cone has been placed in an oven overnight to calibrate the thermocouples. After calibration the measuring spread of the thermocouples is within $1.0[^\circ\text{C}]$.



Figure 6.11: Cone for the thermal test with 30 thermocouples and corresponding wiring installed. The wires leave the rear of the cone in two cable batches will be connected to the data acquisition computer.

The liner is designed with 3 different liner sections each of 3 meters in length. The base is a VM50 casing which is single in the first section and followed by a P110- and P110 heavy overlap section. The only difference between the P110 and P110 heavy casing is the increased wall thickness (17.0[mm] instead of 13.7[mm]). Thermocouples are also installed on the liner, 15 in total, 5 per section of liner as shown in Figure 6.12. After a section of the liner has been expanded the setup will be left to rest for 24 hours, letting all heat escape, and starting the next test with a uniform temperature.

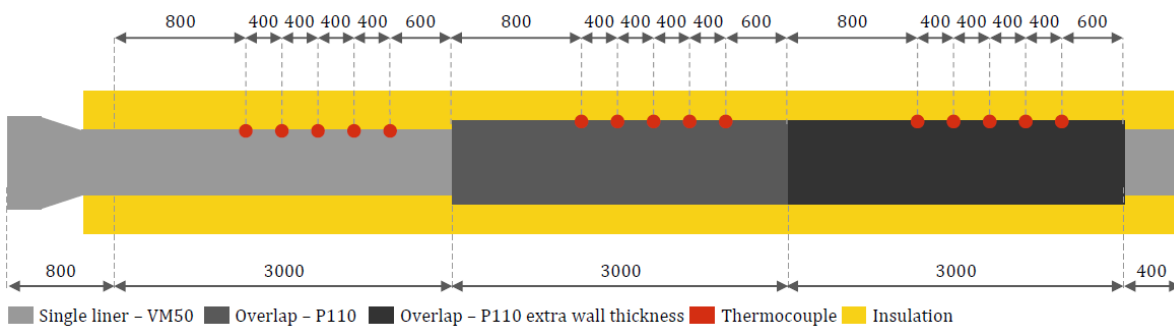


Figure 6.12: Design of the liner for the thermal test, showing the position of the thermocouples in red, the three different sections of the liner in cascading shades of gray and the insulation in yellow. All dimensions are in [mm].

To insulate the liner, thick blankets are used which are strapped around the liner as shown in Figure 6.13



Figure 6.13: Liner for the thermal test installed in the RETF and insulated with thick (gray) blankets to prevent any heat losses.

6.2.4. Results single liner

The single liner section was expanded with a nearly constant expansion force, F_{ex} , the peak was 1137[kN] and the steady state 1063[kN]. The expansion speed, v_{ex} , was constant at 25.75[mm/s] (based on the average between 230[s] and 300[s]) as shown in Figure 6.14. The total work done on the system is calculated by;

$$W_{ex} = F_{ex}v_{ex}. \quad (6.1)$$

Based on the experimental data the expansion work is 27.37[kW].

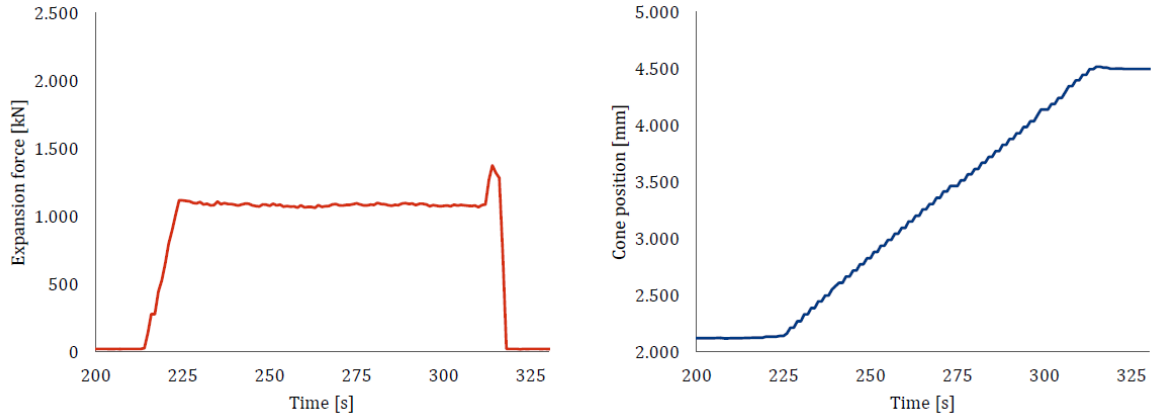
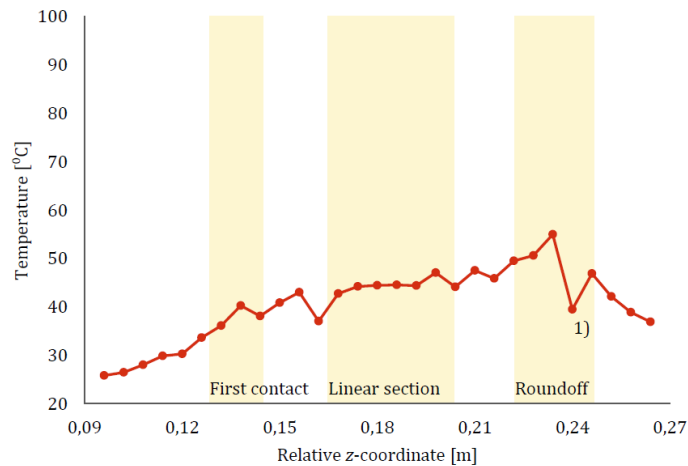


Figure 6.14: Left, the expansion force during single liner expansion. This shows a nearly constant force until the cone comes into contact with the overlap section. The cone position as a function of the time is shown on the right.

The temperatures measured inside the cone stabilized at the end of the test as can be seen from the full results in Appendix H. The steady state temperature profile over the cone during single liner expansion is shown in Figure 6.15. Note that at least two thermocouples malfunctioned during the test, thermocouple 25 gave very low readings, most likely it was positioned incorrectly, thermocouple 30 did not give any data at all. The results of thermocouple 12 are also strange when the value is compared to its neighbors however it is still within range of the expected values.



1) Thermocouple most likely malfunctioned

Figure 6.15: Steady state temperatures measured inside the cone (2[mm] below the contact surface) during single liner expansion. The low value from thermocouple 25, is likely incorrect due to a measurement error.

The thermocouples on the liner reached an average maximum temperature of 47.1[°C] ($\Delta T_{li} = 25.5[°C]$) as shown in Figure 6.16. The first and last thermocouples give lower values, this is most likely due to the fact that the cone was not yet in a thermal steady state at the first thermocouple and the cone did not completely pass the last thermocouple. When the cone is not yet in a thermal steady state, more heat flows into the cone

and hence less into the liner. To calculate the heat flow through the liner (heat output) first the mass flow of the liner is calculated,

$$\dot{m}_{li} = A_{li} v_{ex} \rho_{li}, \quad (6.2)$$

where A_{li} represents the area of the liner normal to the expansion direction and ρ_{li} is the density of the liner. Using the temperature increase, ΔT_{li} , of the liner and the specific heat, $C_{p_{li}}$ the heat output then follows from:

$$Q_{out} = \dot{m}_{li} C_{p_{li}} \Delta T_{li}. \quad (6.3)$$

Based on the experimental data a heat output of 14.89[kW] is found for the single liner expansion.

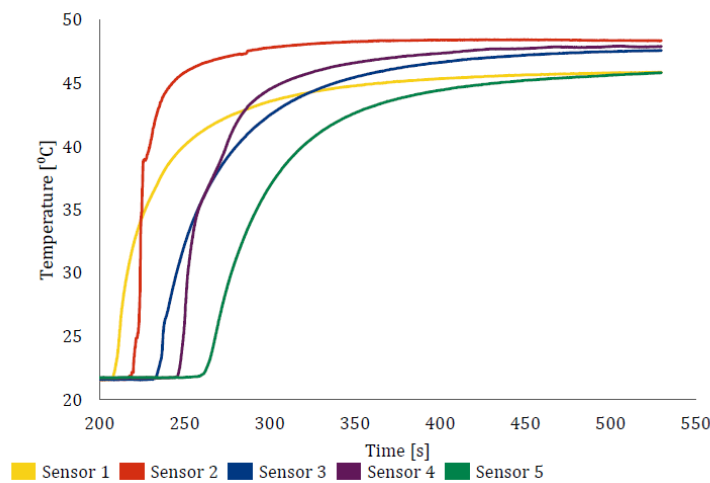


Figure 6.16: Temperature on the outside of the liner during single liner expansion in the thermal cone test. The thermocouples are placed according to Figure 6.12.

When the expansion work is compared to the heat output of the liner;

$$X = \frac{Q_{out}}{W_{ex}}, \quad (6.4)$$

it follows that only 54.4% of the expansion work is returned in the form of heat in the liner.

6.2.5. Results overlap

The overlap section was expanded with an average steady state force of 1692[kN] with a speed of 26.15[mm/s]. The initial peak startup force was 1892[kN]. The steady state parameters are determined by the average value between 70[s] and 160[s]. This resulted in an expansion work, calculated according to Equation 6.1, of 44.24[kW]. The force and speed for the overlap expansion are shown in Figure 6.17.

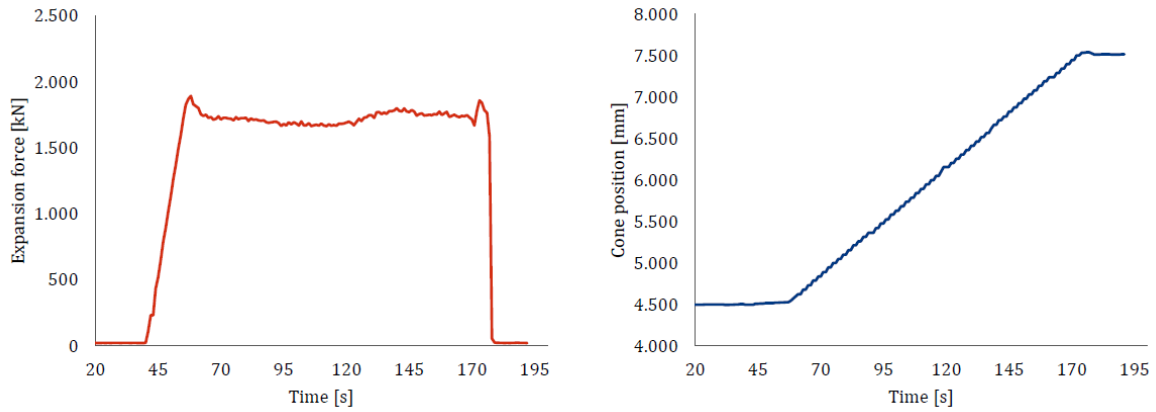
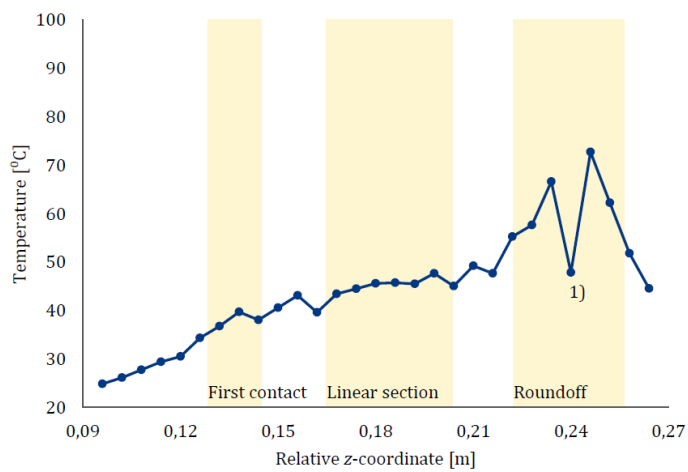


Figure 6.17: Left, the expansion force during overlap expansion. The expansion force shows a clear decrease over time as the lubricant starts to heat up. The right figure shows the cone position over time.

The cone temperature profile of the overlap test shows a very good match with the single liner test from the front of the cone until the round off. At the round off the temperatures are significantly higher, as can be expected due to the extra forces opposed here by the P110 casing. The cone steady state temperature profile for the overlap expansion is shown in Figure 6.18



1) Thermocouple most likely malfunctioned

Figure 6.18: Steady state temperatures measured inside the cone (2[mm] below the contact surface) during overlap expansion. The low value from thermocouple 25, is likely incorrect due to a measurement error.

On the liner an average maximum temperature of $40.5[^\circ\text{C}]$ was measured ($\Delta T_{li} = 18[^\circ\text{C}]$). Again it is seen that the system was not yet in a full steady state at the first thermocouple, hence a slightly lower maximum temperature. The result from the liner thermocouples during overlap expansion are shown in Figure 6.19. The heat output through the liner, calculated using Equations 6.2 and 6.3, is $26.44[\text{kW}]$.

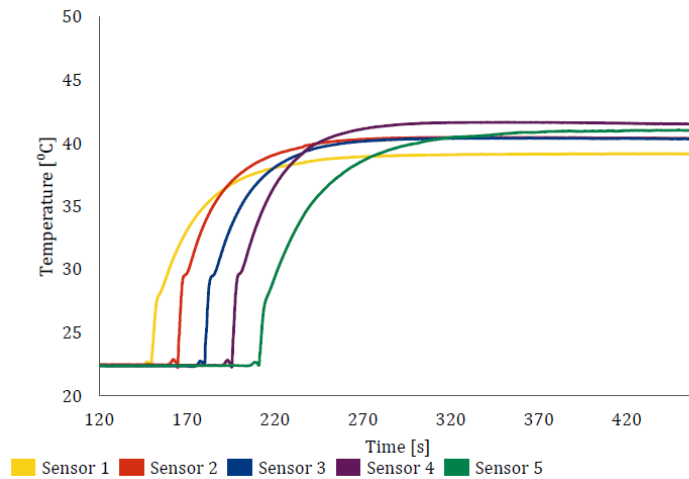


Figure 6.19: Temperature on the outside of the liner during overlap expansion in the thermal cone test. The thermocouples are placed according to Figure 6.12.

During the overlap expansion 59.8% of the expansion work was found as heat inside the liner, slightly more than the single liner expansion.

6.2.6. Results heavy overlap

The heavy overlap section required so much expansion force that the expansion speed had to be set lower, an average speed of 22.55[mm/s] was reached between 210[s] and 260[s]. Additionally water was sprayed inside the liner before the expansion to activate the lubricant as the expansion force otherwise exceeded the limitations of the RETE. Finally a successful expansion was completed with an initial peak force of 2410[kN] and a steady state force of 2100[kN], resulting in an expansion work of 47.36[kW] as shown in Figure 6.20.

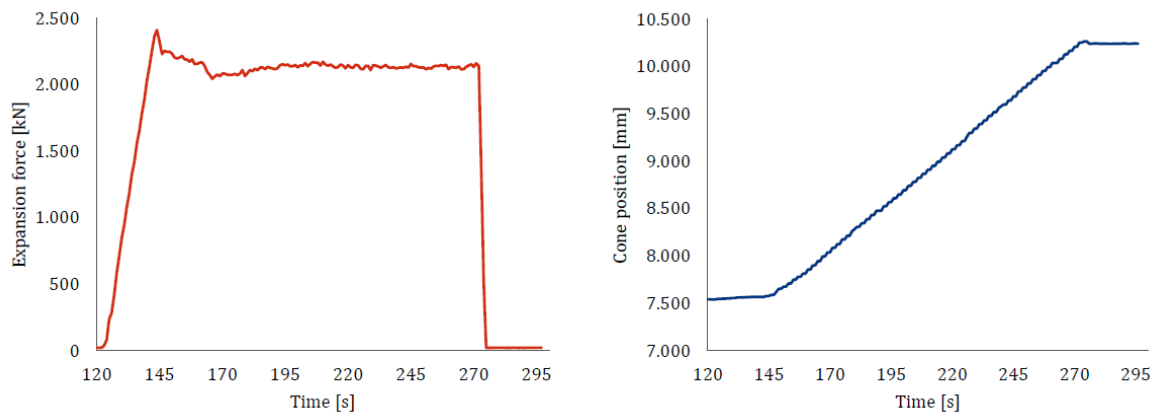
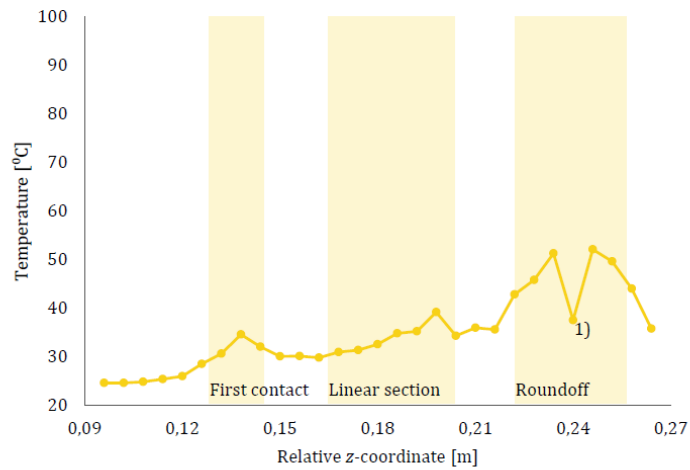


Figure 6.20: Left, the expansion force during heavy overlap expansion. The expansion force shows a clear decrease over time as the lubricant starts to heat up. The right figure shows the cone position over time.

The cone steady state temperatures during the heavy overlap test, as shown in Figure 6.21, were significantly lower than during the first two test. This is most likely caused by spraying the lubricant with water which is known to temporally lead to a significant reduction of the friction coefficient. The film strength of the lubricant is also reduced by the spraying of water, this could explain why the first pressure peak is much more visible in this experiments as compared to the single liner and overlap sections.



1) Thermocouple most likely malfunctioned

Figure 6.21: Steady state temperatures measured inside the cone (2[mm] below the contact surface) during heavy overlap expansion. The low value from thermocouple 25, is likely incorrect due to a measurement error.

The average temperature of the overlap liner after expansion was 44.4[°C] ($\Delta T_{li} = 21.1$ [°C]). Again the reading from the first thermocouple was the lowest but the difference is significantly less in this case. The results from the liner thermocouples during the heavy overlap expansion are shown in Figure 6.22. The heat output through the liner was 35.19[kW].

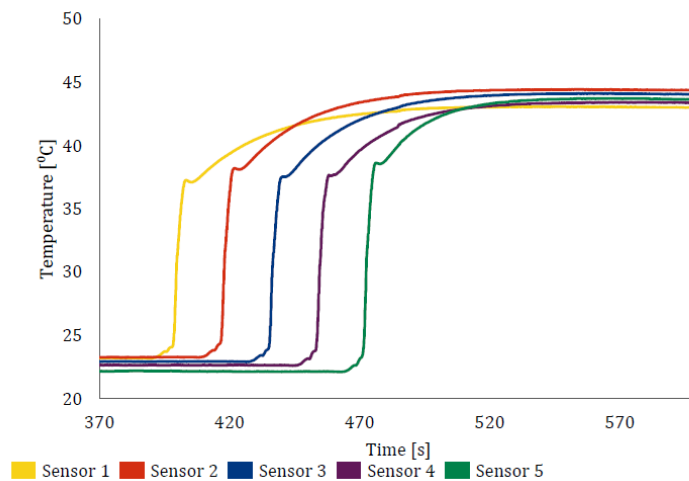


Figure 6.22: Temperature on the outside of the liner during heavy overlap expansion in the thermal cone test. The thermocouples are placed according to Figure 6.12.

The heavy overlap test shows a heat over work ratio of 80.4%, by far the highest of all test.

7

Results

In this chapter the results of the thermal test are compared to the model. The model is configured according to the test case, as given by Appendix J, so that the output should be comparable to the experimental results. A calibration step is made to bring the numerical and experimental results even closer together. The final step is to set the expansion parameters according to the base case, as in Appendix I, so that the results for a field expansion are found.

7.1. Calibration & Validation

Due to the large number of unknowns and uncertainties in the input parameters some calibration is required to fit the model to the experimental results. The calibration is done in a few steps as described in the sections below.

7.1.1. Pressure profile & Cone temperatures

As described in Section 3.1, some doubt exists on the validity of the pressure profiles determined by FEA analysis from 4RealSim (Figures 3.4 & 3.5). It is known that these pressure profiles over predict the expansion force and they are mesh dependent. The results from the thermal cone test can be used to give some new insights on these pressure profiles.

Rear pressure peak

First the rear pressure peak is investigated. Due to the high local pressure the lubrication here is in the boundary lubrication range, as described in Section 3.1. The friction coefficient is therefore expected to be well represented by the friction coefficient as given in Figure 3.2. Assuming that the heat transfer model is valid this means that locally there is only one unknown variable, the contact pressure. When the rear pressure peak is reduced by about 20% as compared to the FEA results a good match is obtained between the model and experimental results for both the single and overlap expansion as shown by Figure 7.1.

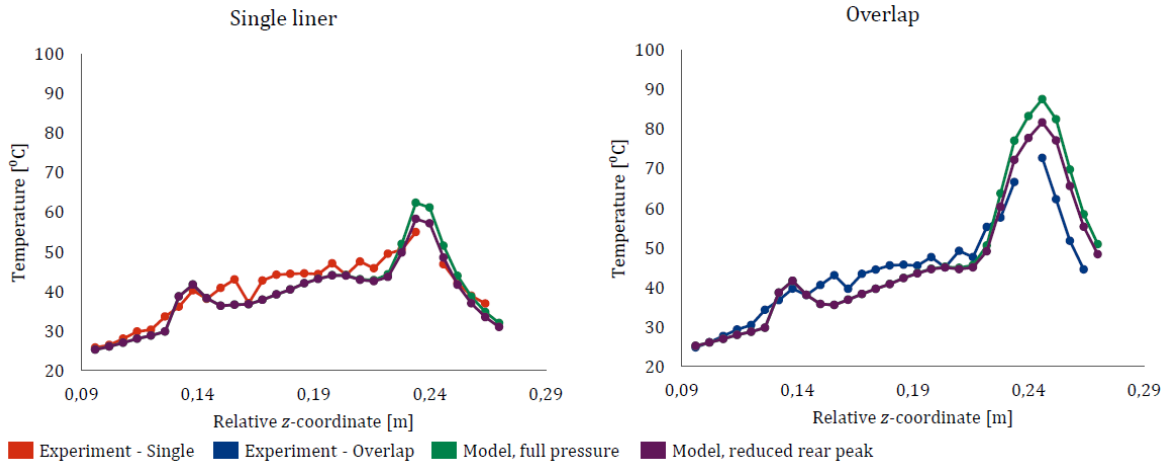


Figure 7.1: Comparison of the experimental cone temperatures and model results using the full pressure profile and the downscaled rear peak. The left figure shows the single liner expansion and the right figure the overlap expansion.

Note that although this correction is valid for the steady state, there may be time transient effects which cause the initial pressure peak to be higher. The next section goes into more details on these effects.

Linear section

When looking at the results of the model in Figure 7.1 a dip in the temperature can be seen behind the front pressure peak which is not visible in the experimental results. In line with the theory developed by Brinkhuis, it could well be possible that a film of lubricant forms over (a part of) the contact area which has enough strength to carry the liner [7]. If this film would indeed form behind the front pressure peak locally the pressure would increase while decreasing it elsewhere, for instance at the rear pressure peak. To validate this theory the pressure profile is adjusted so that the linear section is stretched to connect with the front pressure peak as shown by Figure 7.2.

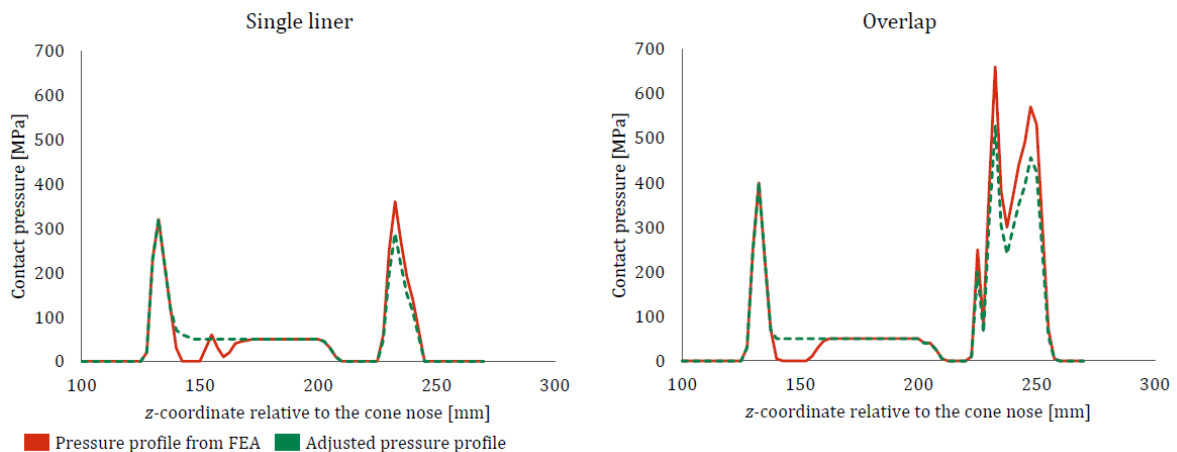


Figure 7.2: The left figure, shows the pressure profile for a single liner expansion and the right figure for an overlap expansion. In both figures, the red line is the pressure profile determined by FEA analysis from 4RealSim. The green line, indicates an adjustment to this pressure profile based on the theory of lubricant film forming and the experimental results.

This adjusted pressure profile is inserted into the model and the results shown in Figure 7.3 are obtained. Their match with the experimental results for both the single liner and overlap section is remarkable.

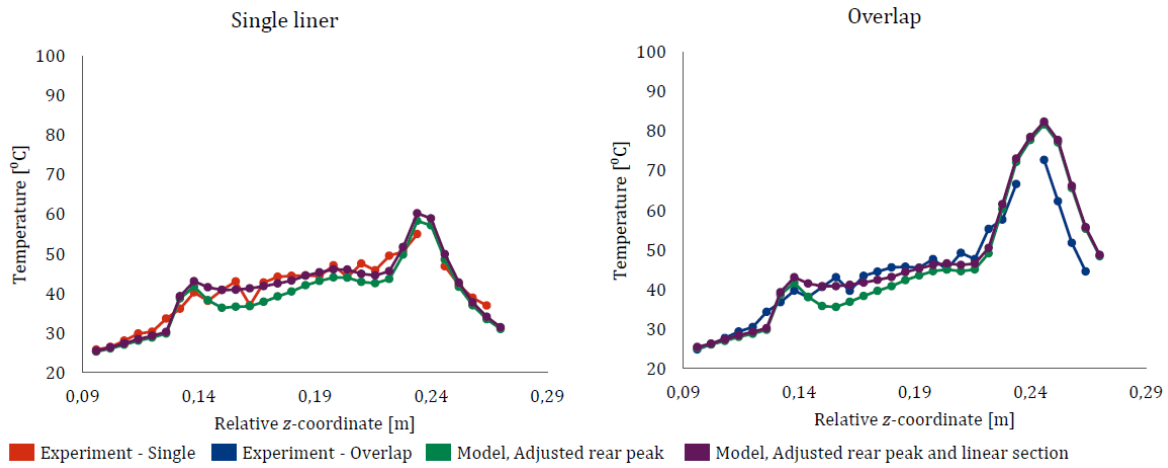


Figure 7.3: The purple line, shows result from the model using the adjusted pressure profile shown in Figure 7.2. This purple line, matches with the experimental results from both the single liner expansion (left) and overlap expansion (right). The green line, shows the result of the model with only the downscaled rear peak.

Another bit of evidence supporting Brinkhuis' theory is found in the time transient behavior of the thermocouples in the area between the front pressure peak and the linear section. Thermocouples located directly under a pressure peak show an immediate response when expansion starts and hence frictional heat is created. The thermocouples located in the area between the linear section and the front pressure peak however don't show such a quick response but show a time delay before they start to heat up. This time delay can be correlated with the required time to form the lubricant film and hence redistribute the pressure over the cone. Figure 7.4 shows the difference between the thermocouples with a direct and indirect response.

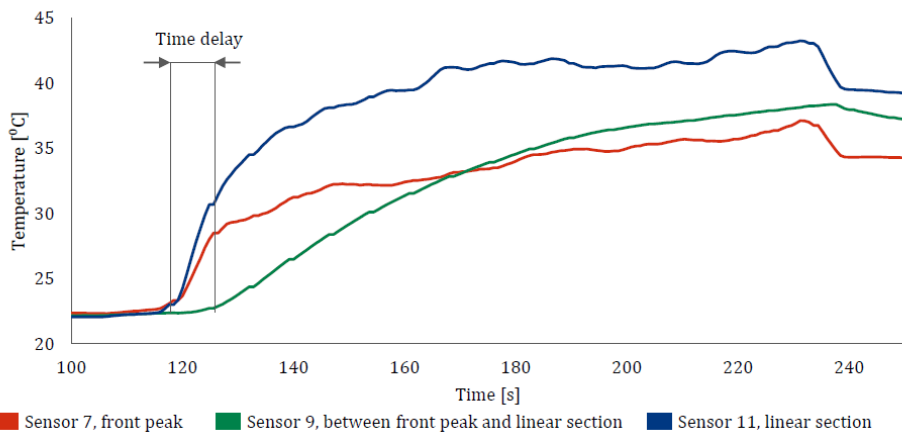


Figure 7.4: Temperature of three thermocouples inside the cone as a function of the time. Thermocouple 7 (red line), is located below the front pressure peak, thermocouple 11 (blue line) at the linear section and thermocouple 9 (green line) in between these two. It can be seen that thermocouple 9 does heat up, but only starts heating up a few seconds later than the start of the expansion.

The integral of the proposed adjusted pressure profile, as shown in Figure 7.2, with respect to the contact area is nearly identical to that of the pressure profile obtained from the FEA results. Hence the force applied on the liner to induce the plastic deformation is retained. However the distribution of this force has changed and further analysis would be needed to verify if the pressure profile alteration is also mechanically sound.

Film strength of RPSLF

The theory of film development and the adjusted pressure profile shows good comparison with the results of the single and overlap experiments. The temperature profile of the heavy overlap experiment however shows significantly different behavior as is shown by Figure 7.5.

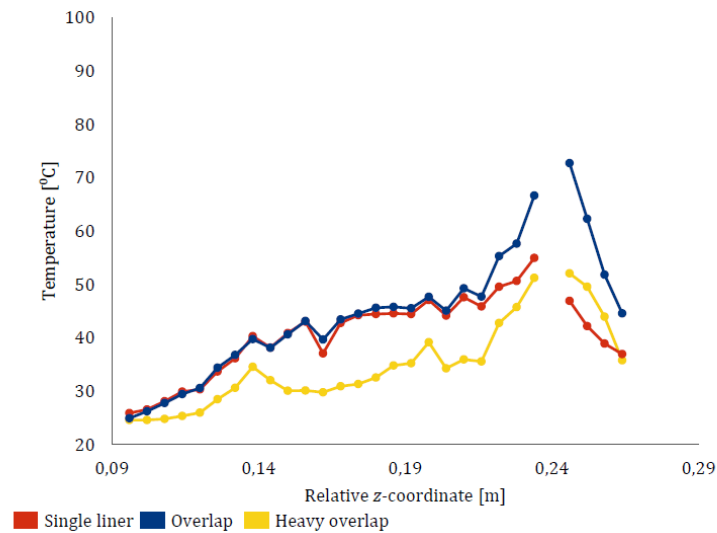


Figure 7.5: Comparison of the steady state temperature profile in the cone measured with the thermal cone test. The single liner and overlap expansion show good agreement. During the heavy overlap expansion the cone was much colder, likely due to the reduced friction coefficient as a result of the spraying of water.

As discussed in Section 6.2.6, the lubricant was sprayed with water prior to the heavy overlap test. Spraying water on RPSLF is a known trick to temporarily decrease the friction coefficient, this was required as the expansion force otherwise exceeded the pulling capacity of the RETF. Another effect of the water on RPSLF is that it decrease the film strength and hence the lubricant may no longer be able to carry a part of the load redistributed from the rear peak. This hypothesis can be tested by running a simulation with the unaltered pressure profile (no redistribution by a lubricant film) but a lower friction coefficient of $\mu = 0.055[-]$. Figure 7.6 shows that there is indeed agreement between the heavy overlap experiment and the low friction coefficient model. Obviously the rear peak does not match as a pressure profile for the heavy overlap section was never determined by FEA analysis.

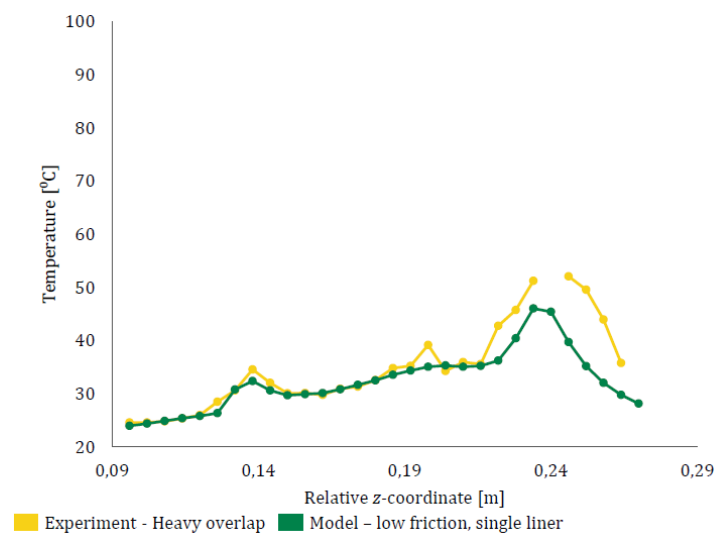


Figure 7.6: Using the FEA pressure profile for single liner expansion and a friction factor of $\mu = 0.055[-]$, the model shows a very good agreement with the results of the heavy overlap expansion.

Expansion force

As a final validation for the adjustment of the pressure profile, the time transient expansion force can be compared between the model and the experimental results. This comparison is shown in Figure 7.7 and is found accurate to within 6.0%. The slight overshoot could be due to the fact that the film of lubricant formed over the linear section may have a lower friction coefficient as it moves from the boundary lubrication to the

hydrodynamic lubrication regime. The model does not take this effect into account and assumes that the friction coefficient only depends on the temperature.

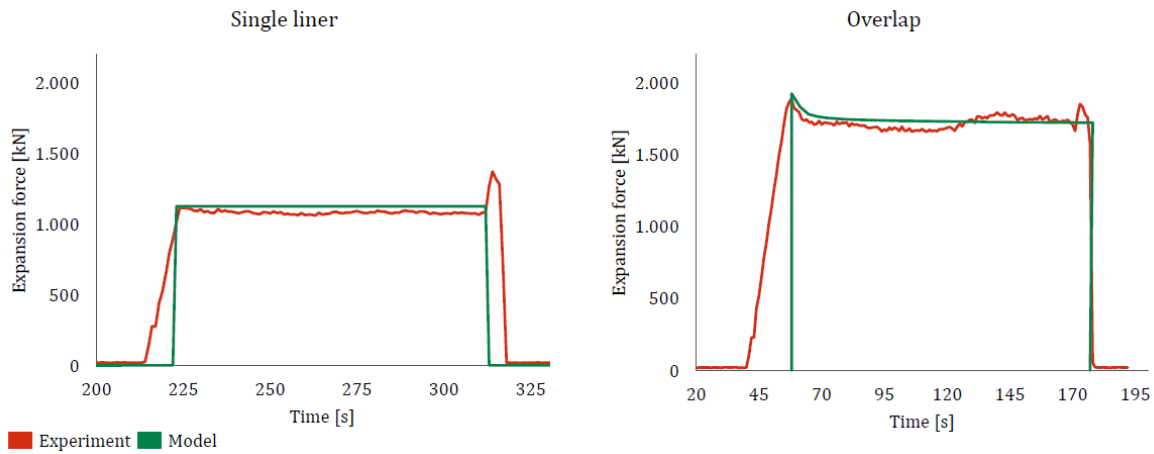


Figure 7.7: The expansion force from the experiments is shown in the red line and from the model in the green line. It can be seen that there is a good match for both the single liner expansion (left) and the overlap expansion (right).

7.1.2. Plastic deformation & the Zehnder model

In Section 3.2 the Zehnder model is used to calculate a strain dependent Taylor-Quinney coefficient. The constant C has initially been chosen so that roughly the steady state value of $\beta = 0.9[-]$ is found. Now that the heat generation due to friction is known, it is possible to calibrate this constant so that the temperature increase in the liner is matched between the model and the experiments. For VM50 a value for $C = 11[-]$ is found suitable and for P110 $C = 9[-]$ is found. Zehnder states that this constant should be in the order of 10, hence the values found here seem reasonable. The calibrated strain dependent Taylor-Quinney curves for VM50 and P110 are shown in Figure 7.8.

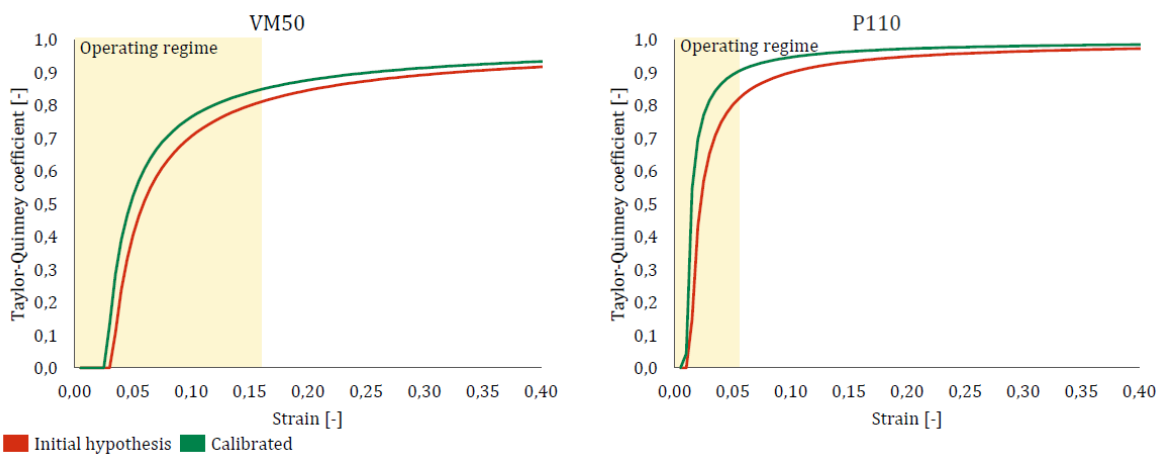


Figure 7.8: Calibrated, green line, and original, red line, strain dependent Taylor-Quinney curves for VM50 (left) and P110 (right)

7.1.3. Heat Partitioning

To prove that the heat output truly represents the major part of the heat input into the system the heat partitioning at the contact surface is analyzed. The heat partitioning indicates the average fraction of frictional heat which flows into the liner. Figure 7.9 shows the heat partitioning for a single liner and overlap expansion. It is seen that initially a lot around 30% of the frictional heat flows into the cone. However, as the cone heats up over time more and more heat is transferred into the liner. After 120[s], around 95% of the frictional heat is transferred directly into the liner.

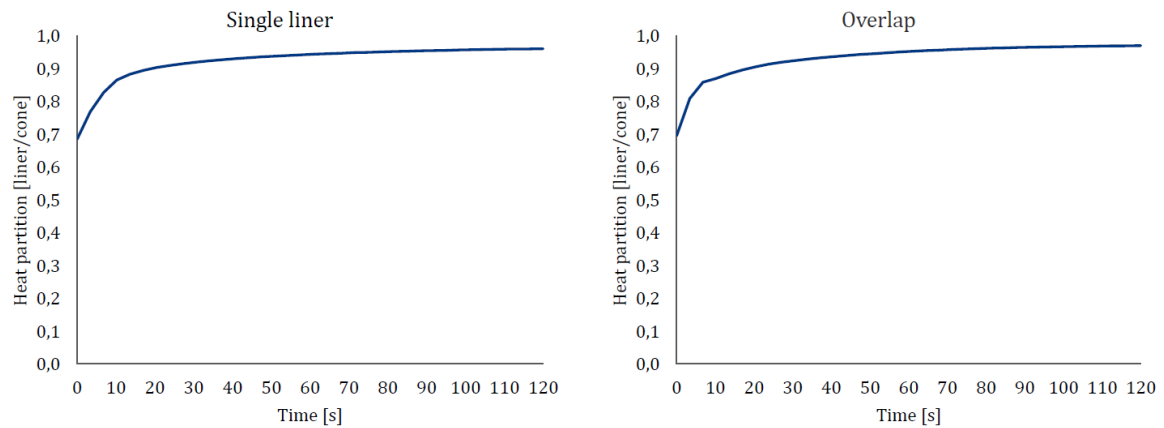


Figure 7.9: The fraction of the frictional heat which flows into the liner as a function of the time for both the single liner (left) and overlap expansion (right). A value of 1 indicates that all frictional heat flows into the liner.

7.1.4. Heat balance

Now that both heat sources have been calibrated the heat balance over the entire system can be verified, the result is shown in Tables 7.1 and 7.2. After the calibration of the model, its accuracy for both the single and overlap expansion is in the order of 5%.

Table 7.1: Comparison of the heat balance of a single liner expansion between the thermal cone experiment and the model.

Parameter	Unit	Experiment	Model	Error
Peak expansion force	kN	1137	1127	-0.9%
Steady expansion force	kN	1063	1127	6.0%
Expansion speed	mm/s	25.75	26.00	1.0%
Expansion work	kW	27.37	29.30	7.0%
Heat input	kW	-	21.63	-
ΔT_{liner}	°C	25.5	27.1	6.1%
Heat output	kW	14.89	15.80	6.1%
Heat/work ratio	-	54.4%	53.9 %	-0.9%

Table 7.2: Comparison of the heat balance of an overlap expansion between the thermal cone experiment and the model.

Parameter	Unit	Experiment	Model	Error
Peak expansion force	kN	1862	1930	3.6%
Steady expansion force	kN	1692	1724	1.9%
Expansion speed	mm/s	26.15	26.00	-0.6%
Expansion work	kW	44.24	44.82	1.3%
Heat input	kW	-	34.40	-
ΔT_{liner}	°C	18.0	17.6	-2.2%
Heat output	kW	26.44	25.85	-2.2%
Heat/work ratio	-	59.8%	57.7 %	-3.5%

7.1.5. Extrapolation of the results to the contact surface

During the experiments, the thermocouples inside the cone measured the temperature at 2[mm] below the contact surface. The model is able to calculate the temperature at these locations and can also calculate the temperature exactly at the contact surface. The comparison between the thermocouple temperatures and contact temperatures according to the model are shown in Figure 7.10. Due to the locally high thermal gradients the contact temperature at the pressure peaks can be up to 15[°C] higher than the thermocouple temperature.

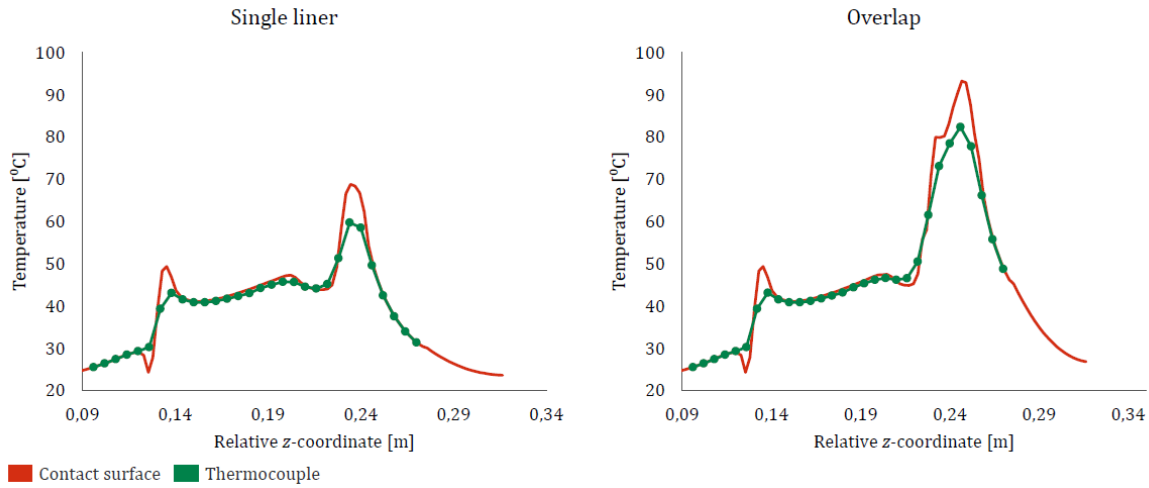


Figure 7.10: Extrapolation of the measured temperatures 2[mm] below the contact surface (green line) to the temperature at the contact surface (red line). Especially at the pressure peaks, there is a high local thermal gradient and the contact surface can be up to 15[°C] hotter than the thermocouple measurement.

7.2. Results for the base case

Now that the test case has proven the validity of the model, the parameters are changed to that of the base case; a single liner and overlap section at down hole conditions, with a field-used expansion speed. The expansion force is now lower due to the reduced friction coefficient at elevated temperatures as is shown in Figure 7.11.

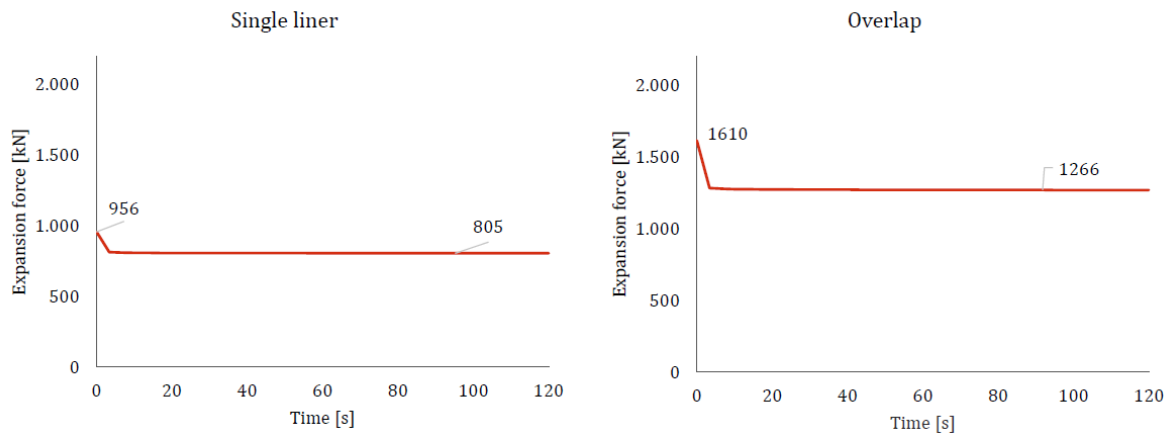


Figure 7.11: The figure shows the expansion force over the time for a base case single liner expansion (left) and overlap expansion (right). Due to the higher temperature and velocity as compared to the test case, the expansion force stabilizes much quicker.

Naturally, the temperatures of the cone and the liner are a lot higher due to the elevated down hole temperature and significantly higher expansion speed. The surface temperature distribution after 120[s] is shown in Figure 7.12 and the temperature profile at the contact and the outside surface of the liner is shown in Figure 7.13.

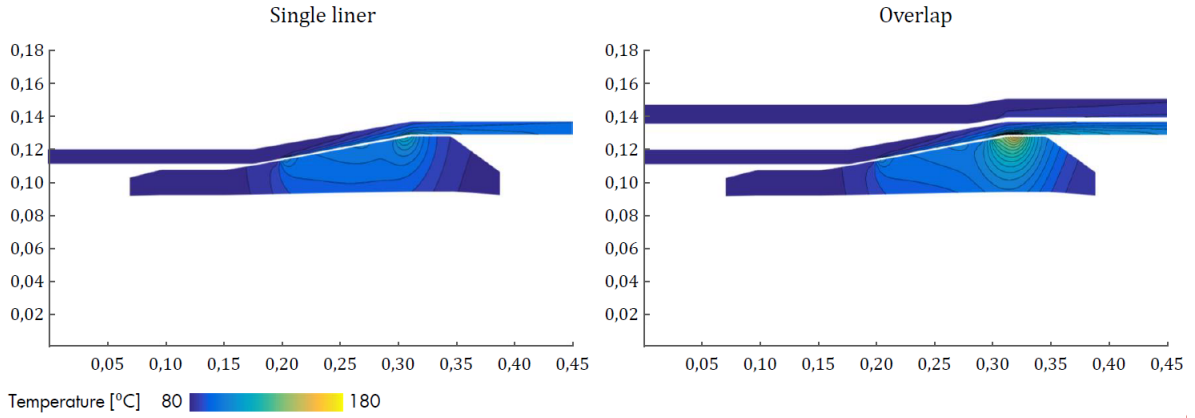


Figure 7.12: Temperature distribution in the cone and the liner after 120[s] of base case expansion. Left shows the single liner expansion with the relatively homogeneous heating of the cone, right the overlap expansion, with a clear temperature concentration at the rear peak.

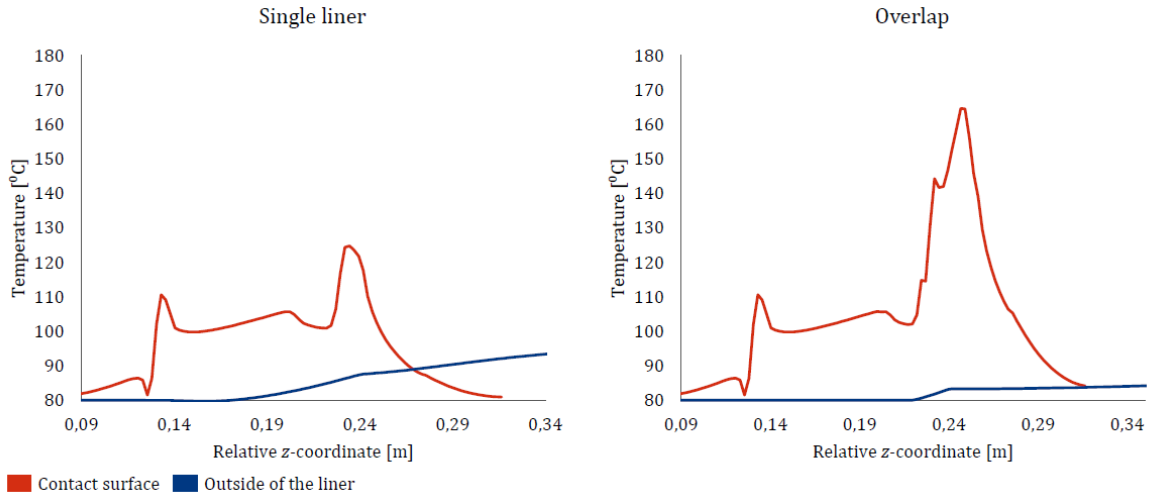


Figure 7.13: Contact surface temperature (red line) and liner temperature profile (blue line) after 120[s] of base case expansion as a function of the position relative to the nose of the cone.

The peak contact temperature of a down hole overlap expansion is 164.4[°C], which is still well below the decomposition temperature of RPSLF (250[°C]). Furthermore, the temperature increase in the liner is 17.2[°C] during overlap expansion, which is comparable to the results from the test case.

7.3. Sensitivity Analysis

Based on the base case, a sensitivity analysis is conducted. All parameters are increased by 20% and the effect on the peak contact temperature is analyzed. Note that although some of these parameters may not influence the peak contact temperature, they may have an influence on the temperature distribution of the cone or liner. The parameter sensitivity is conducted by means of non-dimensional, logarithmic sensitivities;

$$\frac{d_L T}{d_L X} = \frac{X}{T} \frac{dT}{dX}, \quad (7.1)$$

in which T is the peak contact temperature and X the value of analyzed parameter. In some cases, it is hard to define the base value of the parameter X as it can be a variable of for instance space or temperature. In these cases the parameter has been altered such that it is increased 20% over the entire range which leads to the following simplification:

$$\frac{X}{dX} = \frac{1}{0.2} = 5. \quad (7.2)$$

The result of the sensitivity analysis is shown in the form of a tornado plot in Figure 7.14. High absolute values indicate a strong correlation between the peak contact temperature and the analyzed parameter. Negative values indicate an inverse correlation between the parameter and the peak contact temperature.

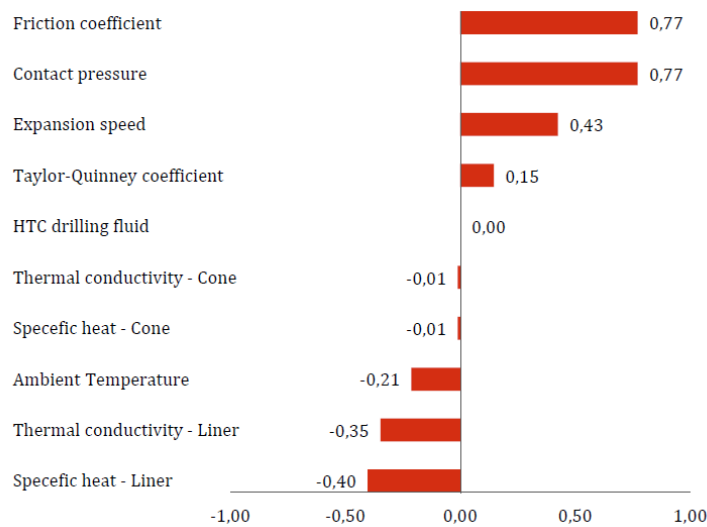


Figure 7.14: Logarithmic sensitivity analysis, impact on peak contact temperature when the value of the parameter is increased. Higher absolute values indicate a stronger correlation, a value of 1 indicates a linear correlation and negative values indicate an inverse correlation.

Friction coefficient & contact pressure

From Figure 7.14 it is evident that the peak contact temperature is most sensitive to the friction coefficient and contact pressure. This is expected as these have a direct correlation with the highly concentrated heat source at the point of the peak temperature. The effect of both is comparable as they both uphold the same linear relation with the frictional heat source as described in Equation 3.2. The effect is slightly damped as an increase of the temperature leads to a decrease of the friction coefficient (until a certain limit) and hence decreases the frictional heat source.

Expansion speed

The expansion speed has a linear correlation with both the frictional- and plastic deformation heat sources. However, when the expansion speed increases also the cooling effect of the liner on the cone is increased hence reducing the peak contact temperature.

Taylor-Quinney coefficient

An increase of the Taylor-Quinney coefficient can lead to a significant increase of the heat source due to plastic deformation. This heat source is however not concentrated at the contact area where the peak temperature and pressure are located. Because of this difference in the location and concentration of the heat sources, the peak contact temperature is less sensitive to the plastic deformation heat source as compared to the frictional heat source.

HTC drilling fluid, thermal conductivity and specific heat of the cone

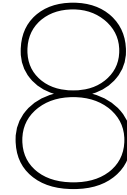
Only a very limited amount of heat flows through the cone after a thermal steady state has been reached. Due to this small heat flow; even significant changes to the thermal resistances obstructing this flow, have limited effect on the peak contact temperature. The thermal resistances here are the conduction through the cone (cone thermal conductivity and specific heat), conduction through the drill string and convection with the drilling fluid.

Ambient temperature

The ambient temperature has a reverse impact on the peak contact temperature increase, there are two main driving effects. First of all, in a general sense a higher temperature means a lower friction coefficient and hence less frictional heat. The strength of this effect is also correlated to the base temperature at which the sensitivity analysis is conducted, as the friction coefficient is not a linear function of the temperature. The second, much smaller, effect is that the elevated temperature slightly softens the steel and less work is required for the plastic deformation of the liner.

Thermal conductivity and specific heat of the liner

Increasing the thermal properties of the liner will significantly decrease the peak contact temperature. First of all, the thermal conductivity of the liner helps to increase the heat partitioning at the contact surface so that a larger portion of frictional heat is directly absorbed by the liner. Next the specific heat is linearly correlated with the volumetric heat capacity of the liner (ρC_p) which is the driving parameter behind the "convective" heat transfer term inside the liner, responsible for removing roughly 95% of the heat from the system.



Conclusions & Recommendations

The aim of this research is to create a model which can calculate the peak contact temperature of the lubricant during the expansion process, under field and laboratory circumstances. To develop this model the heat sources from friction and plastic deformation are analyzed in Chapter 3. A custom numerical heat transfer model is then created in Matlab as described in Chapter 4. Boundary conditions are analyzed and modeled in Chapter 5. Experiments are designed and executed to verify the model, as described in Chapter 6. Finally, the results of the experiments are compared to the model in Chapter 7, where after the results are extrapolated to field conditions. This chapter gives the final conclusion in Section 8.1 and recommendations for improvements and further research in Section 8.2.

8.1. Conclusions

The conclusion is divided into four sections, first the heat sources are described; friction in Section 8.1.1 and plastic deformation in Section 8.1.2. After which the heat transfer model is evaluated in Section 8.1.3. Finally, Section 8.1.4 answers the main goal of the research and provides the peak contact temperature of a down hole expansion.

8.1.1. Heat due to friction

The strong correlation between the frictional heat and the temperature of the contact surface is more than evident from both the numerical and experimental results. This heat is driven by three main parameters; the friction coefficient, the contact pressure and the expansion speed. Of these three the expansion speed can be controlled, the other two must be modeled.

Friction coefficient

Judging by the comparison of the time transient behavior of the expansion force between the model and experiments the temperature dependent modeling of the friction coefficient seems adequate. Unfortunately a small error remains, likely due to the fact that film forming leads to an additional reduction of the friction coefficient. The driving principle here could be the (local) transition from the boundary lubrication to the mixed or hydrodynamic lubrication regimes. This effect is not accounted for in the model.

Contact pressure

The pressure profile is validated qualitatively at the initial onset of expansion. During the first few seconds of expansion it is likely that a film of lubricant builds up which redistributes roughly 20% of the pressure from the rear peak of the cone to the linear section. Although both steady state and time transient analysis of the cone temperatures support this theory it must be stated that direct measurement of the pressure is not possible and therefore hard evidence for the forming of this film and hence redistribution of the pressure is still missing.

8.1.2. Heat due to plastic deformation

The temperature of the liner after expansion in the experiments clearly shows that a significant part of the work is done on the system is not converted into heat. For the single liner expansion, experiments show

54.4% of the work being converted into heat and 59.8% during the overlap expansion. As all frictional work is converted into heat this "loss" of energy must be due to its storage in the liner, both in the form of elastic energy and metallurgical dislocations and transformations. The Zehnder model gives a decent approximation (error < 5%) for this behavior with a heat/work ratio of 53.9% for single liner expansion and 57.7% for overlap expansion. The last remaining uncertainty is the exact value of the material dependent constant in the Zehnder model, only complicated, dedicated experiments can improve the estimate for this value.

8.1.3. Validity of the heat transfer model

Based on the comparison between the numerical and experimental results on the time transient expansion force, cone- and liner temperature, it can be concluded that the numerical model is valid under testing conditions within a very reasonable degree of accuracy, in the order of 5%. Verification of the down hole boundary conditions is however not always possible. The best example is the convective heat transfer coefficient of the non-Newtonian drilling fluid. A much higher or lower heat transfer coefficient might influence the contact temperature. The impact of the other boundary conditions on the peak contact temperature is expected to be minimal so that the results of down hole simulations should also be fairly accurate. Some care should however be taken when interpreting these results due to the unvalidated boundary conditions.

8.1.4. Peak contact temperature

Based on the results of the numerical model under base case conditions, the maximum contact temperature is 124.7[°C] for single liner expansion and 164.4[°C] when expanding in overlap. As this temperature is well below the lubricant decomposition temperature of 250[°C] the expansion process is safe in this sense and it could even be considered to increase the expansion speed to save time. Furthermore the peak contact temperature is most sensitive to the frictional heat source resulting from the friction coefficient and the contact pressure. A higher expansion speed does increase the peak contact temperature but the effect is weaker than increasing the heat sources as the cooling by the liner is also increased.

8.2. Recommendations

The results from the model are promising and well comparable with the experiments, some factors however can still be improved or require further research.

Verify the influence of water on RPSLF

Judging by the difference between the single liner and overlap test with the heavy overlap test, it looks like RPSLF is extremely sensitive to the presence of water. It would be wise to further investigate this phenomenon by for instance doing ball-on-3 friction test with and without water or a thermal cone test with and without sprayed water.

Verify the absorption of RPSLF into drilling mud

At elevated down hole temperatures RPSLF may well be absorbed by an oil-based drilling fluid. If this is the case, field expansions would not be lubricated by RPSLF but by the oil in the drilling fluid. This would require a new model for the friction coefficient.

Verify the necessity of RPSLF

Running an expansion test without RPSLF but with drilling fluid would give insight in the "worst case" conditions of down hole expansion. As the friction coefficient of an expansion based solely on oil is expected in the range of $\mu = 0.12[-]$, such a test could show if it is even necessary to use RPSLF in specific cases.

Measure the strain dependent Taylor-Quinney coefficient

The constants used in the Zehnder model have been estimated and calibrated with the experiments and seem to yield acceptable results. Due to the indirect measurement the certainty of these values is limited. It would be wise to design an dedicated experiment and specifically measure these constants.

Use the knowledge of the strain dependent Taylor-Quinney coefficient

If a field expansion appears to come close to the critical temperature of the lubricant, it could be considered to use a slightly smaller cone and hence reduce the strains in the liner. This will not only reduce the pressure on the cone and the strain in the liner, but could also significantly decrease the Taylor-Quinney coefficient. This would imply that although the expansion force may reduce only slightly the heat generation could reduce much more.

Analyze the effects of the alteration of the pressure profile

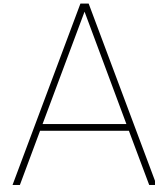
Alteration of the pressure profile due to film forming of the lubricant works well for the thermal model. Before it is completely accepted as the truth further analysis should be done on the effect of this pressure profile in the models for the deformation field in the liner, expansion force and ironing.

Investigate the effect of stick-slip

The model uses a constant expansion speed which is in good agreement with laboratory conditions. In the field, often a stick-slip effect is observed. It may be interesting to investigate the effect of different velocity profiles on the peak contact temperature.

Investigate the thermal properties of (potential) new liner types

The VM50 liner is by far the most commonly used for mono-diameter wells, other types are however available. As the thermal properties of the liner have such a significant impact on the peak contact temperature, these should be measured for any (potential) new types of liners.



Components

This appendix provides an overview of all the components within the scope of the thermal analysis. For each component the relevant dimensions and material properties are provided. Many material properties have been measured specifically for this research.

A.1. Cone

The cone consists of one solid piece of metal with a conically shaped outer surface and a fixed inner diameter. On the outer surface numerous different angles and fillets with specific radii are used to fit the mechanical engineering demands for the plastic deformation. Most of these minor radii or angles have limited influence on the overall shape of the bulk material which makes them irrelevant for thermal analysis.

A.1.1. Dimensions

In order to fit a somewhat simplified mesh to the cone the choice is made to slightly simplify the geometry of the cone allowing the fit of a quadrilateral-based skewed mesh. A cross-sectional view of the actual geometry of the cone is shown in Figure A.1, the simplified regions are highlighted in red.

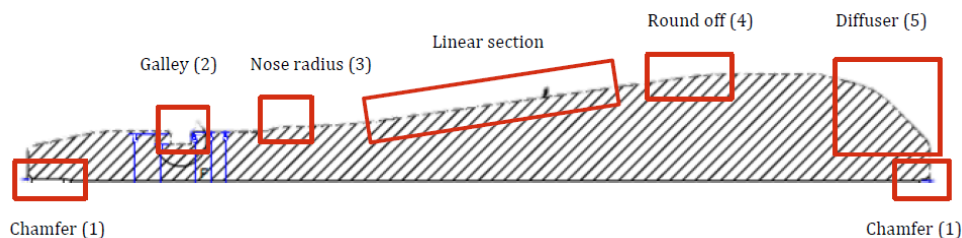


Figure A.1: Geometry of the cone in the r - z plane with the regions at which simplifications are used highlighted.

The simplifications to the geometry are shown in Figure A.1 and include:

1. Removal of the chamfer on front and rear inner wall of the cone
2. The galley on the front straight section is ignored
3. The nose radius before the linear section is ignored
4. The round off is modeled as 1 angle between two straight sections
5. The rear diffuser is modeled with 1 constant angle instead of 2 with rounded angles
6. All other fillets are ignored

With these simplifications in place the cone can be modeled based on the geometric parameters given by Table J.3 and illustrated in Figure A.2

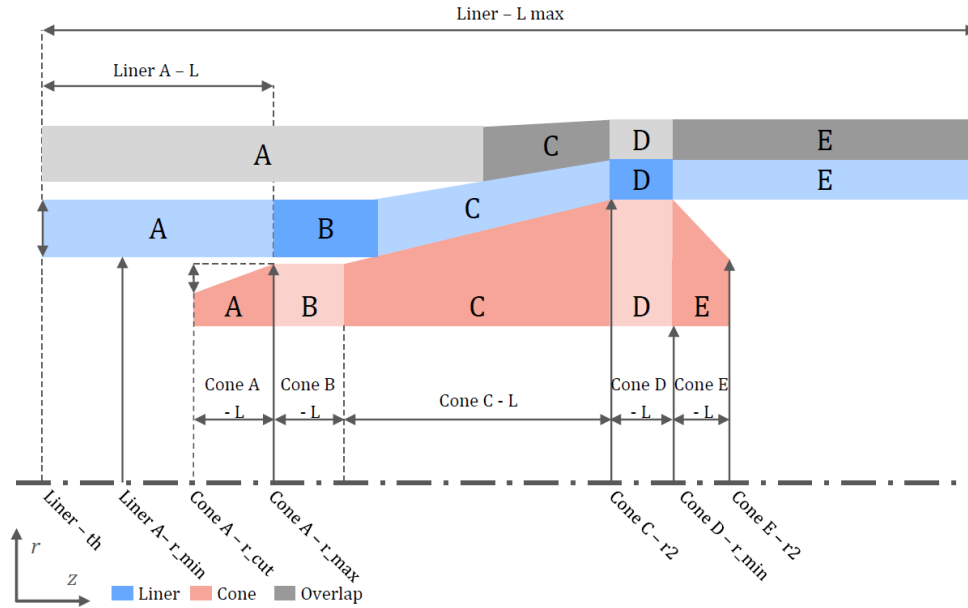


Figure A.2: Naming and location of all dimensions required for the simplified geometries

A.1.2. Material

The cone is made of a hard tool-steel alloy referred to as Sverker-21, produced by Uddeholm. Sverker-21 is known for high wear resistance, high compressive strength and good hardening properties. It consists of, among others; 11.8%Cr, 1.55%C, 0.8%Mo, 0.8%V, 0.4%Mn, 0.3%Si. The main properties of Sverker-21 at room temperature as obtained from the manufacturer are listed in Table A.1 [32].

Table A.1: Sverker-21 Material properties at room temperature

Property	value	unit
Density	7700	$\frac{kg}{m^3}$
Thermal conductivity	14.61	$\frac{W}{mK}$
Modulus of elasticity	210	GPa
Specific heat	460	$\frac{J}{kgK}$

A.1.3. Thermal properties

The thermal properties of Sverker-21 over the full temperature range have been obtained from the manufacturer (Uddeholm) and are shown in Figure A.3.

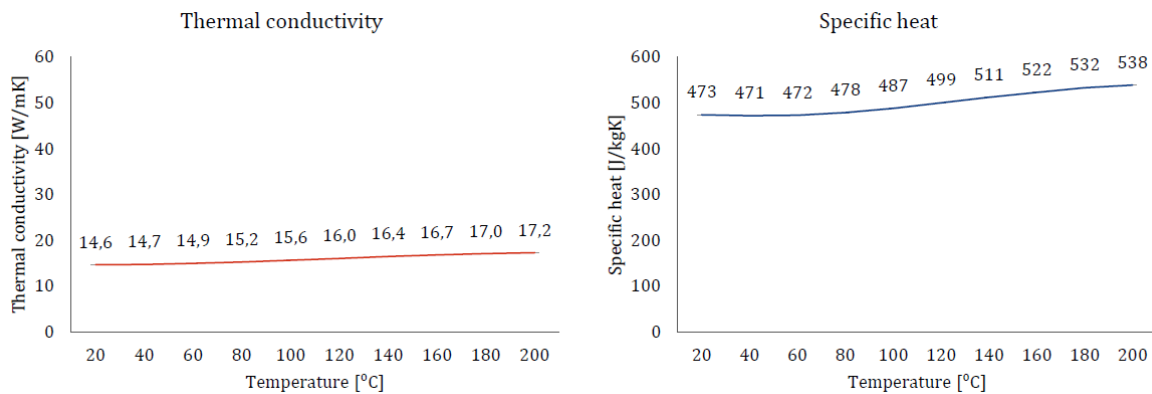


Figure A.3: Thermal conductivity (left) and specific heat (right) as a function of the temperature for Sverker-21 (from Uddeholm)

A.2. Liner - Single

The liner is the steel pipe which prevents the hole from collapsing and which is plastically deformed during the expansion process. In the field many different materials are used in combination with an even greater number of coatings. In this research the focus is on the main types used for mono-diameter applications.

A.2.1. Dimensions

The liner is assumed to be of a perfect circular shape, before and after expansion. Furthermore, it is assumed that the total volume of the liner remains constant during the expansion process. As a consequence, only 3 dimensions are required to model the liner, accompanied by the maximum outer radius of the cone which indicates the inner radius of the liner after expansion their locations are shown in Figure A.2.

A.2.2. Material

VM50 has been selected as the base case material for the liner. This material is a relatively low-alloy steel consisting of among others 0.95%*Mn*, 0.2%*Si*, 0.14%*C*, 0.04%*Al*. Due to the low amount of alloying elements the properties of this steel are close to that of plain carbon steel.

Table A.2: VM50 Material properties at room temperature

Property	value	unit
Density	7845	$\frac{kg}{m^3}$
Thermal conductivity	47.6	$\frac{W}{mK}$
Modulus of elasticity	195	<i>GPa</i>
Specific heat	455	$\frac{J}{kgK}$

A.2.3. Thermal properties

The thermal properties of VM50 have been measured according to the procedure described in Appendix B.2 and the results are shown in figure A.4. It can be seen that the values are quite close to that of plane steel and fairly independent over the temperature.

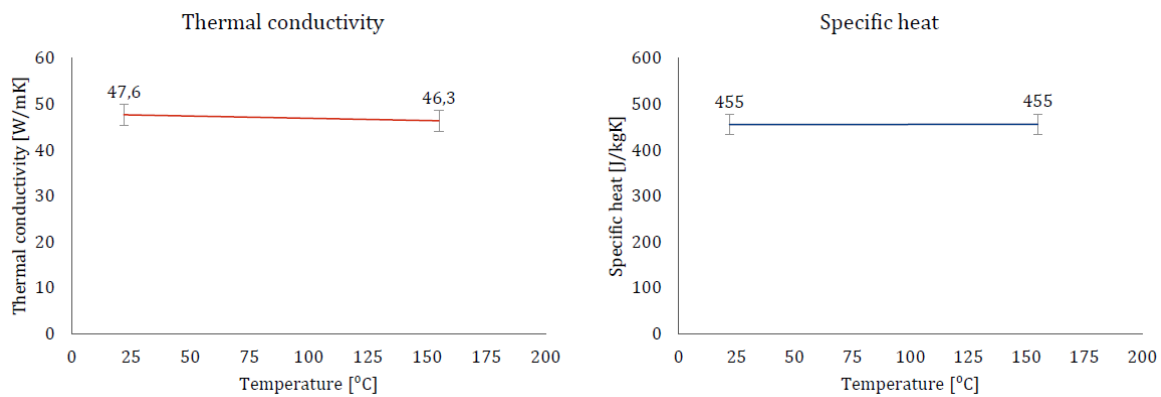


Figure A.4: Thermal conductivity (left) and specific heat (right) as a function of the temperature for VM50 (Measured according to the procedure described in Appendix B.2)

A.2.4. Mechanical properties

As the liner is plastically deformed during the expansion process also the mechanical, strain hardening properties of the material are required for the model. To determine the stress strain behavior of the material the Swift law is used;

$$\sigma = C * (\epsilon_e)^n, \quad (A.1)$$

in which the constant C and exponent n are calculated from tensile experiments as;

$$C = \frac{\sigma_{uts}}{\epsilon_{uts}^n}, \quad (A.2)$$

$$n = \frac{\log \frac{\sigma_{yield}}{\sigma_{uts}}}{\log \frac{\epsilon_{yield}}{\epsilon_{uts}}}, \quad (A.3)$$

based on the yield, σ_{yield} , and ultimate stress, σ_{uts} , accompanied by their respective strains, ϵ_{yield} & ϵ_{uts} , which were previously determined by tension test and shown in Table A.3. Previous research conducted by Wilmlink has proven the validity of this model for this material [35].

Table A.3: Mechanical properties of VM50

Property	value	unit
S_{yield}	390	MPa
S_{uts}	475	MPa
ϵ_{uts}	0.5	
ϵ_{yield}	0.019	

Using Equations A.1 to A.2 and the values from Table A.3 the stress strain curve for VM50 at room temperature can be derived and is shown in Figure A.5.

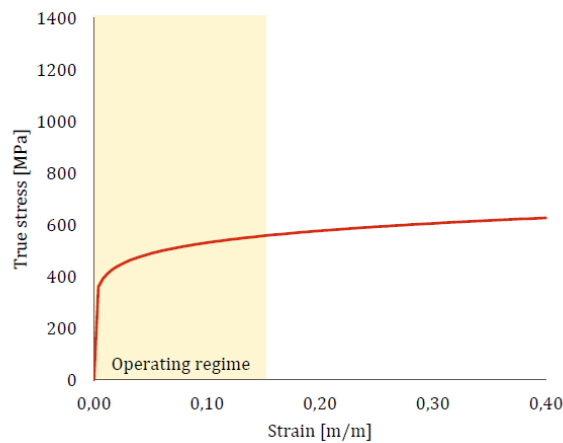


Figure A.5: True stress-strain curve of VM50 based on the Swift-law

At elevated temperatures materials become softer and thus the stress strain behavior changes. To account for this effect the yield and ultimate stresses are corrected for the elevated temperature by means of;

$$\sigma(T) = \sigma(T_0) * \left(1 + \left(\frac{T - T_0}{T_0} \right) * (1 - R) \right). \quad (A.4)$$

In which R is a material property correlated to the rate of softening at elevated temperatures, T is the temperature at which the material properties are determined and T_0 is the temperature at which the measurements were conducted. for steels a value of $R = 1.16[-]$ is used. Calculation of the elevated temperature stress strain behavior is then conducted parallel to the room temperature calculations.

A.3. Liner - Overlap

Some sections exist where two liners are expanded in an overlap. Despite the fact that the expansion ratio for the outer liner is much smaller the higher mechanical properties provide a significant increase in the contact pressure on the cone and hence the expansion force. Aside from further expanding a previously expanded section of VM50 liner, at the top of the expandable section a conventional liner is expanded in overlap, this liner has different dimension and is made of a different material.

A.3.1. Dimensions

Parallel to the assumptions made for the single liner the host liner is assumed to have a perfect circular shape and that its volume is conserved throughout the expansion process. This leads to the same simplified set of dimension required for the single liner.

A.3.2. Material

The typical host liner used for expandable wells is of the type P110. This low-alloy steel consists of amongst others 0.93%Cr, 0.75%Mn, 0.31%C, 0.24%Si, 0.17%Mo, 0.13%Cu and 0.1%Ni. The main properties of P110 are summarized in Table A.4.

Table A.4: P110 Material properties at room temperature

Property	value	unit
Density	7830	$\frac{kg}{m^3}$
Thermal conductivity	40.2	$\frac{W}{mK}$
Modulus of elasticity	210	<i>GPa</i>
Specific heat	455	$\frac{J}{kgK}$

A.3.3. Thermal properties

The thermal properties of P110 have been measured according to the procedure described in Appendix B.2 and the results are shown in Figure A.6. From the results a significant dependence of the thermal conductivity on the temperature can be seen within the expected temperature range.

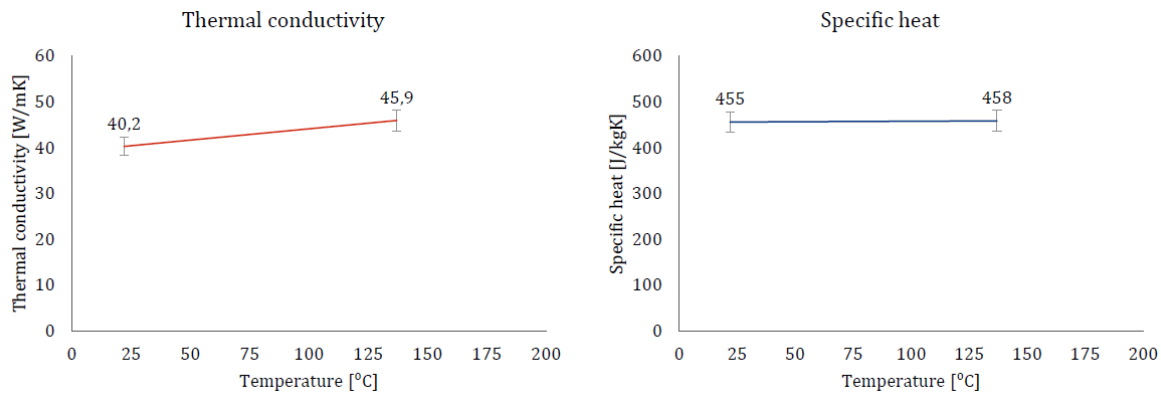


Figure A.6: Thermal conductivity (left) and specific heat (right) as a function of the temperature for P110 (Measured according to the procedure described in Appendix B.2)

A.3.4. Mechanical properties

Despite the limited expansion ratio of the overlap liner plastic deformation still takes place. The mechanical properties are therefore relevant for the model and summarized in Table A.5. Corrections for elevated temperatures are done parallel to the procedure described in Section A.2.4.

Table A.5: Mechanical properties of P110

Property	value	unit
S_{yield}	861	<i>MPa</i>
S_{uts}	965	<i>MPa</i>
ϵ_{uts}	0.38	
ϵ_{yield}	0.006	

A power law stress-strain model is used to describe the stress-strain curve (as in Equation A.1).

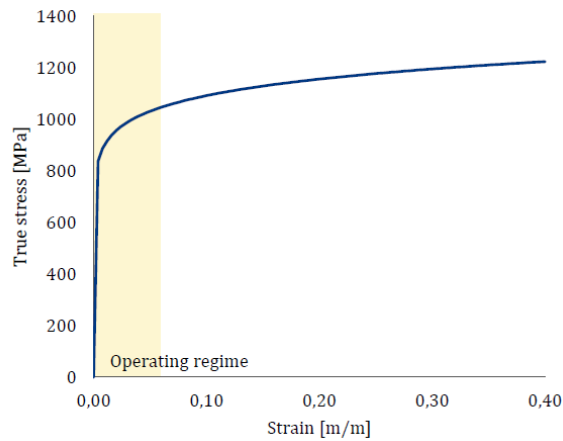


Figure A.7: True stress-strain curve for P110 based on the Swift-law

A.4. Lubricant

In order to reduce the friction, a specialized lubricant has been developed for the expansion process. This specialized lubricant, RPSLF (Rust Preventive Solid Lubricant F) is able to handle high loads and cope with the plastic deformation during expansion under down-hole conditions while remaining chemically and thermally stable. The major complication of the lubricant is that it thermally decomposes when exposed to temperatures above 250[°C]. When the lubricant starts to decompose the friction coefficient and hence the expansion force will increase. This in turn is related to one of the main reasons for this research. The major chemical components of RPSLF are of 50% Calcium Stearate, 31% Polyethylene wax and 13% Acrylic emulsion.

A.4.1. Thermal properties

The layer of lubricant is typically only very thin (several micrometers), and the influence on the heat transfer in the entire system is expected to be minimal, as described in more detail in Section 5.1.1. The thermal properties of the lubricant do however influence the temperature of the material in close proximity to the lubricant layer. Therefore the thermal properties of the lubricant have been analyzed according to the testing procedures described in Appendix B.1, the results of these test are shown in Figure A.8. Measurements at higher temperatures were not possible as the liquid RPSLF starts to boil around 80[°C] at ambient pressure.

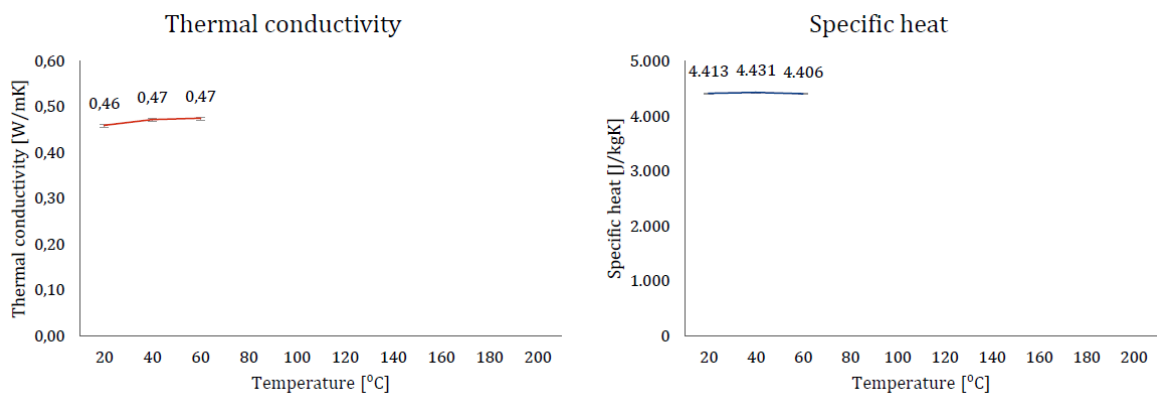


Figure A.8: Thermal conductivity (left) and specific heat (right) as a function of the temperature for RPSLF (measured according to the procedure described in Appendix B.1)

A.5. Drilling fluid

Through the inside of the drill string there is a flow of drilling fluid. During drilling the purpose of this fluid is the transportation of the cuttings (from the drill bit) to the surface. Two main types of drilling fluid exist,

water based and synthetic (oil based). Both come in many different forms with a large variety of additives. For the base case a standard Gulf of Mexico synthetic mud is selected (NGM 9.85A).

Table A.6: NGM 9.85A Material properties at room temperature

Property	value	unit
Density	1557	$\frac{kg}{m^3}$
Thermal conductivity	0.375	$\frac{W}{mK}$
Specific heat	2150	$\frac{J}{kgK}$
Apparent viscosity	0.024	<i>Pa</i> s
Power law exponent	0.3	-
Power law consistency index	0.7	-

A.5.1. Thermal properties

Due to the non-Newtonian aspects of these fluids their thermal properties are not only dependent on the temperature but also of the shear-force [18]. Unfortunately no equipment was available to measure the thermal properties at different shear rates so that they have only been measured when the fluid was at rest. The results of these measurements are shown in Figure A.9. Measurements at higher temperatures were not possible as the the drilling fluid started to boil around 100[°C] at ambient pressure.

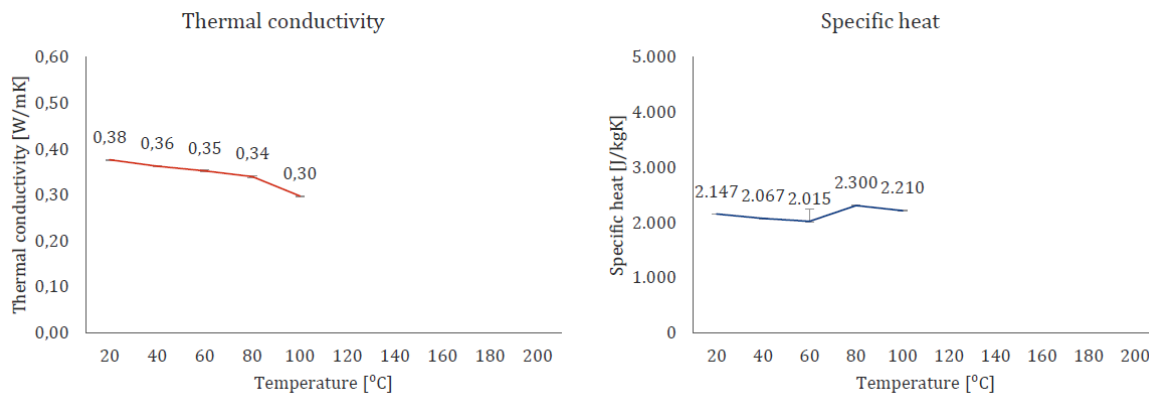


Figure A.9: Thermal conductivity (left) and specific heat (right) as a function of the temperature for the drilling fluid (measured according to the procedure described in Appendix B.1)

A.6. Drill string

Essentially the drill string is nothing more than a thick steel pipe to which the tools are attached such as the cone or drill bit. The drill string is made of high tensile strength AISI4340 steel. The chemical composition consists of, amongst others; 1.8%Ni, 0.8%Cr, 0.7%Mn, 0.4%C and 0.25%Mo [31].

Table A.7: AISI4340 Material properties at room temperature

Property	value	unit
Density	7850	$\frac{kg}{m^3}$
Thermal conductivity	42	$\frac{W}{mK}$
Modulus of elasticity	210	<i>GPa</i>
Specific heat	460	$\frac{J}{kgK}$

A.6.1. Thermal properties

Unfortunately no samples of AISI4340 were available for testing and the manufacturer was not able to provide detailed information. Therefore the thermal properties of AISI4340 are assumed as constants.

B

Measurement of thermal properties

Measuring the thermal conductivity of a material is not straightforward. Several measuring techniques are available each with its own limitations concerning the measuring range and state of the material. In this research two different methods are used. Section B.1 gives the measuring procedure for liquids and Section B.2 for solids.

B.1. Liquids

The liquids are measured using a PSL Systemtechnik LabTemp 30190 which can measure the thermal conductivity of liquids, gels and powders according to the ATSM D2717 standard, the Instationary hot wire method [4]. The machine uses a water cooling- and heating system to ensure a constant and controlled temperature of the sample. Only a very small sample of approximately 50ml is required for this machine. The setup and detail of the hot wire are shown in Figure B.1



Figure B.1: Setup for the measurement of the thermal conductivity of liquids using the hot wire method. The picture on the right shows the wire and temperature sensor. These are inserted to the device shown in the left picture which controls the ambient temperature and conducts the measurements.

The hot-wire method measures the thermal conductivity of the sample by measuring the temperature increase at a defined distance away from a hot wire. This wire is assumed to be an infinitely long and thin cylinder. If the heat source is constant and the sample has uniform properties the thermal conductivity can be directly derived from the measured temperature increase at a known distance from the wire according to:

$$\Delta T(r, t) = \frac{q}{4\pi k} \ln\left(\frac{4\alpha t}{r^2 C}\right). \quad (\text{B.1})$$

In which t is the time, r the radius of the distance between the hot wire and the temperature sensor and C is the exponent of Euler's constant:

$$C = e^g \quad (\text{B.2})$$

$$g = 0.5772157 \quad (\text{B.3})$$

B.1.1. Calibration

Prior to the first test the functionality of the machine is verified using a sample of distilled water. The thermal conductivity of this sample is measured at 20[°C] and is found to be within 5% (measuring error of the machine) of the reference value provided in the manual. Hence validating the proper functionality of the machine.

B.1.2. Measuring procedure

All measurements are done according to the same standard procedure summarized below.

1. **Cleaning** The container is cleaned with ethanol and then flushed with purified water. Finally it is dried with a paper towel to ensure the sample is not contaminated with any residue of previous measurements.
2. **Set temperature** The temperature is set to a fixed temperature and the machine is allowed time for the temperature to stabilize. The temperature is called stable once it deviates no more than 0.1[°C] over 1 minute.
3. **Measurement** The thermal conductivity is measured 20 times, whilst the bulk temperature of the sample is constantly monitored to ensure it still remains within the set limits.
4. **Increase temperature** The temperature of the sample is increased and steps 2 and 3 are repeated.

B.1.3. Analysis

Once the measurements are done the two highest and lowest values are excluded and the average of the remaining 16 measurements is taken as the thermal conductivity. Parallel to the thermal conductivity also the thermal diffusivity of the material is measured. As the density is known also the specific heat can be calculated by means:

$$\alpha = \frac{k}{\rho C_p}, \quad (\text{B.4})$$

where k is the thermal conductivity, ρ the density and C_p the specific heat.

B.2. Solids

Thermal measurements of the solids is done using the C-Therm Tci machine. This machine uses the modified transient plane source method and is only suitable for the measurement of solid samples [5]. The solid samples are placed on a sensor as shown in the right image of Figure B.2 and then placed inside an oven. The oven is used to control the bulk temperature of the sample which is measured by the sensor on which it is placed.

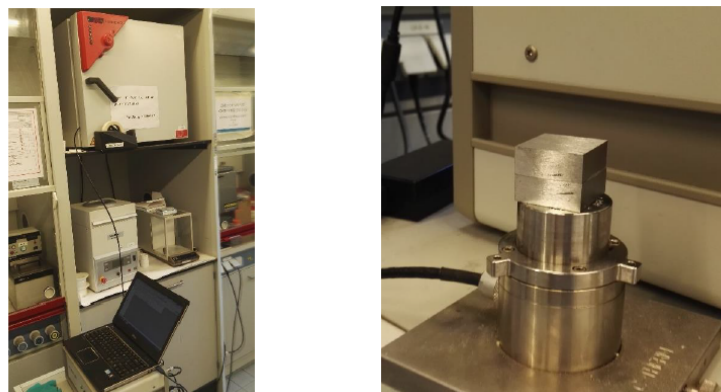


Figure B.2: Setup for the measurement of the thermal conductivity of solids using the modified transient plane source method. The picture on the right shows how two samples have been stacked to obtain one sample with sufficient size.

The modified plane source method uses a spiral heating measurement to apply a short, known and constant heat input to the sample. The change of the voltage over the coil is correlated with the temperature of the

spiral which is in direct contact with the sample. Less thermally conducting materials (for instance plastics) would give a higher temperature at the surface and hence a bigger drop of the voltage over the coil. This drop of the voltage is used to determine the thermal conductivity and effusivity.

B.2.1. Calibration

The machine is calibrated using a perspex sample which is supplied with the machine. The thermal conductivity of the sample is measured at room temperature and compared to the reference value provided by the manufacturer. The value is within the specified range and thus the proper functionality of the machine is verified.

B.2.2. Measuring procedure

The modified transient plane source method requires, a sample which is sufficiently thick so that no heat penetrates all the way through the sample and is lost to the surroundings. For metals the required thickness is around 20[mm]. Samples of the material from the different liners had to be cut from actual liners and which were not available with the required thickness. To overcome this issue, multiple samples are cut and stacked on top of each other to obtain the required thickness. A set of 4 different S355 samples with different amount of layers and heights were used to verify the stacking method.

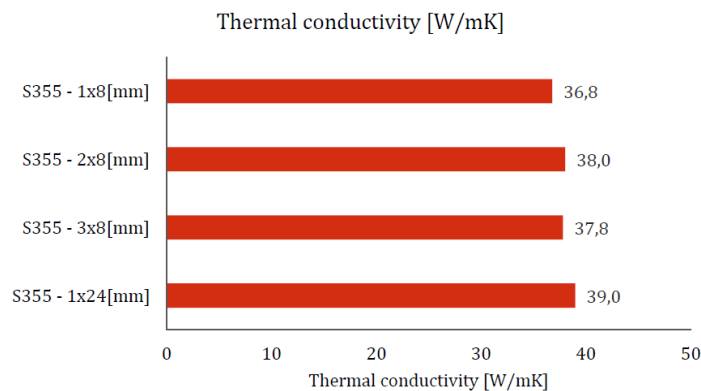


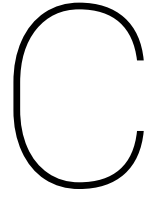
Figure B.3: Verification of the stacking method by means of 4 different S355 samples with different amount of layers and thickness

As can be seen in Figure B.3 the thermal conductivity of the unstacked sample (1x24[mm]) is the highest, the samples with 2 and 3 layers come to within 3% of this value which is an acceptable error. For the measurements of the liner materials 3 layers of 8[mm] are used. Measurement are done according to the procedure described below.

1. **Stacking** If required the sample is stacked using a highly thermal conductive paste between the layers.
2. **Cleaning** The sensor is cleaned with ethanol to remove any residue from previous measurements.
3. **Apply contact agent** The contact agent supplied by the manufacturer of the machine is applied on the sensor and the sample is set on top.
4. **Set temperature** The temperature of the oven is set to a fixed temperature and allowed to stabilize for about 1 hour.
5. **Measurement** The thermal conductivity is measured 10 times.
6. **Increase temperature** The temperature of the sample is increased and steps 4 and 5 are repeated.

B.2.3. Analysis

An average is taken of the 10 measurements to determine the thermal conductivity and effusivity of the material at a specific temperature. Calculation of the specific heat then follows the same procedure as described in Section B.1.3.



Conduction of heat

C.1. Theoretical background

Conduction is the transfer of internal heat by collisions of particles and the movement of electrons on a microscopic scale [26]. Conduction is generally homogeneous in all direction of a single material and proportional to the local gradient of the temperature. Thermal conduction is also referred to as diffusion and occurs spontaneously with only the temperature gradient as the only driving force.

C.2. Analytical approach

The conduction of heat is described by Fourier's law [1] [26] which is (per unit area) given by:

$$.q = k\nabla T \tag{C.1}$$

Where q is the heat flux per unit area, k the thermal conductivity and ∇T the gradient of the temperature. By integrating Fourier's equation over a certain area one arrives at the integral form of Fourier's equation:

$$Q = k \oint \nabla T dA. \tag{C.2}$$

Where Q is the total heat flux. Furthermore the first law of thermodynamics states that:

$$\Delta U = Q - W. \tag{C.3}$$

In which ΔU is the change of internal energy in, Q the external heat input on, and W the work done by any system or body. In other words the first law states that energy is always conserved. For most solids one can assume a (temperature dependent) value for the specific heat, C_p , of the material and thus the internal energy per unit volume of any body is given by:

$$U = \rho C_p T, \tag{C.4}$$

this Equation can be rewritten to equate a temperature increase as a function of the change of internal energy in a system:

$$\Delta T = \frac{\Delta U}{\rho C_p}. \tag{C.5}$$

Inserting Equations C.2 & C.5 in Equation C.3 and assuming that $W = 0$ a differential equation for the temperature increase as a consequence of eat conduction is found:

$$\frac{dT}{dt} = \frac{k \oint \nabla T dA}{\rho C_p}. \tag{C.6}$$

Which can be rewritten in cylindrical coordinates (useful considering the cylindrical nature of the cone and liner) following the cylindrical nature of the system considered:

$$\frac{1}{r} \frac{\delta}{\delta r} \left(kr \frac{\delta T}{\delta r} \right) + \frac{1}{r^2} \frac{\delta}{\delta \theta} \left(k \frac{\delta T}{\delta \theta} \right) + \frac{\delta}{\delta z} \left(k \frac{\delta T}{\delta z} \right) = \rho C_p \frac{\delta T}{\delta t}. \quad (\text{C.7})$$

Where r , θ and z represent the cylindrical coordinates. Next the thermal diffusivity, α is introduced as:

$$\alpha = \frac{k}{\rho C_p}. \quad (\text{C.8})$$

Finally if one assumes axis symmetry and an infinity long cylinder all derivatives of θ and z turn zero and inserts Equation C.8 you find the simplified differential equation for axis symmetric heat conduction:

$$\frac{1}{r} \frac{\delta}{\delta r} \left(r \frac{\delta T}{\delta r} \right) = \frac{1}{\alpha} \frac{\delta T}{\delta t}. \quad (\text{C.9})$$

This differential equation can be solved using the method of separation of variables so that we find:

$$T(r, t) = \frac{2T_s}{b} \sum_{n=1}^{\infty} \frac{J_0(\lambda_n r)}{\lambda_n J_1(\lambda_n b)} e^{-\alpha \lambda_n^2 t}, \quad (\text{C.10})$$

which is based on Bessel functions, J_n , and zero's, λ_n , of the n -th order [34]. Now a simplified test geometry is introduced which can be solved with the equation above. Results from this analytical calculation can later be used to verify a numerical model. The simplified geometry is shown in Figure C.1

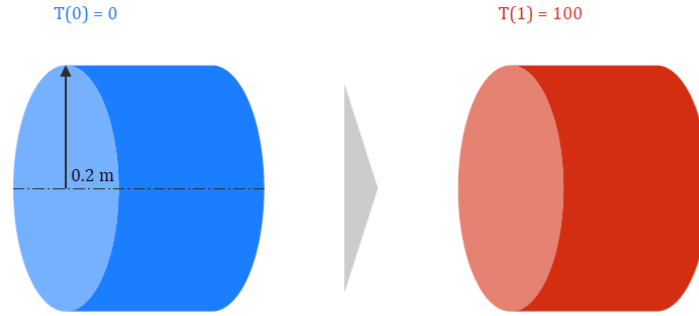


Figure C.1: Setup of the test calculation to verify Analytical method. The setup is based on a cylinder with a radius of 0.2[m], initially at $T = 0[^\circ\text{C}]$ everywhere. Then the outer surface temperature is set to $T = 100[^\circ\text{C}]$ and the radial temperature distribution is analyzed.

For the verification calculation the test cylinder is chosen to be at a uniform temperature of $T = 0[^\circ\text{C}]$ at $t = 0[\text{s}]$. At any time after that the outer boundary of the system is set to $T = 100[^\circ\text{C}]$ and the heating of the cylinder with respect to the radial coordinate and the time is analyzed. Furthermore for the sake of simplicity all the properties of the cylinder are assumed to be independent of the temperature.

Two even further simplified methods are first used to get an estimate for the order of magnitude Temperatures to be expected. The first method is known as the "Heat penetration theorem" (equation C.11 this theorem gives the expected depth heat will penetrate (Δx) within a certain time (t) dependent on the thermal diffusivity (α) of the material. The heat penetration theorem is intended for application in a semi-infinite body as in our case the cylinder is heated from two sides, the theorem will only be valid for short time scales (where there is no interference from heating of the other side).

$$\Delta x = \sqrt{\pi \alpha t} \quad (\text{C.11})$$

The second simplified method comes from Mills, it gives the expected centerline temperature of an infinitely long object when the outer surface is set a constant temperature [1]:

$$T_c = T_o \left(1 - A_1 e^{-\lambda^2 F_o} \right). \quad (\text{C.12})$$

Here T_c is the centerline temperature and T_o is the surface temperature of the object. The shape factors (A_1 & λ) have to be selected based on the Biot number,

$$Bi = \frac{h_c L}{k}, \tag{C.13}$$

and the corresponding shape. For the fixed temperature boundary condition the Biot number is equal to infinity so that the shape factors are given by Table C.1. This method is only valid for longer timescales where $Fo > 0.2$,

$$Fo = \frac{\alpha t}{R^2}, \tag{C.14}$$

where R is the radius of the cylinder and t the time. In the Figure C.2 it can be seen that at every time the simplified analytical solutions match the full analytical solution thus providing a good reference case to which the numerical model can be verified.

Table C.1: Shape factors for Mills long time solution [1]

Shape	$ \lambda $	$ A_1 $
Slab	2.467	1.273
Cylinder	5.784	1.602
Sphere	9.869	2.000

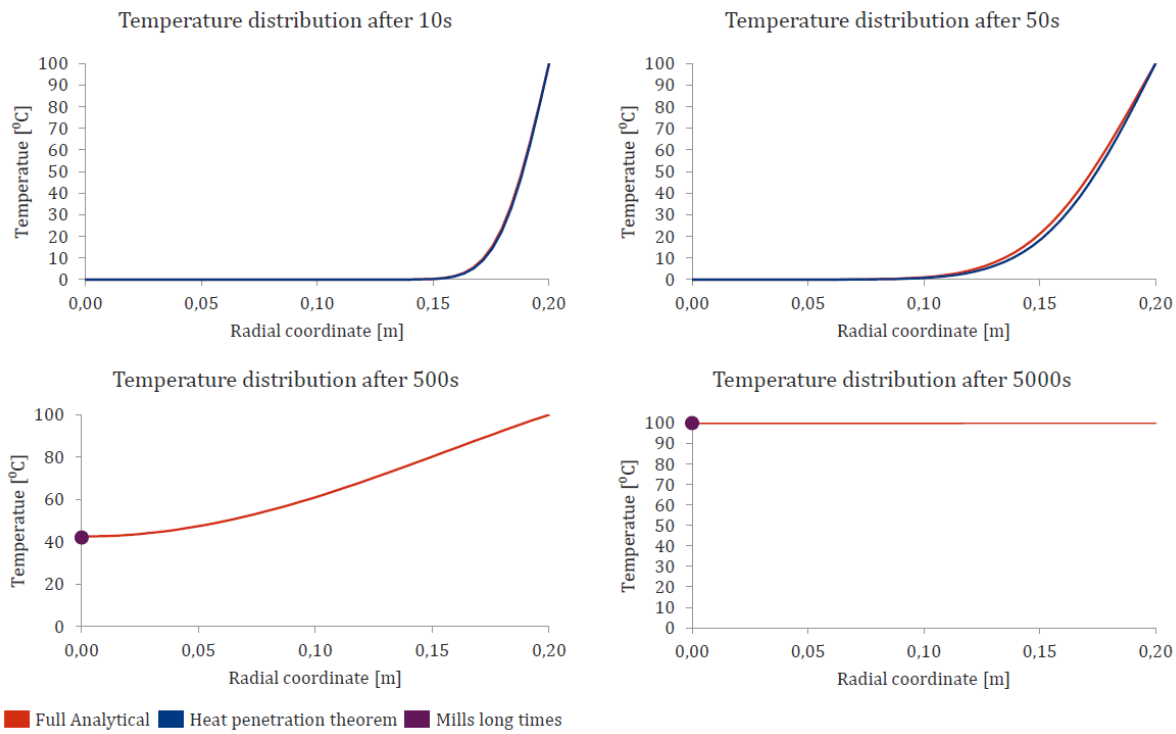


Figure C.2: The temperature distribution along the r -coordinate of the test calculations is shown at four different moments in time. The full analytical solution shows a good match with the simplified methods with their ranges of validity.

D

Model flowchart

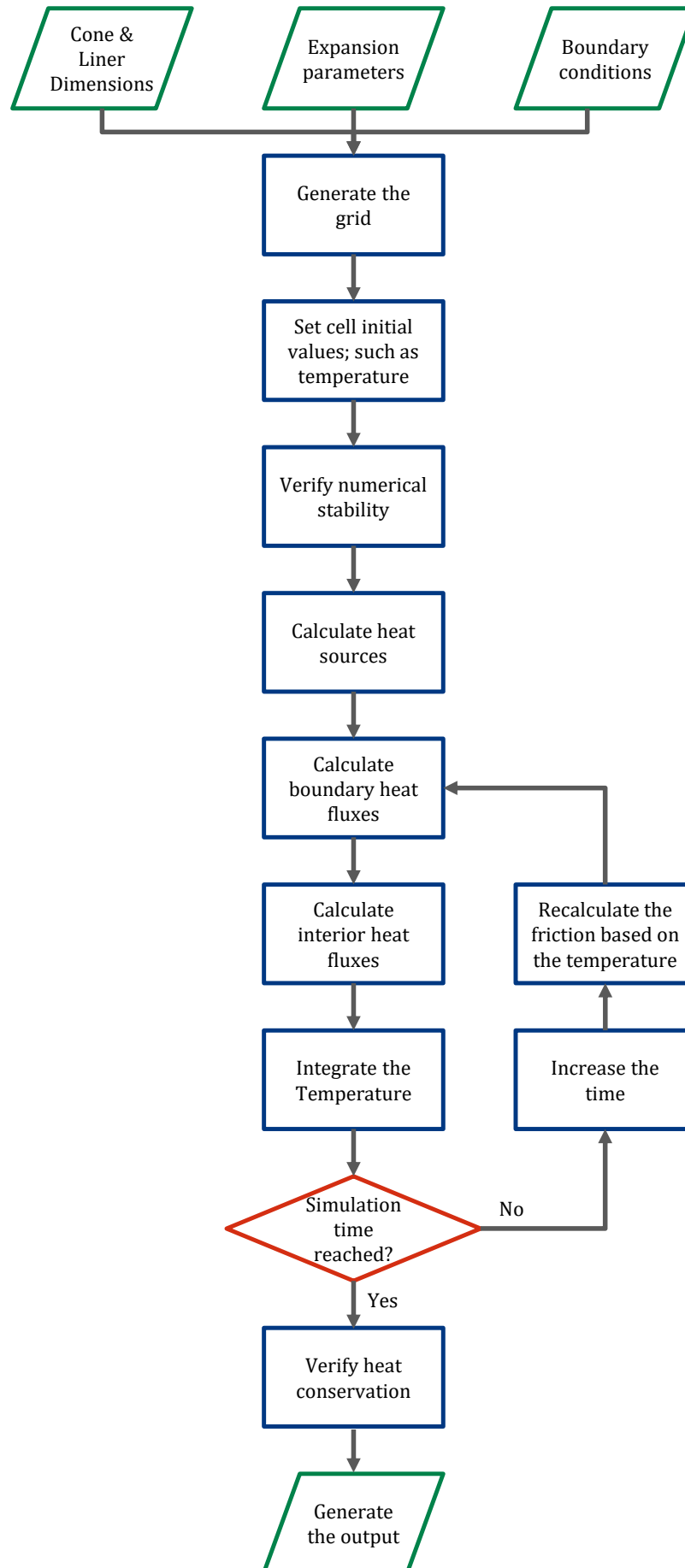


Figure D.1: High-level flowchart of the numerical heat transfer model. Input and Output is shown in green, processing steps in blue and choices in red.

Thermal resistance models

Thermal resistance models are used to derive an estimate for the relative thermal effect of a specific component or layer. A thermal resistance model works by considering obstruction of the component to the flow of heat as electrical resistors, placed either in series or in parallel [1]. When several thermal resistances are positioned in series, for example during conduction through consecutive materials as illustrated in the top of Figure E.1, the total resistance, R , of the system is calculated as:

$$R_{tot} = R_A + R_B, \quad (\text{E.1})$$

in this specific case, the total resistance (101) is nearly equal to the resistance of resistance A (100) and the smaller resistance B (1) could be ignored. When the resistances are placed in parallel, as in the bottom of Figure E.1 for example during conduction and convection from a solid to a liquid, the total resistance is calculated as:

$$R_{tot} = \frac{1}{\frac{1}{R_A} + \frac{1}{R_B}} = \frac{R_A R_B}{R_A + R_B}. \quad (\text{E.2})$$

The parallel thermal resistance is calculated as 1.01, now resistance A can be ignored

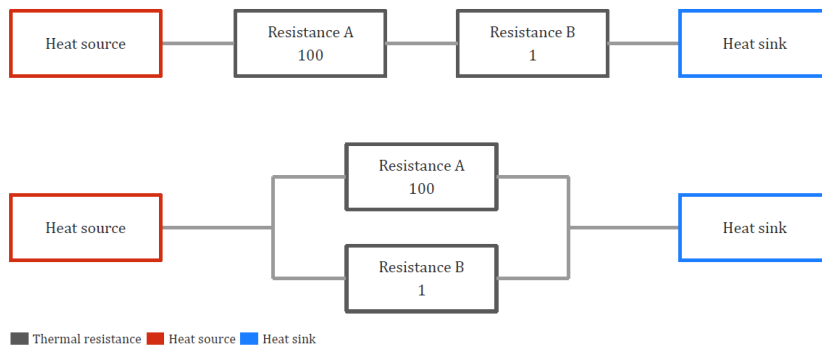


Figure E.1: Schematic of thermal resistance model, top in series and bottom in parallel

For each form of heat transfer the thermal resistance can be calculated. The thermal resistance from conduction is given by;

$$R_{cond} = \frac{L}{kA}, \quad (\text{E.3})$$

in which L is the length over which the heat is transferred, k the thermal conductivity and A the area normal to the heat transfer. The thermal resistance of convection is given by;

$$R_{conv} = \frac{1}{hA} = \frac{D_h}{Nu k}, \quad (\text{E.4})$$

in which h is the convective heat transfer coefficient, D_h the hydraulic diameter and Nu the Nusselt number. Finally, the thermal resistance due of radiation is given by;

$$R_{rad} = \frac{\epsilon \sigma}{A} \frac{T_h^4 - T_c^4}{T_h - T_c}, \quad (\text{E.5})$$

in which ϵ is the radiative emissivity, σ Stefan-Boltzmanns constant, T_h the high temperature and T_c the cold temperature.

F

Split cone design

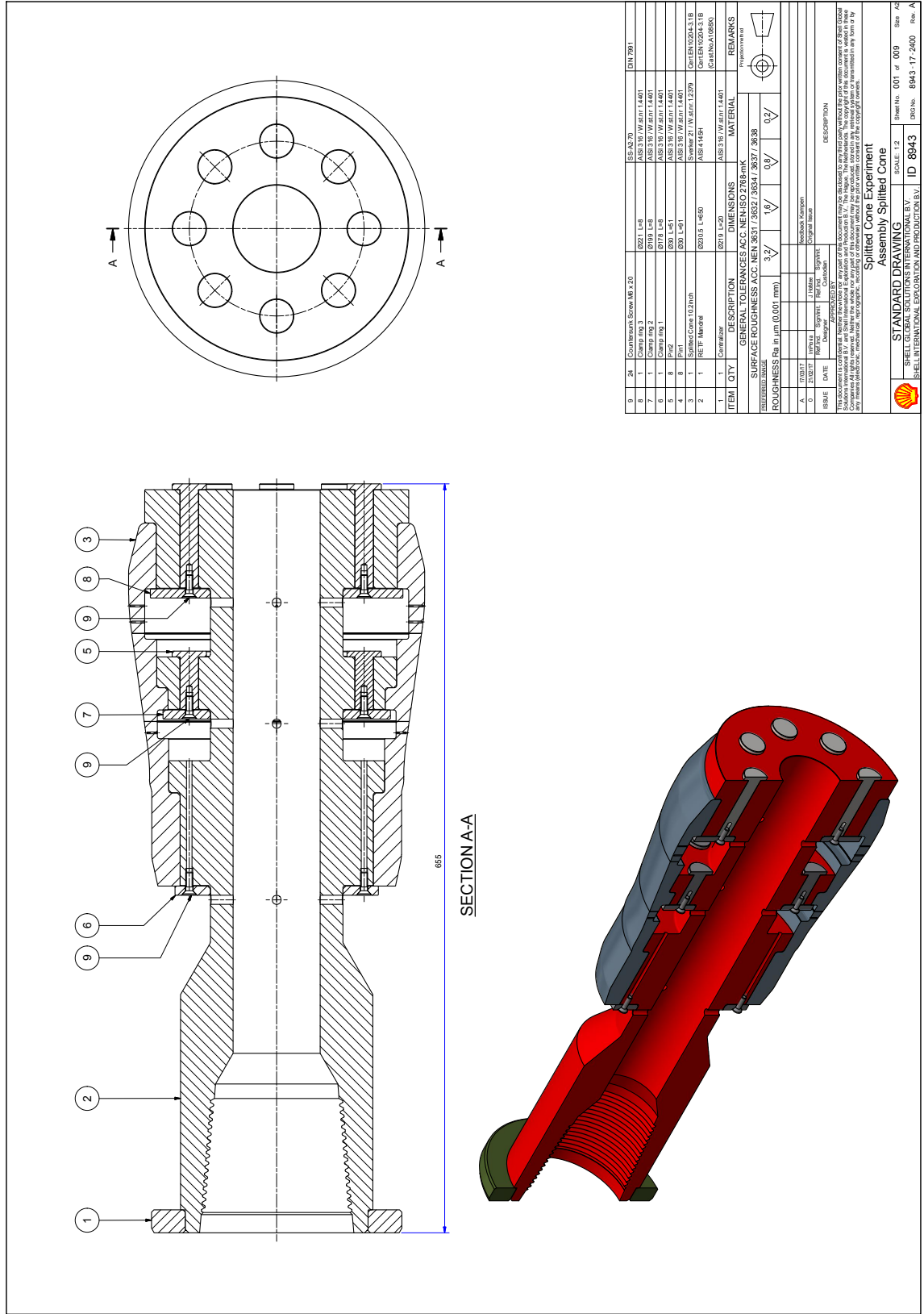


Figure F.1: Design of the cone body (in red) for the split cone test. The locations for the strain gages can also be seen where material has been removed from the body.

FILENAME: 8943-17-2400-001.dwg

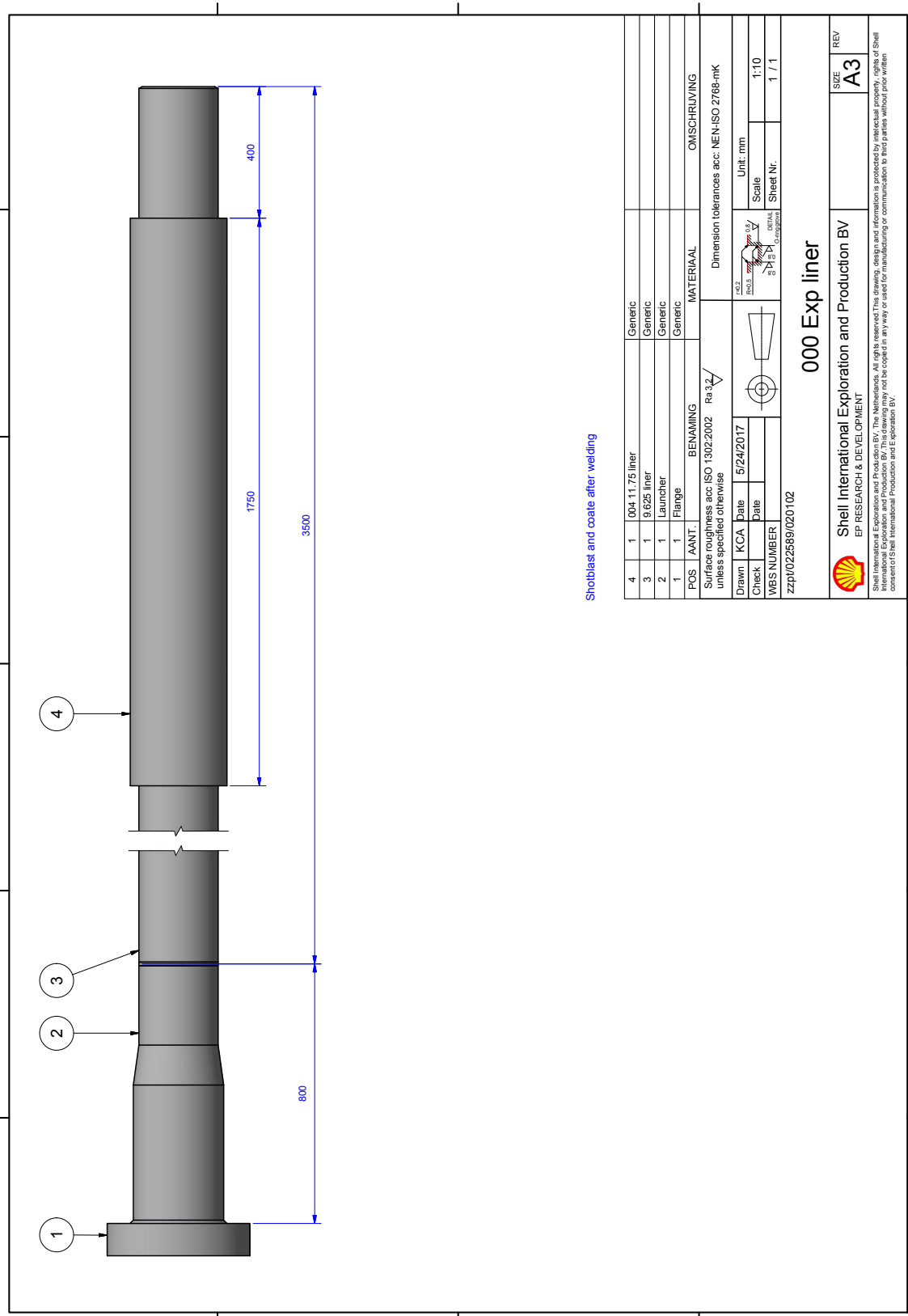


Figure E3: Design of the liner for the split cone test. The liner consists of 2 different casing section, a single liner and overlap section.

G

Thermal cone design

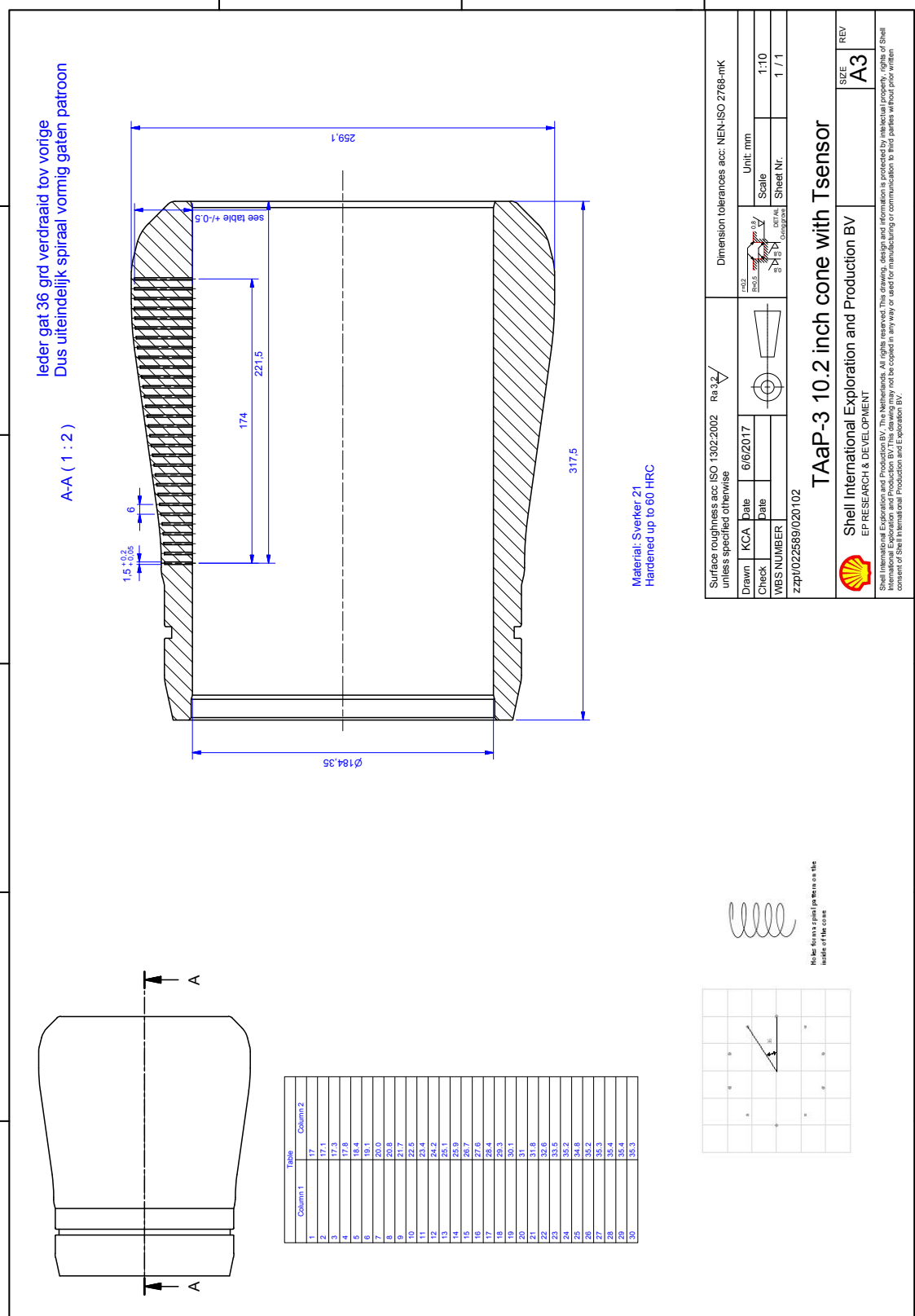


Figure G.1: Design of the cone for the thermal cone test, showing the location and depth of the holes for the thermocouples.

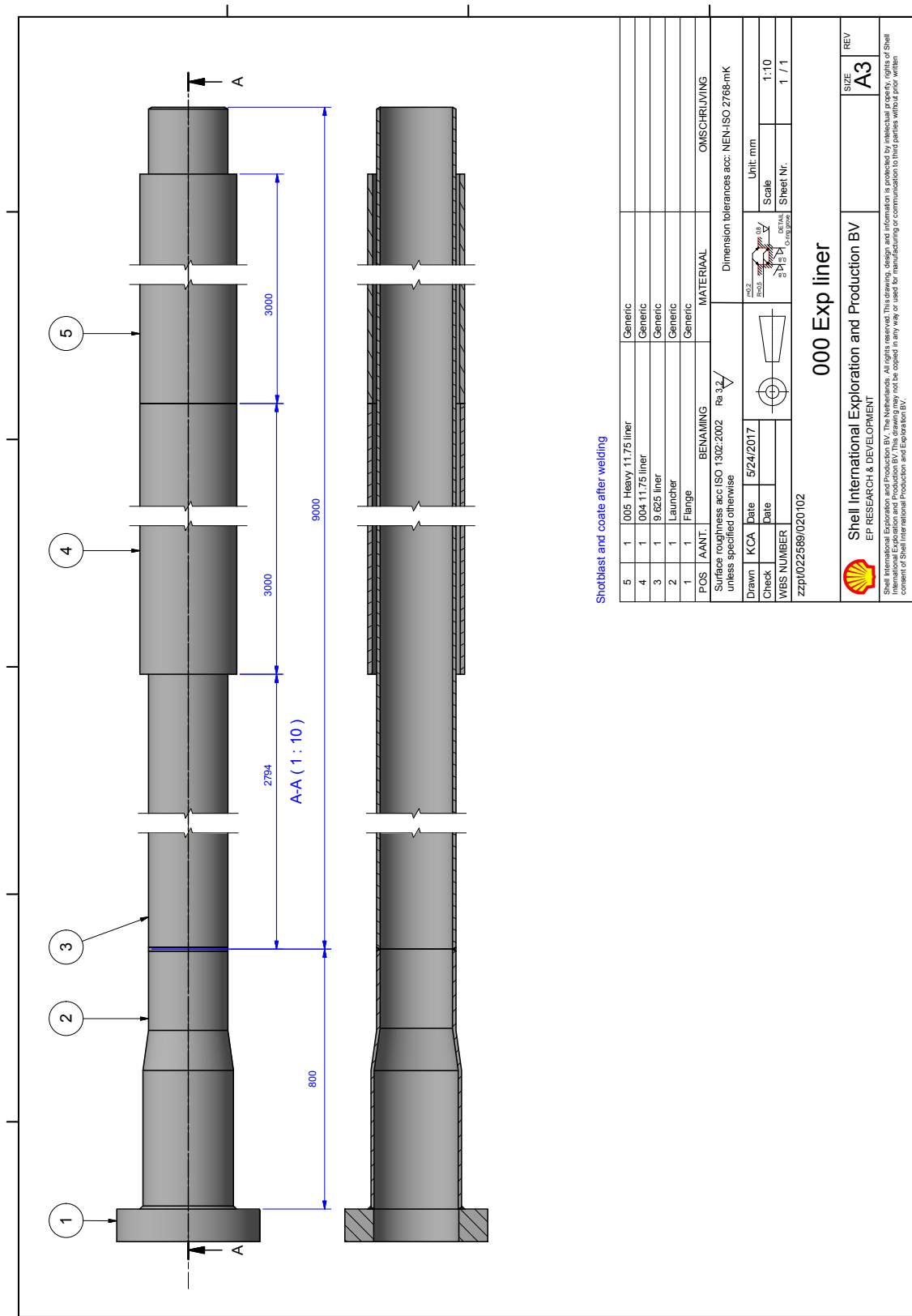


Figure G.2: Design of the liner for the thermal cone test. The liner consists of 3 segments, a single liner, overlap and heavy overlap section.



Full results thermal cone

H.1. Single liner expansion

Table H.1: Expansion parameters during single liner expansion

Parameter	value	unit
Peak expansion force	1110	kN
Steady state expansion force	1063	kN
Expansion speed	25.75	mm/s
Temperature increase liner	25.5	°C
Section length	2560	mm
Shortening	128.6	mm

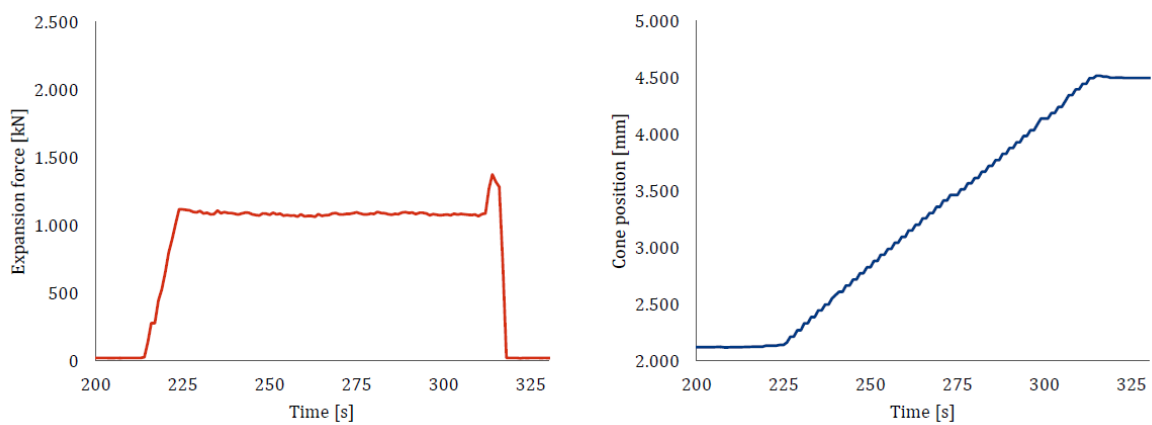
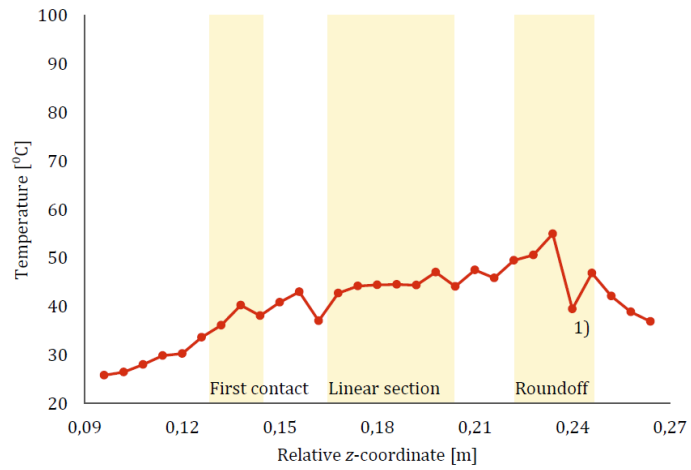


Figure H.1: Expansion force and cone displacement during single liner expansion



1) Thermocouple most likely malfunctioned

Figure H.2: Steady state temperatures inside the cone during single liner expansion

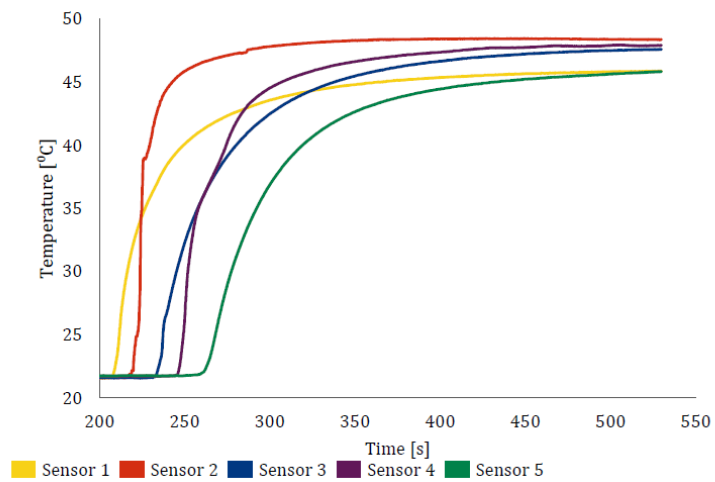


Figure H.3: Transient temperature development on the outside of the liner during single liner expansion

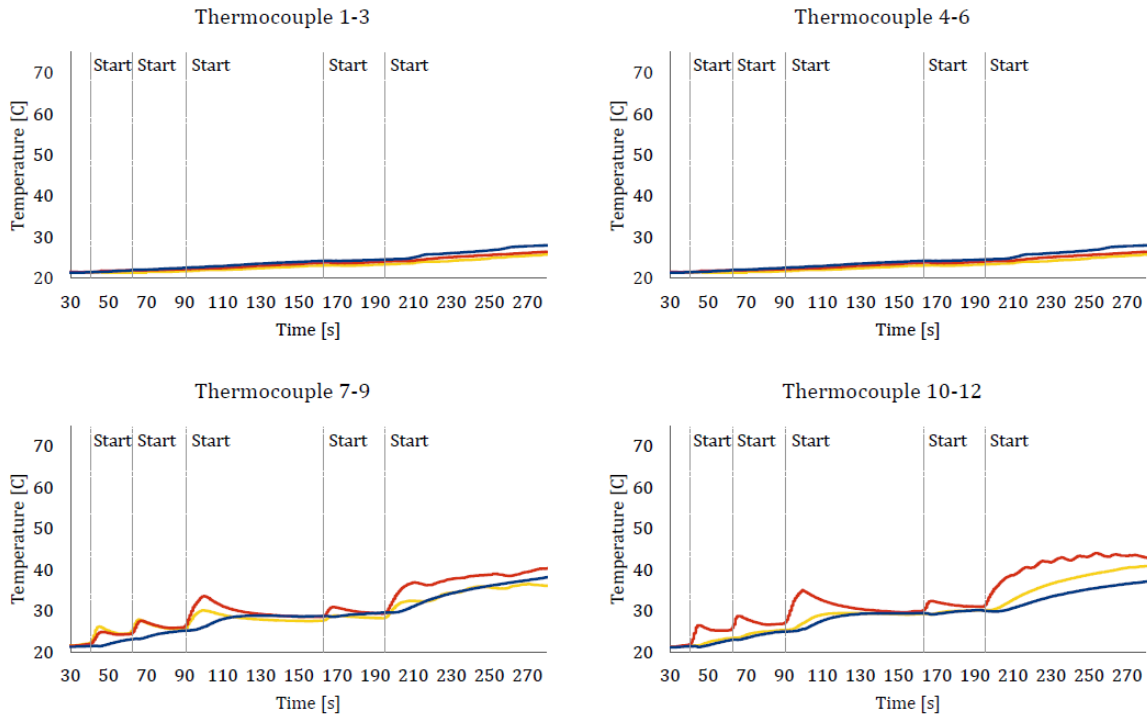


Figure H.4: Results from cone thermocouples 1-12 of the single liner expansion. For each graph the first thermocouple is represented by the yellow line, the second by the red line and the third by the blue line.

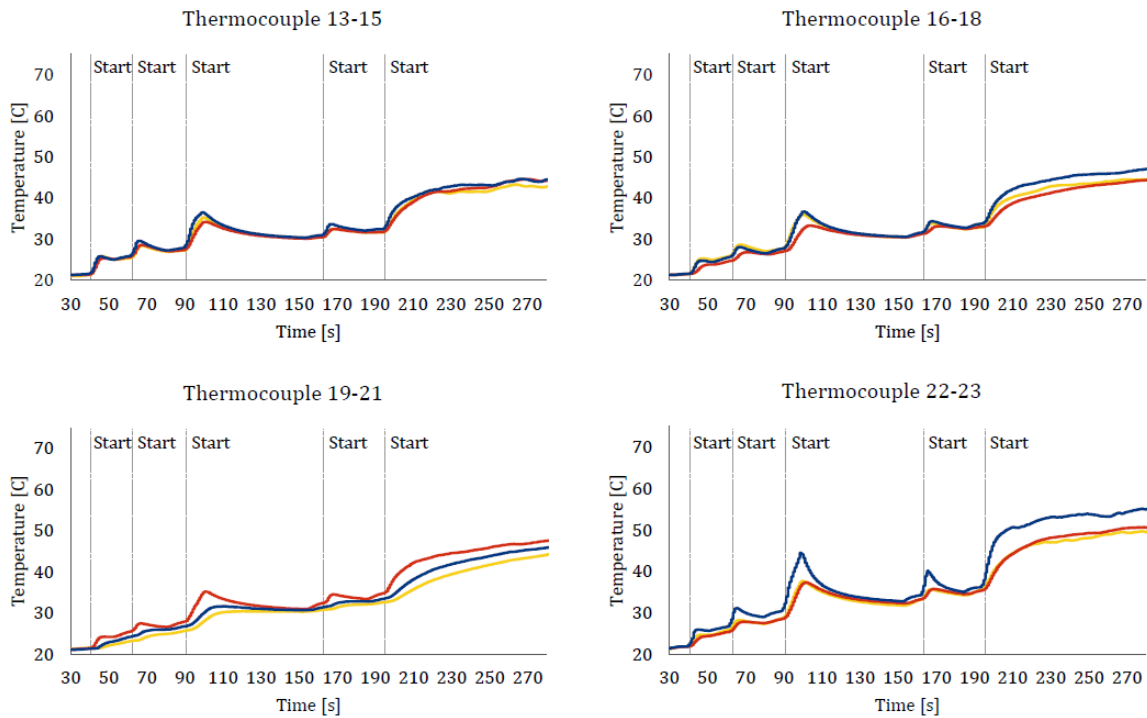


Figure H.5: Results from cone thermocouples 13-24 of the single liner expansion. For each graph the first thermocouple is represented by the yellow line, the second by the red line and the third by the blue line.

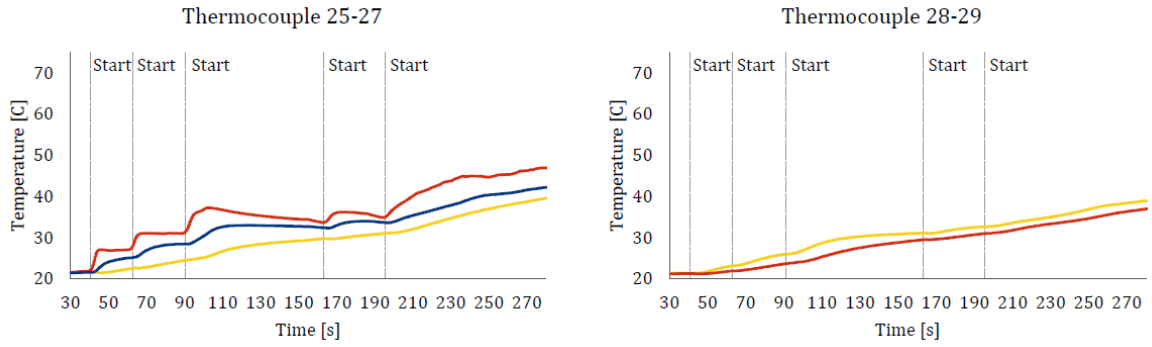


Figure H.6: Results from cone thermocouples 25-29 of the single liner expansion. For each graph the first thermocouple is represented by the yellow line, the second by the red line and the third by the blue line.

H.2. Overlap expansion

Table H.2: Expansion parameters during overlap expansion

Parameter	value	unit
Peak expansion force	1892	kN
Steady state expansion force	1692	kN
Expansion speed	26.15	mm/s
Temperature increase liner	18.0	°C
Section length	3000	mm
Shortening	44.14	mm

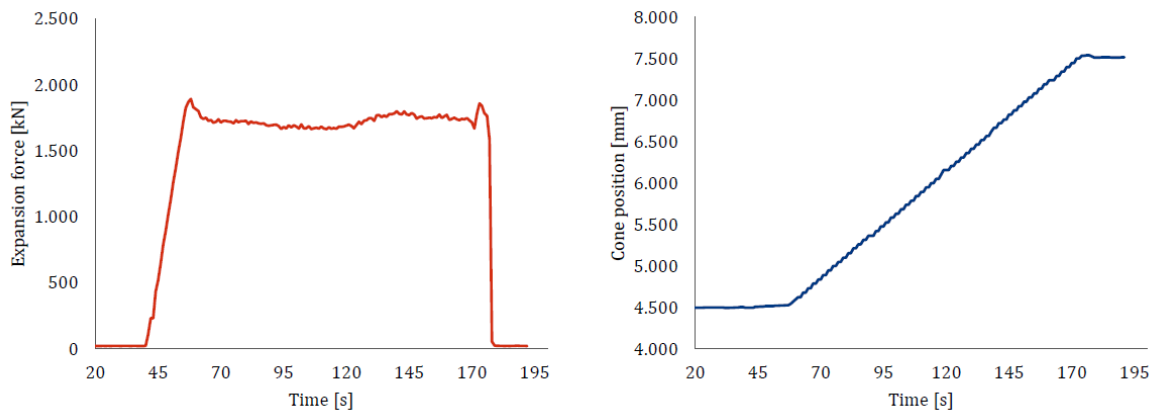
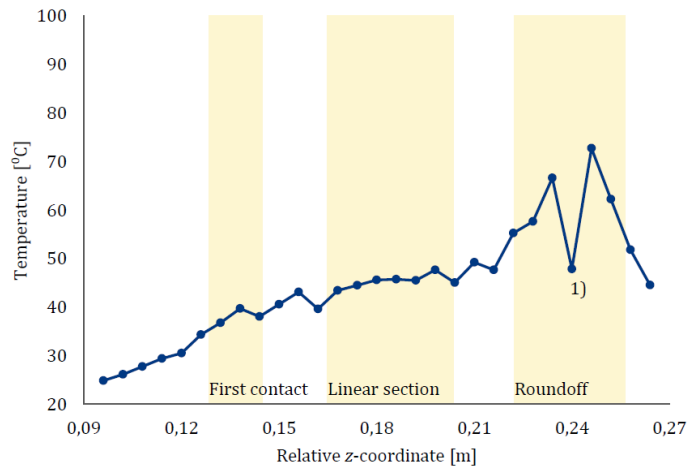


Figure H.7: Expansion force and cone displacement during overlap expansion



1) Thermocouple most likely malfunctioned

Figure H.8: Steady state temperatures inside the cone during overlap expansion

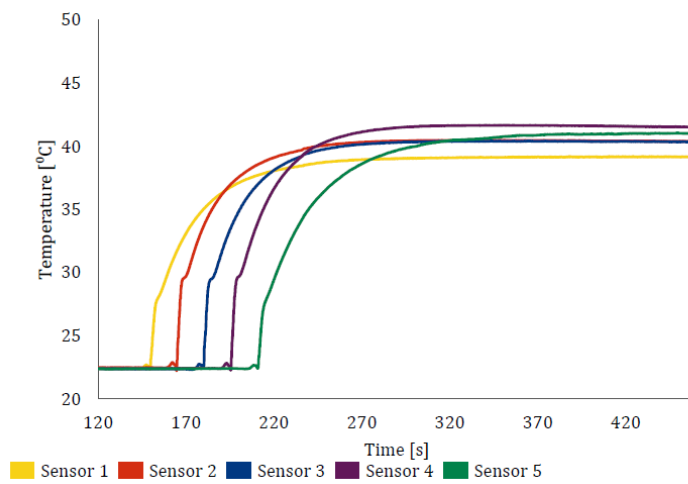


Figure H.9: Transient temperature development on the outside of the liner during overlap expansion

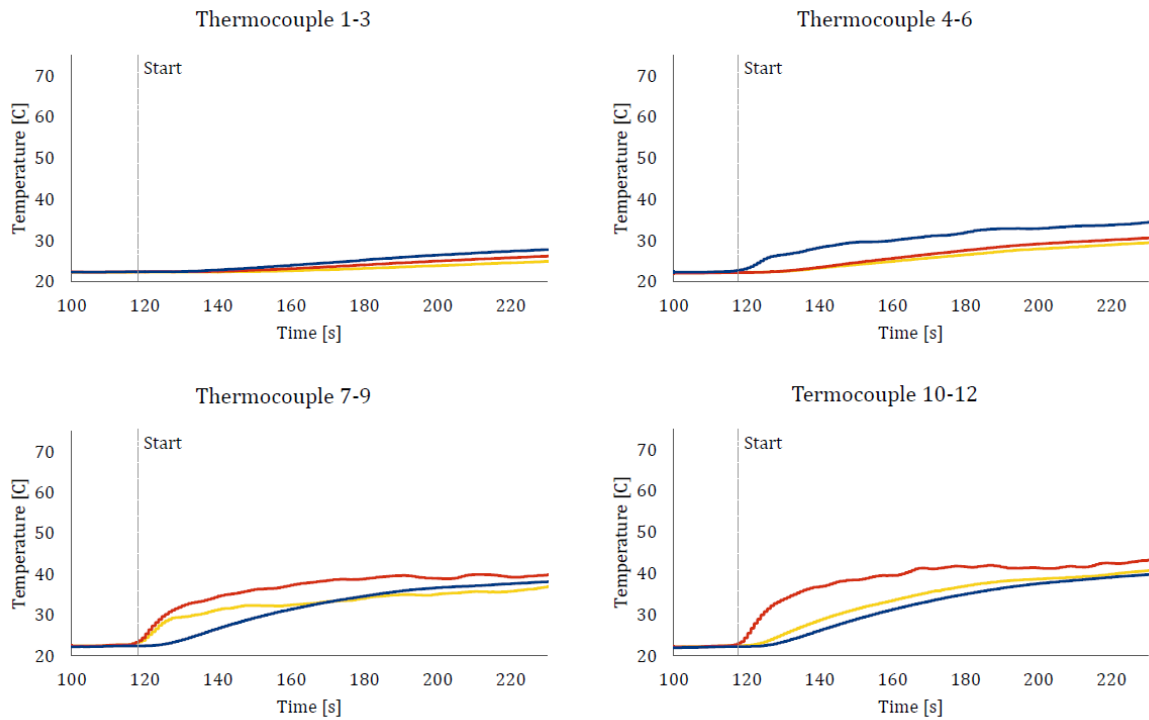


Figure H.10: Results from cone thermocouples 1-12 of the overlap expansion. For each graph the first thermocouple is represented by the yellow line, the second by the red line and the third by the blue line.

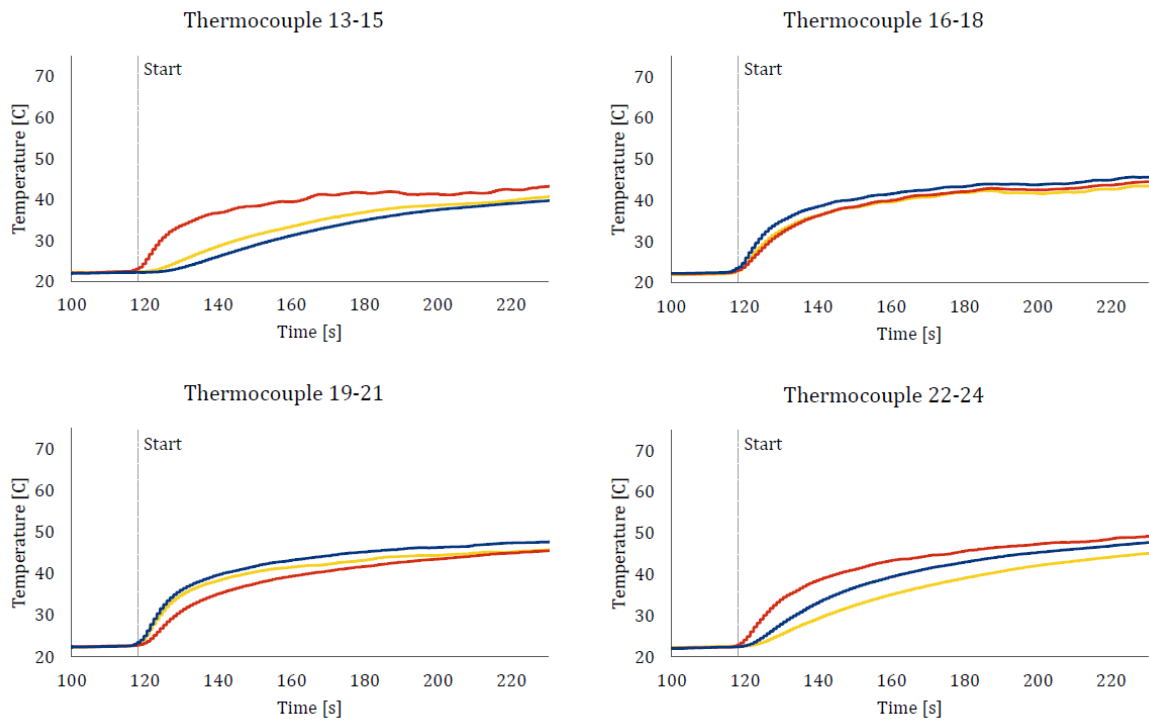


Figure H.11: Results from cone thermocouples 13-24 of the overlap expansion. For each graph the first thermocouple is represented by the yellow line, the second by the red line and the third by the blue line.

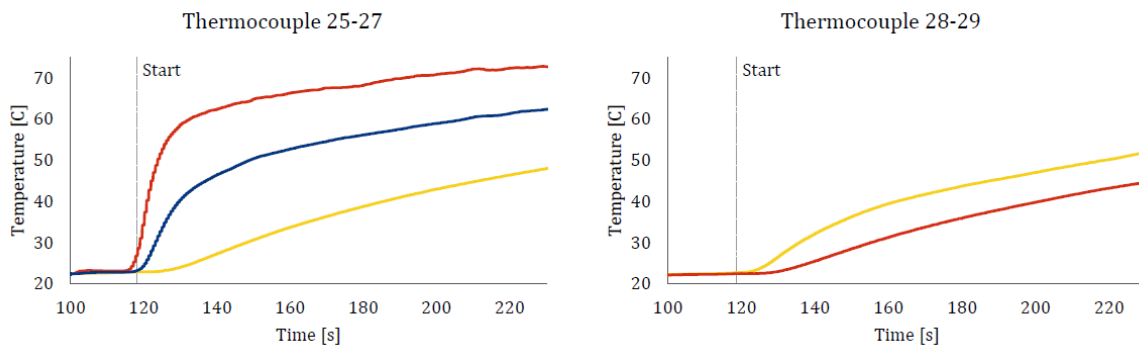


Figure H.12: Results from cone thermocouples 25-29 of the overlap expansion. For each graph the first thermocouple is represented by the yellow line, the second by the red line and the third by the blue line.

H.3. Heavy overlap expansion

Table H.3: Expansion parameters during heavy overlap expansion

Parameter	value	unit
Peak expansion force	2410	kN
Steady state expansion force	2100	kN
Expansion speed	22.55	mm/s
Temperature increase liner	21.1	°C
Section length	2940	mm
Shortening	54.53	mm

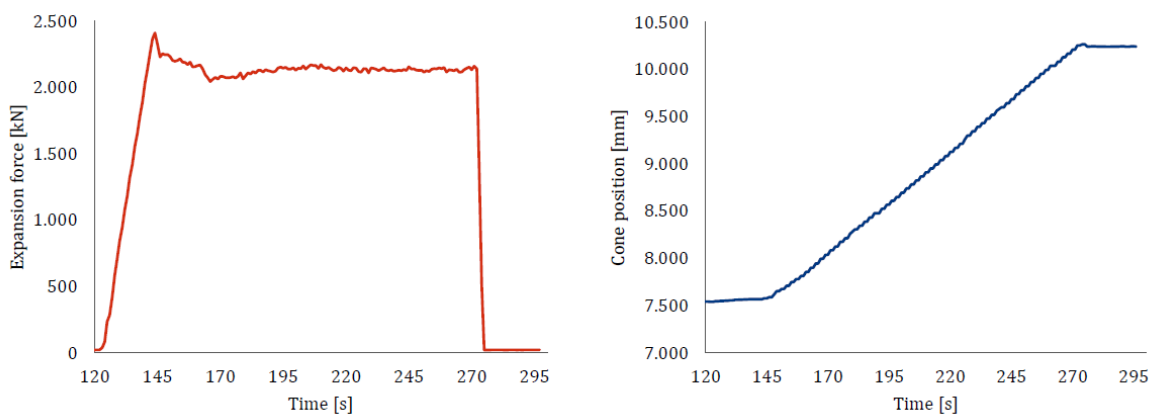
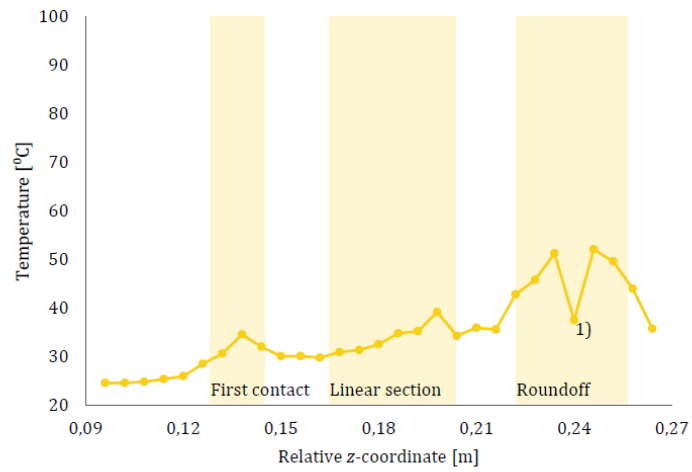


Figure H.13: Expansion force and cone displacement during heavy overlap expansion



1) Thermocouple most likely malfunctioned

Figure H.14: Steady state temperatures inside the cone during heavy overlap expansion

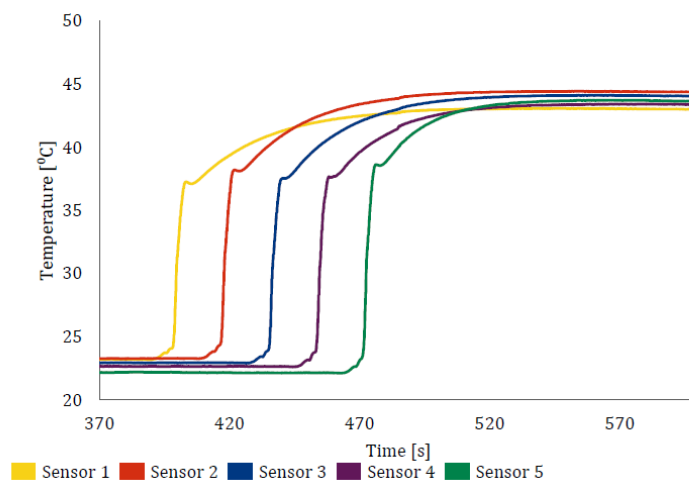


Figure H.15: Transient temperature development on the outside of the liner during heavy overlap expansion

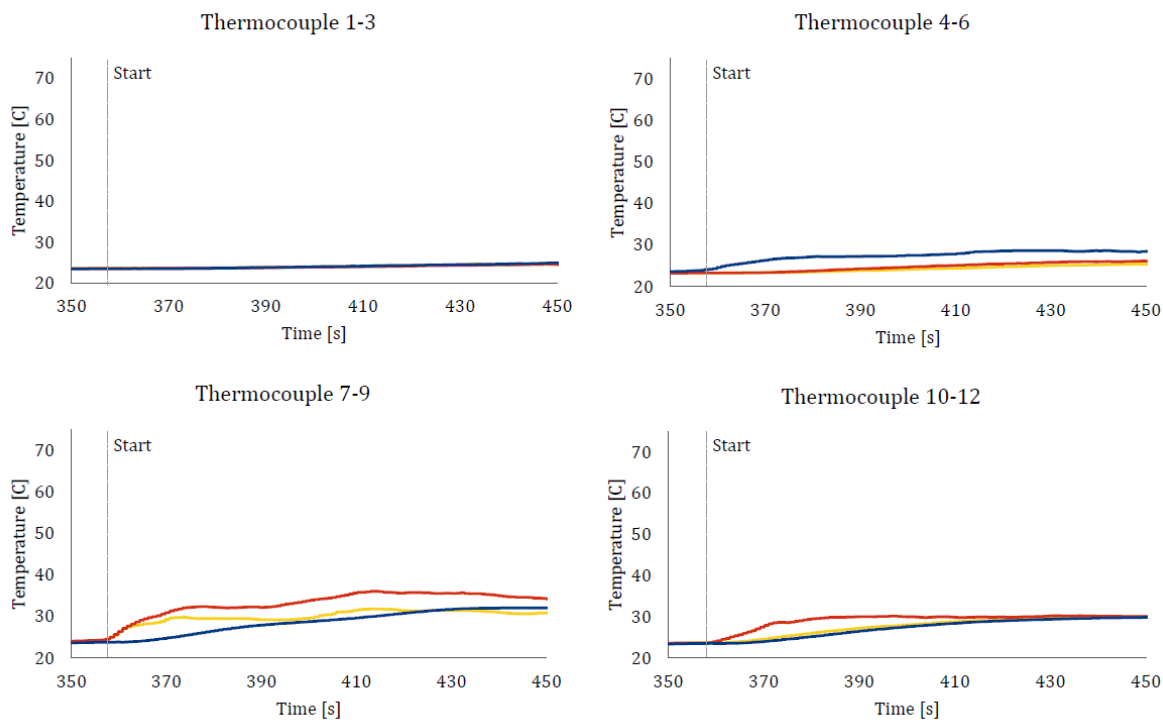


Figure H.16: Results from cone thermocouples 1-12 of the heavy overlap expansion. For each graph the first thermocouple is represented by the yellow line, the second by the red line and the third by the blue line.

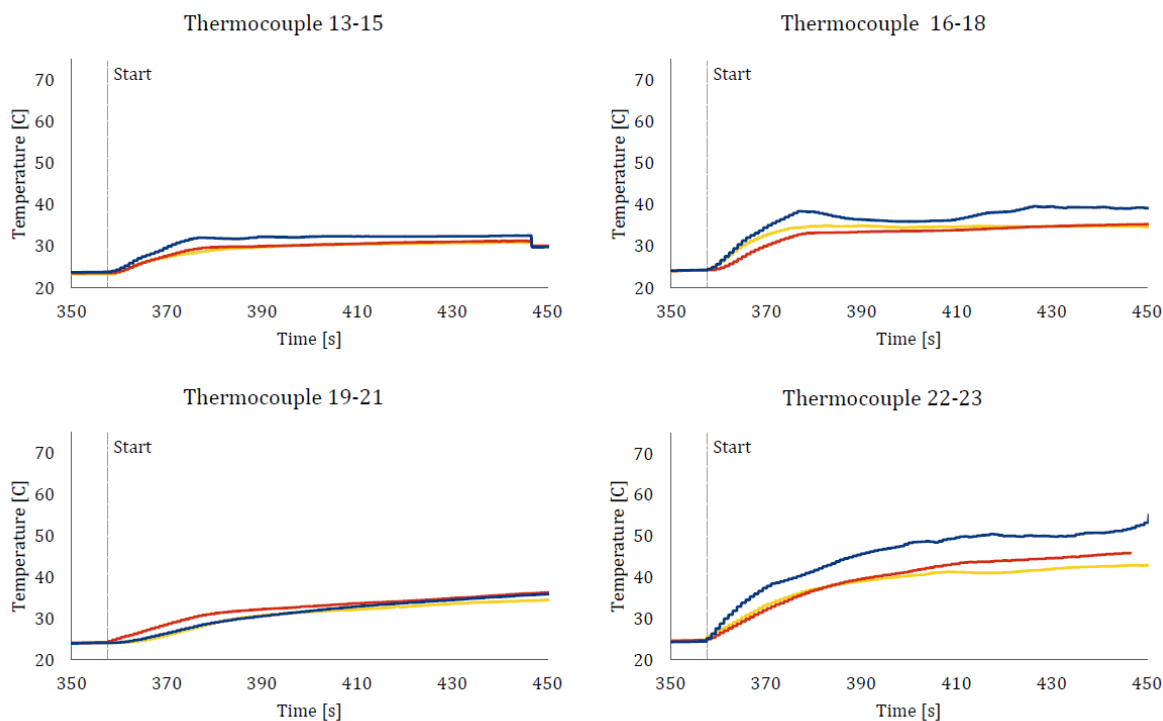


Figure H.17: Results from cone thermocouples 13-24 of the heavy overlap expansion. For each graph the first thermocouple is represented by the yellow line, the second by the red line and the third by the blue line.

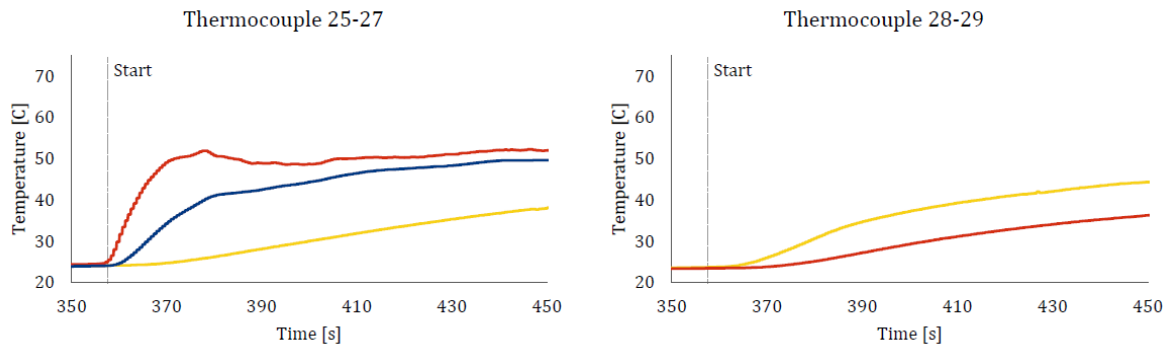


Figure H.18: Results from cone thermocouples 25-29 of the heavy overlap expansion. For each graph the first thermocouple is represented by the yellow line, the second by the red line and the third by the blue line.



Base case

Table I.1: Expansion parameters

Parameter	Value	Unit
Expansion speed	0.1	$\frac{m}{s}$
Down hole temperature	80	$^{\circ}C$
Expansion mode	Tension	-
Cone type	10.2" TAap_3	-
Liner type	VM50 OD $9\frac{5}{8}$, wall 0.435	inch
Overlap type	P110 OD $11\frac{3}{4}$, wall 0.54	inch

Table I.2: Boundary conditions

Boundary	Type	Value
Contact	Conduction & heat source	
Liner North	Isolated	
Liner East	Convective term	
Liner West	Convective term	
Liner South	Isolated	
Cone East	Convection	$h = 954$
Cone West	Isolated	
Cone South	Conduction & Convection	$h = 954$

The simplified dimensions shown in Tables I.3 to I.5 are used to model the cone, liner and the overlap liner in the numerical model.

Table I.3: Cone dimensions

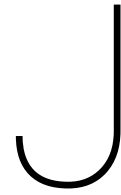
Dimension	Description	Value [m]
r_{in}	Cone inner radius	0.0922
r_{maxA}	Front straight section outer radius	0.1092
r_{cutA}	Radius reduction at front outer chamfer	0.0050
r_{maxC}	Maximum outer radius of the cone	0.1296
r_{cutE}	Outer radius at the rear of the cone	0.1073
L_A	Length of section A	0.0275
L_B	Length of section B	0.0551
L_C	Length of section C	0.1720
L_D	Length of section D	0.0372
L_E	Length of section E	0.0258

Table I.4: Liner dimensions

Dimension	Description	Value [m]
r_{in}	Initial liner inner radius	0.11049
t	Initial thickness of the liner	0.01105
L	Length of a casing section	12.192

Table I.5: Overlap casing dimensions

Dimension	Description	Value [m]
r_{in}	Initial liner inner radius	0.13551
t	Initial thickness of the liner	0.01372
L	Length of a casing section	12.192



Test case

Table J.1: Expansion parameters

Parameter	Value	Unit
Expansion speed	0.02 / 0.025	$\frac{m}{s}$
Ambient temperature	22	$^{\circ}C$
Expansion mode	Tension	-
Cone type	10.2" TAap_3	-
Liner type	VM50 OD $9\frac{5}{8}$, wall 0.435	inch
Overlap type	P110 OD $11\frac{3}{4}$, wall 0.54	inch

Table J.2: Boundary conditions

Boundary	Type	Value
Contact	Conduction & heat source	
Liner North	Isolated	
Liner East	Convective term	
Liner West	Convective term	
Liner South	Isolated	
Cone East	Isolated	
Cone West	Isolated	
Cone South	Isolated	

The simplified dimensions shown in Tables J.3 to J.5 are used to model the cone, liner and the overlap liner in the numerical model.

Table J.3: Cone dimensions

Dimension	Description	Value [m]
r_{in}	Cone inner radius	0.0922
r_{maxA}	Front straight section outer radius	0.1092
r_{cutA}	Radius reduction at front outer chamfer	0.0050
r_{maxC}	Maximum outer radius of the cone	0.1296
r_{cutE}	Outer radius at the rear of the cone	0.1073
L_A	Length of section A	0.0275
L_B	Length of section B	0.0551
L_C	Length of section C	0.1720
L_D	Length of section D	0.0372
L_E	Length of section E	0.0258

Table J.4: Liner dimensions

Dimension	Description	Value [m]
r_{in}	Initial liner inner radius	0.11049
t	Initial thickness of the liner	0.01105
L	Length of a casing section	12.192

Table J.5: Overlap casing dimensions

Dimension	Description	Value [m]
r_{in}	Initial liner inner radius	0.13551
t	Initial thickness of the liner	0.01372
L	Length of a casing section	12.192

Bibliography

- [1] A.F. Mills. *Basic Heat Mass Transfer*. Pearson Education (Us), second edition, 1998. ISBN 9780130962478.
- [2] O. S. Al-abri and T. Pervez. Structural behavior of solid expandable tubular undergoes radial expansion process – Analytical, numerical, and experimental approaches. *International Journal of Solids and Structures*, 50(19):2980–2994, 2013. ISSN 0020-7683. doi: 10.1016/j.ijsolstr.2013.05.013.
- [3] M. F. Ashby, J. Abulawi, and H. S. Kong. Temperature Maps for Frictional Heating in Dry Sliding. *Tribology Transactions*, 34(June 2015):577–587, 1991. ISSN 1040-2004. doi: 10.1080/10402009108982074.
- [4] ASTM International. ASTM D2717-95(2009), Standard Test Method for Thermal Conductivity of Liquids, 2009. URL www.astm.org.
- [5] ASTM International. ASTM D7984-16, Standard Test Method for Measurement of Thermal Effusivity of Fabrics Using a Modified Transient Plane Source (MTPS) Instrument, 2016. URL www.astm.org.
- [6] ASTM International. ASTM G133-05(2016), Standard Test Method for Linearly Reciprocating Ball-on-Flat Sliding Wear, 2016. URL www.astm.org.
- [7] C. Brinkhuis. *A study to the lubrication expansion processes for high temperature wells*. Msc. thesis, Universiteit Twente, 2016.
- [8] D. Campo, C. Willieam, A. Filippov, L. Cook, D. Brisco, B. Dean, and L. Ring. Monodiamerer drilling liner - from concept to reality. In *SPE/IADC 79790*, page 15, 2003.
- [9] A. M. Crowell, A. T. Ochsner, and W. Gosnold. Correcting Bottom-Hole Temperatures in the Denver Basin : Colorado and Nebraska. *GRC Transactions*, 36:201–206, 2012.
- [10] D. Di Crescenzo, D. Ernens, M. M. Shuster, and D. H. Zijsling. Lubricant selection for expandable tubular applications A tribological system optimization. Technical report, 2012.
- [11] K. Dupal, D. B. Campo, C. J. Andrews, L. Cook, L. Ring, and P. L. York. Realization of the MonoDiameter Well : Evolution of a Game-Changing Technology. In *Offshore Technology conference*, number Id, 2002.
- [12] Z. B. Hou and R. Komanduri. General solutions for stationary/moving plane heat source problems in manufacturing and tribology. *International Journal of Heat and Mass Transfer*, 43(10):1679–1698, 2000. ISSN 00179310. doi: 10.1016/S0017-9310(99)00271-9.
- [13] T.J.R. Hughes, L.P. Franca, and G.M. Hulbert. A New finite element formulation for computational fluid dynamics: VIII. The Galerkin/least-squares method for advective-diffusive equations. *Computer Methods in Applied Mechanics and Engineering*, 73:173–189, 1989.
- [14] J.C. Jaeger. Moving sources of heat and the temperature at sliding contacts. *Proceedings of the Royal Society of New South Wales*, 76:203–224, 1942.
- [15] A. Jameson, W. Schmidt, and E. Turkel. Numerical Solution of the Euler Equations by Finite Volume Methods Using Runge-Kutta Time Stepping Schemes Numerical Solution of the Euler Equations by Finite Volume Methods Using Runge-Kutta Time-Stepping Schemes. *AIAA*, M(July), 1981. doi: 10.2514/6.1981-1259.
- [16] A. Karrech and A. Seibi. Technology Analytical model for the expansion of tubes under tension. *Journal of Materials Processing*, 210:356–362, 2010. doi: 10.1016/j.jmatprotec.2009.09.024.
- [17] C. Kim. An analytical solution to heat conduction with a moving heat source. *Journal of Mechanical Science and Technology*, 25(4):895–899, 2011. ISSN 1738-494X. doi: 10.1007/s12206-011-0214-5.

- [18] D. Lee. Shear rate dependence of thermal conductivity and its effect on heat transfer in a non-newtonian flow system. *Korean Journal of chemical engineering*, 15(3):252–261, 1998.
- [19] P. Livesey, A. Donneuy, and C. Tomlinson. Measurement of the Heat of Hydration of Cement. *Cement & Concrete Composites*, 13:177–185, 1991.
- [20] P.R.M. Lyra and R Lima. An axisymmetric finite volume formulation for the solution of heat conduction problems using unstructured meshes. *Journal of the Brazilian . . .*, XXVII(4):407–414, 2005.
- [21] J J Mason, A J Rosakis, and G Ravichandran. On the strain and strain rate dependence of the fraction of plastic work converted to heat: an experimental study using high speed infrared detectors and the Kolsky bar. *Journal of Mechanics of Materials*, 17:135–145, 1994.
- [22] D. Mikuli, B. Milovanovi, and I. Gabrijel. Analysis of Thermal Properties of Cement Paste During Setting and Hardening. pages 465–471, 2013. doi: 10.1007/978-94-007-0723-8.
- [23] OGJ. Shell drills world's first MonoDiameter well in South Texas, 2002. URL <http://www.ogj.com/articles/print/volume-100/issue-43/drilling-production/shell-drills-worlds-first-monodiameter-well-in-south-texas.html>.
- [24] J.L. Perez-Castellanos and A. Rusinek. Temperature increase associated with plastic deformation under dynamic compression: Application to Aluminium alloy AL 6082. *Journal of theoretical and applied mechanics*, 50(2):377–398, 2012.
- [25] F. T. Pinho and P. M. Coelho. NON-NEWTONIAN HEAT TRANSFER, 2009. URL <http://www.eolss.net>.
- [26] D.R. Poirier and G.H. Geiger. *Transport Phenomena in Materials Processing*. Springer, 1994. ISBN 9783319485652. doi: 10.1007/978-3-319-48090-9.
- [27] A. Rusinek and J. R. Klepaczko. Experiments on heat generated during plastic deformation and stored energy for TRIP steels. *Materials and Design*, 30(1):35–48, 2009. ISSN 02641275. doi: 10.1016/j.matdes.2008.04.048.
- [28] Shell. Monodiameter drilling. URL <http://www.shell.com/careers/experienced-professionals/technical-careers/wells-engineering/monodiameter-drilling.html>.
- [29] R. Stribeck. *Die wesentlichen Eigenschaften der Gleit- und Rollenlager*. Springer, 1903.
- [30] G.I. Taylor and H Quinney. The latent energy remaining in a metal after cold working. *The proceedings of the Royal Society A: Mathematical, Physical & Engineering sciences*, 143(849), 1934.
- [31] Uddeholm. Specification: AISI4340 High tensile steel, . URL <http://www.uddeholm.com>.
- [32] Uddeholm. Specification: sverker @ 21, . URL <http://www.uddeholm.com>.
- [33] C. Vuik, E.J. Vermolen, M.B. van Gijzen, and M.J. Vuik. *Numerical Methods for Ordinary Differential Equations*. VSSD, Delft, second edition, 2015. ISBN 9 7890-7130-1742.
- [34] J. Wall. *Transient Heat Conduction : Analytical Methods*, volume 2. 2009. URL <http://www.ewp.rpi.edu/hartford/{~}wallj2/CHT/>.
- [35] D.G. Wilmlink. *Experimental and theoretical modelling of ironing during tubular expansion*. Msc. thesis, University of Twente, 2016.
- [36] A.A. Yevtushenko, E.G. Ivanykt, and O.M. Ukhanska. transnsient temperature of local moving areas of sliding contact T- (S & 3. *Tribology International*, 30(3):209–214, 1997.
- [37] R. Zaera, J. A. Rodríguez-Martínez, and D. Rittel. On the Taylor-Quinney coefficient in dynamically phase transforming materials. Application to 304 stainless steel. *International Journal of Plasticity*, 40:185–201, 2013. ISSN 07496419. doi: 10.1016/j.ijplas.2012.08.003.
- [38] A. T. Zehnder. A Model for the heating due to plastic work. *Mechanics research communications*, 18(1): 23–28, 1991.